ABSTRACT

NEGI, ANKIT. Understanding and Engineering Thermal Transport in Perovskites (Under the direction of Dr. Jun Liu).

Perovskites are fascinating ABX_3 type structure that can accommodate a variety of A and B cations as well as X anions. Such versatility allows for tremendous multifunctionality as ferroelectrics, thermoelectric, photovoltaics and optoelectronic materials. The research on perovskite started as early as 1839, after the discovery of first perovskite. However, the research towards this material propelled only after the discovery of $BaTiO_3$ ceramics in the mid-1940s. The discovery of relaxor perovskites like PMN and the first hybrid organic inorganic perovskite were revolutionary milestones in the history of perovskites. The key to the remarkable properties of these materials lies in their structure. This study aims to study the thermal property-structure relationship in 3 major perovskites, namely, the classic $BaTiO_3$ (BTO), the up-and-coming revolution, PMN-PT and the hybrid perovskites.

PMN-PT consists of ferroelectric domain walls, which can be manipulated to realize dynamic modulation of thermal conductivity (k), which is essential for developing novel phononic circuits. Despite the interest, little attention has been paid to achieve room temperature thermal modulation in bulk materials due to challenges in obtaining high thermal conductivity switch ratio (k_{high}/k_{low}), particularly in commercially viable materials. I demonstrated room temperature thermal modulation in 2.5 mm-thick $Pb(Mg_{1/3}Nb_{2/3})O_3$-$x$$PbTiO_3$ (PMN-xPT) single crystals. With the use of advanced poling conditions, assisted by the systematic study on composition and orientation dependence of PMN-xPT, I observed a range of thermal conductivity switch ratio with a maximum ≈1.25. This work highlights the potential of commercially available PMN-xPT single crystals among other relaxor-ferroelectrics for achieving temperature control in solid-state devices.

BTO like Nanosized perovskite ferroelectrics are widely employed in several electromechanical, photonics, and thermoelectric applications. Scaling of ferroelectric materials entails a severe reduction in the lattice (phonon) thermal conductivity, particularly at sub-100 nm length scales. Such thermal conductivity reduction can be accurately predicted using the information of phonon mean free path (MFP) distribution. The current understanding of phonon MFP distribution in perovskite ferroelectrics is still inconclusive despite the critical thermal management implications. Using experimental thermal conductivity measurements and first-principles based modeling (including four-phonon scattering), I determined the phonon MFP distribution in BTO. The simulation results agree with the measured thickness-dependent thermal conductivity. My experimentally validated phonon MFP distribution is consistent with the theoretical predictions of other complex crystals with strong anharmonicity. This work paves the way for thermal management in nanostructured and ferroelectric-domain-engineered systems for oxide perovskite-based functional materials.

2D Hybrid organic inorganic perovskites (HOIP) are potential candidates for several industrial applications. Implementation of these materials at a device level demands a comprehensive understanding of their thermal conductivity to mitigate thermal management challenges and ensure long term device stability. Here, 12 different 2D HOIP thin films were prepared by changing the organic cations comprising pure achiral, mixed achiral, mixed chiral and pure chiral. The thermal conductivity of the pure achiral 2D HOIP is mostly contingent on the length of organic layer and the thermal conductance between the organic layers. In mixed achiral 2D HOIP, the thermal conductivity is largely determined by the length of organic layer and the CH--π interaction between organic cations. Using a combination of pure and mixed achiral 2D HOIPs, an unprecedented interlayer dependence of thermal conductivity is clearly observed. The thermal conductivity of all the mixed chiral 2D HOIP is same regardless of the achiral organic cation suggesting the dominance of organic-organic thermal conductance in determining thermal transport. The thermal conductivity of pure chiral 2D HOIP is higher than the mixed chiral highlighting their candidacy in photovoltaic devices. This work shows the relevance of these materials as ultralow thermal conductivity materials.

Understanding and Engineering Thermal Transport in Perovskites

by
Ankit Negi

A dissertation submitted to the Graduate Faculty of
North Carolina State University
in partial fulfillment of the
requirements for the degree of
Doctor of Philosophy

Mechanical Engineering

Raleigh, North Carolina
2023

APPROVED BY:

Dr. Jun Liu Committee Chair	Dr. Xiaoning Jiang
Dr. Yong Zhu	Dr. Divine Kumah

DEDICATION

Dedicated to my family, who laughed and cried together

whenever and wherever during my long journey.

BIOGRAPHY

Ankit Negi is currently a Ph.D. candidate in the Department of Mechanical and Aerospace Engineering at North Carolina State University and has been working at the Nanoscale Thermal Transport Laboratory since 2018. He pursued a B.Tech. in Mechanical Engineering from Nirma University (Ahmedabad, India) and worked on modeling fluid flow and conjugate heat transfer problems. interested in modeling and simulating nanoscale heat transport phenomena. Prior to pursuing his Ph.D. career, he worked as a junior research fellow at IIT Gandhinagar (India) on diesel and methanol powered full cell reformer systems. During his Ph.D., he focused on characterizing thermal transport in bulk systems and thin films using optical and electrothermal methods. He has extensive experience in thermal characterization, sample preparation, material characterization, developing heat transfer models in commercial packages and data post processing. His expertise lies in thermal characterization of ferroelectric single crystals and thin films, and hybrid perovskite thin films. He intends to join the semiconductor industry as a mechanical engineer to utilize his skills in developing deposition chambers and processes. Outside of work, he enjoys an active lifestyle, travel and going to hike with friends.

ACKNOWLEDGMENTS

First and foremost, I'd like to express my biggest thanks to my advisor, Dr. Jun Liu for his constant motivation, support, insights, and discussions . I learned a lot of things from Dr. Liu, apart from my technical skills, like prioritizing multiple projects, collaborating with other groups, positively pushing everyone to move the projects forward, time management and a positive attitude. There have been plenty of times during my PhD when things don't seem to work out and discussing with Dr. Liu seems to almost magically show a ray of hope. My PhD would not have been possible without his words of enthusiasm and the weekly meetings.

I'd also like to thank my committee members Dr. Xiaoning Jiang, Dr. Yong Zhu and Dr. Divine Kumah for their constant help with ferroelectric projects. The monthly update meetings helped me to work harder and keep everything on track. Thanks to Dr. Peters and her student Anastasia for an amazing collaboration. Thanks to their lab members Dr. Haotian Wan, Dr. Hwang Pill Kim, Dr. Shuang Wu, and Xuanyi Zhang for helping in a lot of discussions and setting up experiments. A super big thanks to Dr. Dali Sun , who was always there when I needed his help. He was always easy to approach and pleasant to talk to. He always has some revolutionary ideas to try out that have helped me a lot during my PhD. I'm also thankful to his group members, Dr. Eric Vetter, and Andrew for helping me with depositions. None of my measurements were possible without their metal depositions.

I'd also like to thank my group members for fostering a friendly and cordial environment. I have fond memories of Dr. Kyunghoon Kim and Dr. Jixiong He, both of whom are now happily making tons of money in their jobs. I also had a great time with Saqlain, Ziqi, Cong and Carter.

I'm highly appreciative of my family, friends, and Pone for providing support during the difficult times and believing in me.

TABLE OF CONTENTS

LIST OF TABLES

LIST OF FIGURES

CHAPTER 1

INTRODUCTION

1.1 Engineering Thermal conductivity of materials

Thermal conductivity (k) is an inherent material property that characterizes heat flow in a material. [1] A high thermal conductivity material, such as metals, Si, GaN, graphene, SiC, diamond (k ~ 2000 W m^{-1} K^{-1}) etc. offer less resistance to heat flow and are suitable for several heat dissipation applications.[2–5] Similarly, low thermally conducting materials, such as air (k ~ 0.026 W m^{-1} K^{-1}), foam, glass, etc. are excellent candidates for thermal insulation and heat localization applications.[6–8] In solids, heat is predominantly carried by electrons and lattice vibrations, aka phonons. [1] Majority of industrially viable materials are non-conducting, implying the contribution of electronic part is negligible. [1] Thus, understanding the "phononic picture" is key in manipulating thermal conductivity of several materials.

Engineering thermal conductivity of materials is increasingly adopted in various domains including energy conversion and storage, turbine blades, thermoelectrics, organic electronics and optoelectronics, corrosion resistant polymer heat exchangers, optics and more.[9–13] Nearly the entire thermal management efforts so far rely on presence of external medium (for instance, cooling fluids) to dissipate the heat produced in the devices.[14–17] However, the complexity in designing such cooling channels in emerging solid-state devices exacerbates the challenge in managing heat. Engineering thermal conductivity of materials is another route to tackle thermal management.[18–21] Further, achieving active control over heat manipulation offers functionality in novel thermal circuit devices (aka phononic circuit), highly regarded for solid-state thermoelectric and photovoltaic applications. This thesis focuses on engineering thermal conductivity of different materials which is applicable in several fields.[22,23]

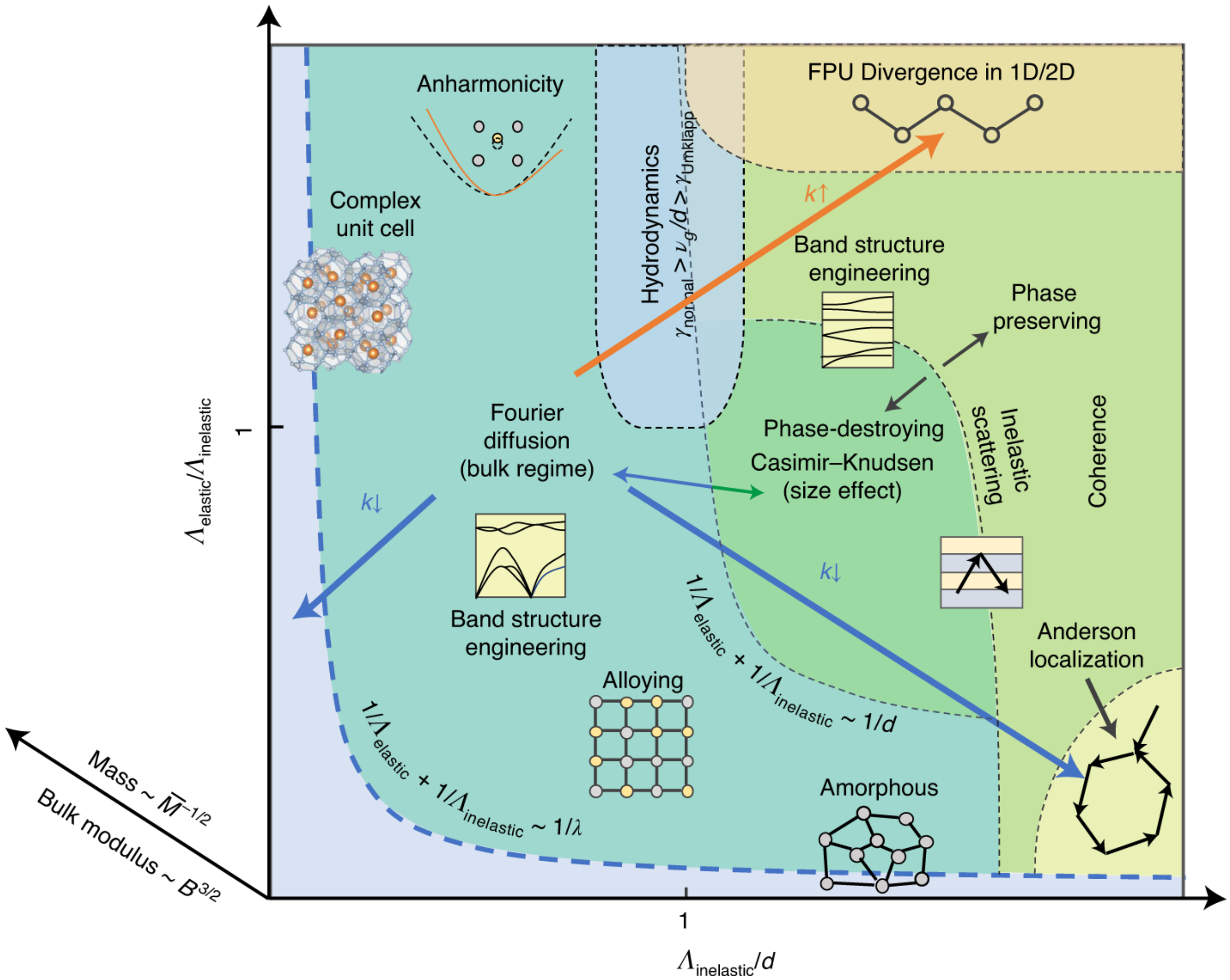

Figure 1.1 Different ways to engineer thermal conductivity (adapted from reference [1])

1.2 Engineering thermal conductivity in ferroelectric materials

In recent years, domain wall (DW) engineering in ferroelectric materials has been at the forefront of leading advancements in nanoelectronics, optics, and photovoltaics, often considered as a promising approach to achieve modulation of electrical, magnetic, optical, and thermal properties.[24–26] DWs are interfaces separating regions of different polarization orientations in ferroelectric materials. The structural or polarization discontinuity at DWs results in anomalous behavior in the material compared to the monodomain state. In relaxor-ferroelectrics such as $Pb(Mg_{1/3}Nb_{2/3})O_3$-$PbTiO_3$ (PMN-PT) or $Pb(In_{1/2}Nb_{1/2})O_3$–$Pb(Mg_{1/3}Nb_{2/3})O_3$–$PbTiO_3$ (PIN-PMN-

PT), manipulating DWs has been shown to achieve exceptional dielectric and piezoelectric properties, lending them as excellent candidates for several electromechanical applications including sensors, actuators, energy storage, drug delivery, diagnostic imaging, and non-destructive testing.[27–32]

Among several DW engineering methods to achieve further enhancement, use of alternating current poling (ACP) to manipulate domains has received considerable attention due to its convenience and effectiveness.[33–39] Studies have shown that up to 40% enhancement in piezoelectric coefficient (d_{33}) and 35% enhancement in free dielectric constants using ACP compared to conventional direct current poling (DCP) methods.[33–39] However, even though the DW engineering-based piezoelectric property enhancement is consistent for ACP, a consensus on how the domain size (or DW density) influences the piezoelectric properties is still not reached. Conventional belief in ferroelectrics has been that the property enhancement is due to high domain wall density [40–42]. Studies by Chang et al. [34], Xu et al.[39], Zhang et al. [36], and Sun et al. [33] on PMN-PT single crystals (SCs) show that the presence of monoclinic phases and finer domain sizes as a result of ACP are responsible for piezoelectric property enhancement, indicating that the conventional wisdom still holds for relaxor-ferroelectrics. However, other studies have shown conflicting results, suggesting an inverse relationship between domain size and piezoelectric properties.[43] Qiu et al. showed that the enhancement in [001] AC-poled PMN-PT is due to the reduction of 71° DWs.[44] Similar results were also obtained in other studies [45], including other relaxor-ferroelectrics such as PIN-PMN-PT. [46]

Part of the reason for the conflicting results observed in the literature lies in the limitations of DW density characterization methods. Typical experimental methods used to characterize domains can be classified into electromechanical (piezoresponse force microscopy (PFM)[34]), optical (polarized light microscopy (PLM)[44], and diffraction-based (X-ray diffraction (XRD))[47]) methods. PFM only scans the surface features (depth < 10 nm) and typically over a small region (~ 10-50 μm). This localized measurement makes it highly susceptible to skin effect and artifacts in relaxor-ferroelectrics [48], meaning that the PFM might not reflect the bulk domain structure in crystals. Although PLM does scan the bulk of the crystal, it is only suitable for observing DW density along a certain direction, otherwise, the overlap of domain walls makes it difficult to interpret the PLM data. [49]XRD works well to assess the bulk domain structure but is limited by selection of refinements, particularly for inhomogeneous domain sizes, which leads to inconsistency in analyzing the XRD data. [50–52] Thus, although localized DW density can be obtained using such characterizations, measurement of bulk domain structures (typically for thicker samples) can involve some uncertainty due to inhomogeneity in the DW distribution. In addition, use of simulation methods such as phase field [44] and first-principles [53] can help identify the mesoscale or atomistic scale origin of piezoelectricity, but does not account for potential inhomogeneity in bulk scale. This challenge highlights the need for a bulk characterization method to assess the overall domain structure in relaxor-ferroelectrics and to understand the influence of DW density on electromechanical property enhancement.

Interestingly, DW engineering has also been applied in the field of thermal science, to modulate thermal conductivity (k) for achieving better control on solid-state heat transfer. [54–62] Thermal conductivity decreases by introducing DWs that act as thermal resistances inhibiting thermal transport. [54–62] The ease in manipulating ferroelectric DW density by electrical input has opened novel possibilities in thermal transport engineering, which led to developments in ferroelectric thermal switches to enable dynamic control over heat flux in a material. Thermal switches modulate thermal conductivity between two states (k_{high} and k_{low}), where the high thermal conductivity state (k_{high}) is a result of lower ferroelectric DW density and vice versa. Several ferroelectric DW-based thermal switches have been reported, attempting to achieve maximum contrast in DW density to obtain high thermal conductivity switch ratio (k_{high}/ k_{low}). [54–62] Thus, utilizing this well-established relation between thermal conductivity and DW density, thermal conductivity characterization can serve as an alternative approach to assess the bulk DW density in relaxor-ferroelectrics.

However, most thermal switches proposed so far focuses on thin films, [57–62] and less attention has been paid to achieving thermal conductivity modulation in bulk crystals [54–56] despite their practical feasibility. Further, the length scale and orientation of domains in thin films are primarily restricted by the film thickness aside from other factors such as strain, residual stress, and boundary conditions. Thus, achieving a high thermal conductivity modulation (by enhancing contrast in DW density) is challenging. The only solution is to somehow reduce the domain size to sizes comparable to the length scale of heat carriers (phonon mean free path), taking advantage of boundary scattering. But achieving domain size reduction to such scales (usually < 100 nm) requires specific film preparation and high electric field, which has limited the maximum thermal conductivity contrast[57–62]. It poses the question of whether bulk scale thermal modulation can offer a higher thermal contrast, considering the domain size restrictions on bulk samples are less severe. Additionally, while several studies have used a constant voltage bias (i.e., DCP) to manipulate ferroelectric domain walls, there has been little exploration of other electrical poling methods, such as ACP, which may improve the thermal conductivity contrast.

In this regard, we demonstrate thermal conductivity modulation in lead-based relaxor-ferroelectric [001]-oriented (100-*x*) $Pb(Mg_{1/3}Nb_{2/3})O_3$-*x*$PbTiO_3$ (PMN-*x*PT), (27<*x*<33) single crystals. The primary reason to choose PMN-PT single crystals is their substantial enhancement in piezoelectric coefficient (d_{33} > 2000 pC/N) using DW engineering near morphotropic phase boundary (MPB: $27<x<32$) compared to other ferroelectrics. In addition, DW engineering of PMN-PT SCs using ACP has been readily conducted and well documented in the literature. [33–39] The purpose of this work is two-fold: (1) Firstly, to demonstrate thermal conductivity modulation (or DW density contrast) with DW engineering of PMN-PT SCs using DCP and ACP, which is supported by the DW density measurements using PLM and quantitative PLM (QPLM) based birefringence measurement; (2) Secondly, to measure the piezoelectric coefficient (d_{33}) for the same set of samples to understand the effect of DW density on the d_{33} enhancement.

1.3 Thermal conductivity scaling in oxide perovskite thin films

Thermal conductivity (k) is an inherent property that dictates the heat flow in a material. In dielectric solids, thermal conductivity is predominantly due to phonons, normal modes of atomic vibrations.[63]The phonon dispersion relation (frequency and wavevector) and the phonon scattering, which characterize the propagation of phonons and the interactions among phonons, respectively, describe the behavior of phonons in a material. The spectral nature of phonons is expressed using the concept of phonon mean free path (MFP) distribution, where the contribution to thermal conductivity from phonons with different phonon MFPs can be clearly seen.[64] With this information, we can tailor the thermal conductivity of materials using nano-engineering approaches or predict the reduced thermal conductivity in nanostructure, because the contribution from phonons with MFP larger than the characteristic length of nanostructure is strongly suppressed.[65–68] The challenge, however, lies in evaluating the phonon MFP distribution using experimental or modelling approaches.[69] Oxide perovskite (ABO_3) based ferroelectrics are typical materials for such study owing to the ubiquity of these materials as nanostructures and thin films.

Further, the insights for these oxide perovskites serve as a standard to generalize the phonon MFP distribution of other complex crystalline materials with strong anharmonicity.

Oxide perovskite thin films, such as barium titanate ($BaTiO_3$ or BTO), have been considered ideal candidates for several industrial applications.[70–72] For instance, the strong ferroelectric behavior, i.e., high room temperature polarization, observed in such epitaxially grown films shows their potential as lead-free field-effect transistors and in other ferroelectric/piezoelectric devices.[73,74] Adding to the impressive piezoelectric properties, their high dielectric constants and low dissipation further make them a suitable material for energy storage and conversion devices.[75–77] More recently, such thin films and nanostructures have also been rendered functional in photonics due to their tunable optoelectronics properties coupled with physical hardness, stability, and variety of growth methods for large-scale production.[78] Studies have also explored other potential applications for these thin films including anti-reflecting coating for resistive switching memories [79], superconductors [80], solar [81], photoelectrochemical water splitting [82], actuators for microelectromechanical systems [83] and in thermoelectric energy conversion [84].

While the electrical, optical, and mechanical properties of BTO have been highlighted in studies, little attention has been paid to thermal properties despite the concern regarding thermal management in such devices.[85]As an example, thermal dissipation is critical for ensuring reliability in high-energy-density photonic network-on-chip devices. [86] Variation in temperature alters the electro-optical properties of the underlying material, thus making thermal management vital in such cases. To ensure steady-state operation of these high energy devices and mitigate thermal runaway, thermal conductivity of the material should be considered during device design. Of particular interest is the thermal conductivity of sub-100 nm thin films or nanostructures, which is the typical feature size in several systems. The MFP of heat carriers (phonons) becomes comparable at the sub-100 nm sizes, which can lead to significant reduction in thermal conductivity due to boundary scattering. Thus, knowledge of phonon MFP distribution is important for appropriate thermal management for such systems.

One way to construct the phonon MFP distribution is to measure thermal conductivity at several characteristic lengths. The characteristic length can be the film thickness for single crystalline films [87], feature size of nanostructures [88], and grain size for polycrystalline thin films [89]. Experimentally, particularly for oxide perovskites, majority of the thin films reported in literature are polycrystalline, because the growth of high-quality perovskite thin films is highly susceptible to substrate, buffer layers, miscut, and chemical termination.[90] The scantness in experimental data makes it challenging to extract the phonon MFP distribution. For BTO, experimental thermal conductivity measurements are not only limited but also show inconsistent values. For bulk crystals, thermal conductivity values of 5.7 W m^{-1} K^{-1}[54] and 3.6 W m^{-1} K^{-1} [91] have been obtained for single crystals while 2.7 W m^{-1} K^{-1} [92] and 10.2 W m^{-1} K^{-1} [93] have been reported for ceramics. For thin films, earlier measurements using the 3ω method show near bulk thermal conductivity for 100 nm polycrystalline BTO film with 150 nm average grain size (4.8 W m^{-1} K^{-1} for 100 nm film thickness compared to 5.15 W m^{-1} K^{-1} for 1 μm film thickness).[94] It indicates that the average phonon MFP in BTO is much lower than 150 nm. However, recent measurements using the time-domain thermoreflectance (TDTR) method for nanograined BTO films suggest a much higher average phonon MFP, showing more than 50% thermal conductivity reduction for an epitaxial 175 nm film thickness compared to bulk.[95] Subsequent measurements using TDTR also show a similar high average phonon MFP.[96,97] Therefore, this information about the phonon MFP distribution in BTO is not conclusive in the literature due to the lack of consistency in the quality of grown films and discrepancy in the measured data. Moreover, simulations remain challenging due to either the inaccuracy of the force field in molecular dynamics or excluding the effects of higher-order anharmonicity in the first-principles based modeling.

Addressing such discrepancies in the phonon MFP distribution is vital, not only for BTO, but also for the study of other oxide perovskites. For instance, in a recent study [98], the thermal conductivity of $La_{0.5}Sr_{0.5}CoO_x$ is assumed to be constant in a thickness range of 8-16 nm. This is justified by the near linear MFP distribution in the thickness range calculated using harmonic dispersion and empirical scattering rates. Such approximations severely overestimate the average MFP, which challenges the feasibility of underlying assumption in the study. This highlights the need for the accurate prediction and measurement of phonon MFP distribution. Another example is found in strontium titanate ($SrTiO_3$ or STO). Foley et al. measured the thermal conductivity of several polycrystalline STO thin films with grain sizes ranging from ≈ 30 nm – 90 nm. They observed that the thermal conductivity contribution of the ~ 100 nm grain size is around 50-60%.[89] Similar results were also obtained for undoped and La: doped STO ceramics.[99,100] Theoretically, Feng et al. used a combined first-principles molecular dynamics and anharmonic lattice dynamics approach to construct the phonon MFP distribution for STO.[101] Despite accounting for only three-phonon scatterings, their results indicate that a major portion of heat (~80%) is carried by phonons with MFP less than 100 nm, contrary to the experimental results.

To address these discrepancies, we experimentally measured the through-thickness thermal conductivity of high-quality single-crystalline [001]-oriented BTO films in a thickness range of 14-56 nm and a bulk single crystal of 0.5 mm thick, at room temperature. We also calculated the phonon MFP distribution of BTO using *ab initio* molecular dynamics simulation and Boltzmann transport equation with the consideration of phonon scattering processes up to the fourth order. The calculated phonon MFP agrees well with our measured thickness-dependent thermal conductivity data. We observed a dramatic rise in thermal conductivity around phonon MFP≈10 nm, achieving near bulk thermal conductivity value for MFP≈100 nm. Strong anharmonicity in the crystal structure of BTO makes four-phonon scattering important for reducing the average phonon MFP. The predicted MFP distribution is also in agreement with other strongly anharmonic complex crystal systems.

.

1.4 Engineering thermal transport in achiral and chiral hybrid perovskites

The perovskite structure (ABX_3), where A is typically a large cation, B is usually a medium-sized cation and X is an anion, exhibits unique electrical, optical, mechanical, and thermal properties.[102,103] The B and X sites form a corner-sharing BX_6 octahedron, "trapping" the A-site cation inside the 3D framework. The ability of the structure to accommodate several types of atoms/molecules renders the perovskite structure highly versatile and paves way towards emergence of hybrid organic and inorganic perovskites (HOIP).[104,105] The chemical and structural diversity of the organic and inorganic members in HOIPs offers wide range for tuning their physical properties and tailoring them for specific applications.[105] Methylammonium-based 3D HOIPs ($MAPbX_3$, X = Cl, Br or I) have been regarded as superior materials for photovoltaic devices, showing more than 15% conversion efficiency due to their tunable bandgap, high mobility of charge carriers and long carrier diffusion lengths.[106] In addition, these have also been considered ideal substitutions in light emitting devices because of their superior material quality and photoluminescence quantum efficiency.[107,108] Further, the presence of hydrogen bonding in HOIP, unlike in inorganic perovskites, also allows for tuning of electrical conductivity.[109] The disordered nature of organic cation inside the 3D inorganic framework results in unusually low thermal conductivity values, a thermal transport property which is critical in determining system level performance in thermoelectric and photovoltaic applications.[110]

Studies have explored several combinations of HOIP structures to achieve unique physical properties. For instance, substituting the A-site organic cation in 3D HOIPs with relatively large sized organic cation (ex, long chained alkylamines or arylamines) results in formation of their low dimensional 2D counterparts.[111–114] The structure of 2D HOIPs resembles a layered stack, with a general formula $R_2A_{n-1}B_nX_{3n+1}$, where one (n = 1) or multiple (n > 1, commonly called quasi-2D HOIP) B-X inorganic octahedron layers are separated by the weakly bonded organic spacers (R).[111,115] This restructuring improves the oxygen resistance and moisture stability of the HOIPs, mainly due to the increased hydrophobicity in large sized organic cations, enhanced structural orientation and packing density.[114–116] The constraint on the size of organic cation is further relaxed in 2D HOIP, allowing them access to a plethora of diverse structures to tailor their functionalities.[117] For instance, the electronic bandgap in alkylaryl ammonium ($(PEA)_2MA_{n-1}Pb_nI_{3n+1}$) 2D HOIPs can be tuned by around 20% by changing the thickness (n) of inorganic layer.[118] Further, differences in perovskite layer distortion in various acene alkylamines show significantly different optical characteristics.[119] Similar unique structure-property relations are also observed for other physical properties in several 2D HOIPs.[120]

Varying the interaction between organic cations (for instance, the intermolecular interaction between two R cations) offers yet another, and relatively less explored, degree of freedom to alter the 2D HOIP structure.[121] This can be simply done by replacing the existing R cations with a different organic cation. For instance, replacing 50% of PEA cations with BA in $[PEA]_2$ results in mixed [PEA][BA]. These so-called mixed 2D HOIPs exhibit unique interaction, unlike between pure alkyl or pure aryl ones, which can be utilized in modulating several properties.[121–124] Yet another way of tuning the HOIP structure can be achieved by introducing chirality in the structure.[125,126] This is facilitated by replacing the achiral organic ligand with chiral organic ligand. The distortions induced by the chiral molecules cause a reduction in crystal symmetry, which makes them highly appealing for applications including optoelectronics, bioencoding, and tomography.[125]

The simplicity in preparing 2D HOIPs using facile low temperature solution processing methods, typically spin casting, is driving the adoption of these materials at the device level.[127] Determining the best approach for implementing 2D HOIPs in devices requires a comprehensive understanding of several physical properties. For instance, 2D HOIPs with thicker inorganic layers ($n > 1$) show remarkable photovoltaic conversion efficiency[128,129] and improved mechanical strength[130]. Nevertheless, the materials' thermal conductivity decreases substantially, posing severe thermal management challenges and compromising device's long-term stability.[131,132] Understanding thermal properties is crucial for predicting the temperature levels in the system, which demands thermal conductivity characterization of the material. Compared to the relatively well-explored optical, electrical, and structural properties, studies on thermal transport and mechanical properties in HOIPs have only recently begun to emerge over the last decade.[104,105,107,110,133]

Most studies exploring thermal transport are focused on 3D HOIPs and only a handful of studies in 2D HOIPs, even though the thermal transport between the two is strikingly different.[133–135] Thermal conductivity in 2D HOIP is primarily dominated by phonons (lattice vibrations), which can be scattered at the inorganic layer, organic layer, inorganic-organic interface, and organic-organic interface.[110,133] Thermal conductivity in the cross-plane direction decreases with increasing inorganic layer thickness (n) for low n (n<5).[131] The challenge in ensuring stability of 2D HOIPs with increasing n however makes this approach less suitable for practical purposes. The length of organic layer does not have significant impact on thermal conductivity.[136] These studies imply that the best route to modulate thermal conductivity in 2D HOIPs involves playing with inorganic-organic and organic-organic interfaces. Indeed, decreasing the distance of the adjacent organic cations does increase thermal conductivity dramatically, but the specific interactions leading to the enhancement is still inconclusive.[137] Further, to achieve the reduction in spacing between organic cations is challenging from an experimental perspective. Nearly all the studies on thermal transport of 2D and even 3D HOIPs deal with pure achiral organic cations, which allows for little room to tune the interaction between organic-organic interfaces. [110,133] This highlights the need for a facile approach to modulate thermal transport in 2D HOIPs.

Herein, we prepared 12 different 2D HOIP thin films with mixed achiral and chiral organic cations. The chiral 2D HOIP thin films are further classified into two groups, half-chiral (when 50% of the achiral organic cation is replaced with chiral organic cation) and full-chiral (when the entire achiral organic cation is replaced with chiral organic cation). We measure the thermal conductivity of the thin films using time domain thermal reflectance (TDTR) method. Using the structural data and insights from GIWAXS characterization, we explain the observed thermal conductivity results. Further, we measure the elastic modulus of the 2D HOIP thin films using nanoindentation. To our knowledge, this is the first report of thermal conductivity and elastic modulus characterizations on mixed achiral and chiral 2D HOIP thin films. We also perform vibrational density of states calculations to support our observations.

1.5 Molecularly engineered ultralow thermal conductivity in hybrid perovskites

The ability of materials to conduct heat, characterized by thermal conductivity (k), is key in addressing thermal management challenges.[1] Rising concerns of temperature hot spots with miniaturization in electronic applications, growing intent towards waste heat recovery using thermoelectric and demand for better insulating materials for extreme environmental conditions are some of such challenges, that have driven the search for material strategies to further push the range of practically achievable thermal conductivity values.[1,138,139] Of particular interest is pushing the lower thermal conductivity limit of a relatively easy-to-prepare fully dense thin film, which is beneficial both from a practical standpoint as well as from a scientific perspective, by further developing the current understanding leading to such ultralow k. [1,138,139]

Thermal conductivity of a material is primarily bifurcated into electronic (portion of heat carried by electrons) and phononic components (portion of heat carried by lattice vibrations). Naturally, suppressing both components is key to achieving ultralow k. The electronic component can be conveniently neglected in materials with low electron density of states such as dielectrics, allowing us to narrow our scope to materials in which heat is primarily carried by phonons. Phonons are normal modes of lattice vibrations, which implies that they have an associated dispersion and undergo scattering. The lattice thermal conductivity (k_{lattice}) is thus influenced by the group velocity (determined from dispersion curve) and the scattering rate (or scattering length). [1] The former is dictated by the inherent atomic arrangement and periodicity in the lattice which is fixed for a given material under a specific temperature and pressure. Further suppression in k_{lattice} can be achieved by anharmonicity in the crystal and introducing scattering mechanisms that localize the vibrations to inhibit heat transport. Several scattering mechanisms exist including phonon-phonon, defect, boundary, resonant and dynamic disorder. [1] The role of strong anharmonicity and scattering due to the complex crystal arrangement is considered as the major reason for observing such ultralow k in several materials. Strong suppression in materials such as clathrates, half-Heuslers and skutterudites has been observed due to presence of anharmonic rattler modes and weak coupling between the host lattice and heavier guest atoms.[140–144] These low frequency rattler modes strongly scatter the acoustic phonons leading to low thermal conductivity in such materials. Resonant scattering in thermoelectrics such as PbTe and SnSe is shown to be responsible for scattering of acoustic and low-lying optical phonons causing thermal conductivity to drop nearly 5 times.[145–147] Similarly, alloying and effect of mass disorder has also been advocated to scatter high frequency phonons although demonstrating mass disorder in practice is challenging.[148] Even though k_{lattice} is suppressed significantly, the observed value is still higher than ~ 0.1 $Wm^{-1}K^{-1}$ with such methods.

Exceptionally low thermal conductivities can be achieved in materials by bringing the “amorphous nature” of materials.[149–152] One way to achieve this in crystalline materials is by limiting the period of crystallinity to a few unit cells by introducing interfaces (in other words, high interface density).[153–160] Ultralow thermal conductivity of around 0.05 W/m/K is observed for layered WSe2 crystals potentially because of random stacking of thin sheet and phonon focusing effect in highly anisotropic materials.[156,160] Similar values are obtained for WS_2 (~ 0.04) and $MoSe_2$ (~ 0.05) thin films using symmetry breaking by random rotation disorder.[154,157] Extremely low values have been recorded for PCBM thin films due to decrease in sound speed and dampening of vibrational frequencies. More recently, use of hybrid organic inorganic perovskite (HOIP) thin films has also emerged as a potential material to achieve the ultralow-k goal. This is further driven by the facile preparation of 2D HOIP thin films, high mechanical stiffness and multifunctionality.

Herein, we demonstrate ultralow thermal conductivity in Azobenzene ethylammonium (AZO) based 2D HOIP thin films. We prepared nine different AZO thin films with different thickness and baking conditions. Measurement of thermal conductivity using TDTR and structural characterization using GIWAXS show the variation in thermal conductivity among the films. Characterization of mechanical stiffness show that the films are mechanically compliant compared to other ultralow thermal conductivity films. Molecular dynamics simulations reveal the role of dynamic disorder at the weakly bonded organic interface leads to such ultralow thermal conductivity.

1.6 Objective and organization of dissertation

This thesis highlights and develops methods to engineer thermal transport in ferroelectric single crystals, thin films and hybrid organic-inorganic thin films. The selection of these materials is driven by their ubiquity in industrial and recent research in several fields of engineering and physics. This study also highlights the potential use of these materials to mitigate thermal management challenges.

In chapter 2, thermal conductivity modulation has been demonstrated in PMN-PT single crystals, which are already commercialized and widely used in ultrasound and piezoelectric applications. This study presents an additional functionality as thermal modulation, which further broadens the applicability of the material in different fields. From a scientific perspective, this study also uncovered some of the fundamental questions on domain wall engineering of ferroelectrics which is key for understanding their structure-property relationship. I believe that the methodology developed in this study can also be extended to other materials such as PIN-PMN-PT, which are nowadays preferred owing to low curie temperature.

Chapter 3 presents the understanding of phonon mean free path distribution in BTO. Surprisingly, even after decades of research on thermal properties, the accurate MFP prediction is not present for a lot of oxide perovskite materials like BTO. Information of MFP distribution aids in nano structuring in thermoelectric materials and avoids incorrect assumptions about thermal conductivity scaling. Further, MFP distribution can also be used to explore extreme thermal transport regimes such as super-diffusive and quasi-ballistic phonon transport.

Chapter 4 introduces a unique class of materials known as Hybrid organic inorganic perovskite (HOIP). These materials have already surpassed the photovoltaic efficiency of currently commercialized solar cell materials. Further, they are excellent candidates for thermoelectric, optical and electronic applications. Implementation of these materials on a device level requires a thorough understanding of their thermal conductivity. This study identifies the parameters that affect the thermal conductivity in 2D HOIP thin films. We prepared and measured different films that led to different thermal conductivity modulation. The organic-organic interface plays a dominant role in determining thermal conductivity in these materials.

Chapter 5 deals with molecular engineering of a specific 2D HOIP thin film which shows ultralow thermal conductivity. Nine different films with different thickness and annealing conditions are prepared and measured. Record low thermal conductivity is confirmed using TDTR and molecular dynamics assisted lattice dynamic simulations. The weak bonding in the organic interface, benzene pi-pi stacking and dynamic disorder leads to such ultralow thermal conductivity. The high mechanical stiffness, ultralow thermal conductivity, potential for thermal conductivity modulation, facile preparation and multifunctionality makes this an ideal material for several applications.

The final chapter of this dissertation outlines potential research directions in thermal transport engineering in the perovskites to further the understanding of scientific community.

CHAPTER 2

Ferroelectric domain wall engineering in PMN-PT single crystals

In this chapter thermal conductivity modulation has been demonstrated in PMN-PT single crystals, which are already commercialized and widely used in ultrasound and piezoelectric applications. This study presents an additional functionality as thermal modulation, which further broadens the applicability of the material in different fields. From a scientific perspective, this study also uncovered some of the fundamental questions on domain wall engineering of ferroelectrics which is key for understanding their structure-property relationship.

2.1 Introduction

Acting like thermal resistances, ferroelectric domain walls can be manipulated to realize dynamic modulation of thermal conductivity (k), which is essential for developing novel phononic circuits. Despite the interest, little attention has been paid to achieve room temperature thermal modulation in bulk materials due to challenges in obtaining high thermal conductivity switch ratio (k_{high}/k_{low}), particularly in commercially viable materials. Here, we demonstrate room temperature thermal modulation in 2.5 mm-thick $Pb(Mg_{1/3}Nb_{2/3})O_3$-$x$$PbTiO_3$ (PMN-xPT) single crystals. With the use of advanced poling conditions, assisted by the systematic study on composition and orientation dependence of PMN-xPT, we observed a range of thermal conductivity switch ratio with a maximum ≈1.25. Simultaneous measurements of piezoelectric coefficient (d_{33}) to characterize the poling state, domain wall density using polarized light microscopy (PLM) and birefringence change using quantitative PLM reveal that compared to the unpoled state, the domain wall density at intermediate poling states ($0< d_{33}< d_{33,max}$) is lower due to the enlargement in domain size. At optimized poling conditions ($d_{33,max}$), the domain sizes show increased inhomogeneity that leads to enhancement in the domain wall density. This work highlights the potential of commercially available PMN-*x*PT single crystals among other relaxor-ferroelectrics for achieving temperature control in solid-state devices.

2.2 Thermal conductivity modulation of ACP PMN-(30~33)PT single crystals

Probing the bulk thermal properties of ferroelectric DWs in PMN-PT single crystals is challenging for several reasons. Firstly, the probing depth (thermal penetration depth) in two of the most accurate thermal characterization methods, namely time domain thermo-reflectance (TDTR) [161–163] and frequency domain thermo-reflectance (FDTR) [164] is only a few microns. Considering an average domain size of 1 μm in PMN-PT SCs, these methods can only capture a few domains near the surface that do not reflect the real domain structure inside the material. Another common approach to measure thermal conductivity, the 3ω method [165], does not apply in this case. The 3ω method requires the deposition of a metal thermometer on top of the sample. This requirement is typically accomplished through lithography, which necessitates baking samples at temperatures greater than 150 °C, higher than the depoling temperature (when the aligned domains begin to reorient) of PMN-PT SCs (130 ~ 170 °C).[166] Other methods, such as Laser Flash Analysis and HotDisk, have strict requirements on sample shape and size, requiring large sample sizes and thickness that have a limited frequency range for their transducer applications. [167] Thus, given the need to probe bulk thermal transport in PMN-PT SCs, this work uses a steady-state infrared radiation (IR) camera measurement to obtain the temperature difference across the single crystals (along the [001] direction). (a) shows the schematic of the steady-state IR camera method for temperature difference (the details are described in Section). The steady-state IR camera method was calibrated using standard BK-7 glass (k ~ 1.0 W m^{-1} K^{-1}) and fused quartz (k ~1.4 W m^{-1} K^{-1}) samples.

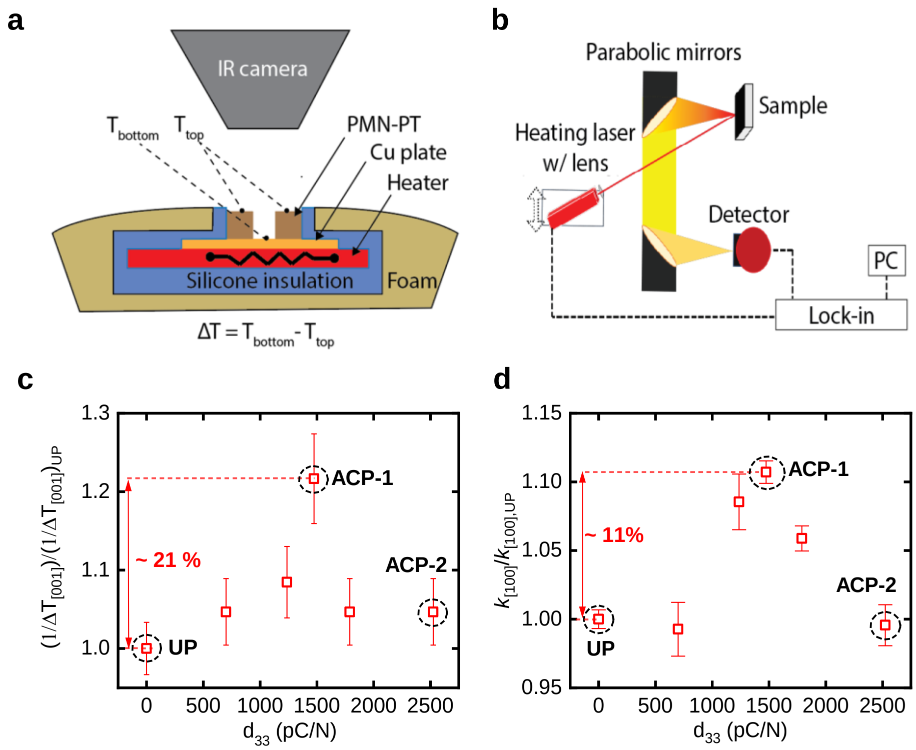

Figure 2.1 (a) Schematic of experimental setup for steady-state temperature difference characterization. The temperature difference ($\Delta T_{[001]}$) across the PMN-PT sample is measured using the IR camera under steady state. (b) Schematic of experimental setup for thermal conductivity measurement using PTR. (c) Normalized temperature difference [$(1/\Delta T)/(1/\Delta T)_{UP}$] along the [001] direction of the UP and ACP PMN-(30~33) PT single crystals poled along the [001] direction as measured from the steady state IR measurement. (d) The normalized thermal conductivity ($k_{[100]}/k_{[100],UP}$) of UP and ACP PMN-(30~33) PT SCs poled along the [001] direction. The sample size for both the measurements is 10 mm × 5mm × 2.5 mm. The data is presented in the form of mean ± standard deviation. Similar behavior of thermal contrast is observed in both results thereby verifying the steady-state measurements.

Firstly, we measured the thermal conductivity modulation in ACP ([001] poled) PMN-(30~33)PT SCs. All the crystals were initially depoled using the method delineated in Section 4.1, resulting in an unpoled (UP) state, which corresponds to a $d_{33} \sim 0$. We varied the poling conditions in ACP to obtain a range of poling states (marked by distinct d_{33} values). The poling conditions and measured d_{33} are shown in section 4.5. The reported thermal conductivity enhancement (or contrast) is measured with reference to the thermal conductivity of the UP state. We anticipated a monotonous thermal conductivity contrast with an increasing d_{33}, under the assumption that the DW density (or domain size) change is primarily responsible for the contrast in d_{33}. [40–43]

Figure 2.1(c) shows the normalized temperature difference $[(1/\Delta T)/(1/\Delta T_{UP})]$ along the [001] direction observed using the steady-state IR camera measurement. The absolute temperature difference is provided in SI Section S4 for reference. Under the steady state, the contrast in normalized temperature difference is the same as the normalized thermal conductivity contrast. Hereafter for simplicity, we stick to thermal conductivity in the discussion. Contrary to the assumption, the thermal conductivity does not show a monotonous behavior with an increase in d_{33}. The maximum thermal conductivity enhancement of ≈21% occurs at an intermediate poling state (ACP-1, d_{33}~1480 pC/N). Intermittent poling states, between UP and ACP-1, show an increase in thermal conductivity with d_{33}. Interestingly, the optimized poling state (ACP-2, $d_{33} \sim$ 2530 pC/N) shows a reduced thermal conductivity compared to ACP-1.

We also measured thermal conductivity of the same set of single crystals using the photothermal radiometry (PTR) method (the schematic of the PTR method is in Figure 2.1(b) and the description can be found in Section). Figure 2.1(d) presents the normalized thermal conductivity ($k_{[100]}/k_{[100]UP}$) along the [100] direction as a function of d_{33}. Thermal conductivity is comparable in both UP and the optimized ACP states, with a maximum value at the intermediate poling state (ACP-1, $d_{33} \sim$

1480 pC/N). This finding is consistent with the results obtained from the steady-state IR camera method. The maximum thermal conductivity enhancement measured using PTR is ≈11%, which is lower than the contrast measured using steady-state IR measurement (≈21%). This discrepancy can be attributed to the fact that PTR measures the in-plane thermal conductivity (along the [100] direction), while steady-state IR measurement is along the cross-plane direction ([001]). Furthermore, our anisotropic temperature difference measurements (shown in Figure 2.2 and described in Section) show that the maximum contrast occurs along the poling direction ([001]), due to different domain structures, which explains the lower thermal conductivity enhancement in PTR compared to the steady state IR measurement.

Using the inverse dependence of thermal conductivity on DW density, the observations indicate that the DW density decreases with AC poling until ACP-1 and then increases upon further poling. The reduction in DW density for intermediate poling states is consistent with the phase field simulation of Qiu et al. at intermediate E-field (equivalent to intermediate poling state in our case) under ACP that shows an enlargement of domains due to the elimination of 71° walls.[44] The intermediate poling states offer finer control over thermal conductivity and heat transfer, as opposed to binary k_{high} and k_{low} states in conventional thermal switches. At optimized poling, the domain enlargement behavior is not fully replicated, potentially because of increasing inhomogeneity in the material, where some regions grew smaller while others grew larger, resulting in an overall increase in DW density. The inhomogeneity in optimized ACP sample is further highlighted in Figure 2.3 and discussed in Section 2.3.

We note that in the current study, the thermal conductivity in PMN-PT single crystals is primarily due to phonons (i.e., lattice vibration) with a negligible electronic contribution. In some ferroelectrics, the formation of charged domain walls can result in metallic-like electrical conductivity,[168–170] which may lead to significant electronic contribution with increasing DW density. However, as described in SI Section S6, the poling conditions employed in this study make it unlikely to form such strongly charged domain walls. Furthermore, even if the enhanced electrical conductivity of charged domain walls is considered, the estimated electronic contribution is still negligible compared to the thermal conductivity contrast observed in the study. Moreover, to deconvolute the effect of potential structural changes incurred during ACP on thermal conductivity, we conducted XRD measurements on PMN-(30~33)PT single crystals. SI Section S7 shows the XRD results of UP, ACP-1, and ACP-2 samples. The peak positions for all the poling states are consistent within the XRD measurement uncertainty, indicating that the effect of any strain on thermal conductivity is similar in all the cases. This suggests that the observed thermal conductivity contrast in the current study is primarily due to the change in DW density with poling.

2.3 Thermal conductivity modulation of ACP PMN-(30~33)PT single crystals

To determine the direction that offers the maximum thermal conductivity contrast, we conducted the steady-state temperature difference measurement along all three directions {001, 010, and 100} for the UP, [001]-poled DCP, and [001]-poled ACP PMN-PT SCs. Figure 2.2 shows the normalized temperature difference $[(1/\Delta T)/\ (1/\Delta T)_{UP})]$ measured for PMN-(27-30)PT (low-PT) and PMN-(30-33)PT (high-PT) compositions.

Different thermal modulation behaviors are observed upon poling for the two compositions. The maximum thermal conductivity contrast is achieved at intermediate poling states for both compositions (~21% at d_{33}~1590 pC/N for high-PT and ~ 12% at d_{33}~1390 pC/N for low-PT). For low-PT SCs under ACP (Figure 2.2**(a)**), the DW density increases on poling, contrary to the high-PT compositions (Figure 2.2 **(b)**), where the DW density decreases in comparison to the UP state.

This dissimilarity in thermal conductivity can potentially be explained by the comparatively higher presence of polar nano-regions (PNRs) in low-PT SCs. PNRs serve as regions of phase instability in relaxor-ferroelectrics, which leads to softening of transverse acoustic phonon modes.[171] This explains the lower thermal conductivity of the UP low-PT SC in comparison to high-PT as measured by PTR ($k_{UP,low\text{-}PT} \approx 1.38$ W m^{-1} K^{-1} compared to $k_{UP,high\text{-}PT} \approx 1.43$ W m^{-1} K^{-1}). Thus, in low-PT, the thermal conductivity reduction caused by PNRs can outweigh the thermal conductivity increase caused by DW reduction. The inconsistent behavior in the three directions for the low-PT is indicative of asymmetry in lattice dynamics induced by anisotropic PNR structure.[171–173] However, further study is needed to understand this effect. As this study primarily concerns high thermal conductivity contrast, we stick to high-PT crystals for further discussion.

Figure 2.2 (b) shows the normalized temperature difference along the three directions for DCP and ACP high-PT SCs. The maximum thermal conductivity contrast (~21%) occurs in the poling direction ([001]). Additionally, the contrast observed in the [010] and [100] directions, which is equivalent in a rhombohedral [001] poled PMN-PT, is similar within the experimental uncertainty. The maximum contrast along these two directions is around 12%, which is consistent with the PTR measurements shown in Figure 1(d). The thermal conductivity of samples increases to a maximum upon poling and then decreases.

The trend is particularly evident in [001], where the maximum contrast is higher, but can also be observed along [010] and [100] directions in PMN-(30~33)PT single crystals. The differences in thermal conductivity enhancement between the [001] and [100] (or equivalent [010]) directions can be attributed to the orientation of DWs, as illustrated in Figure 2.2(c).

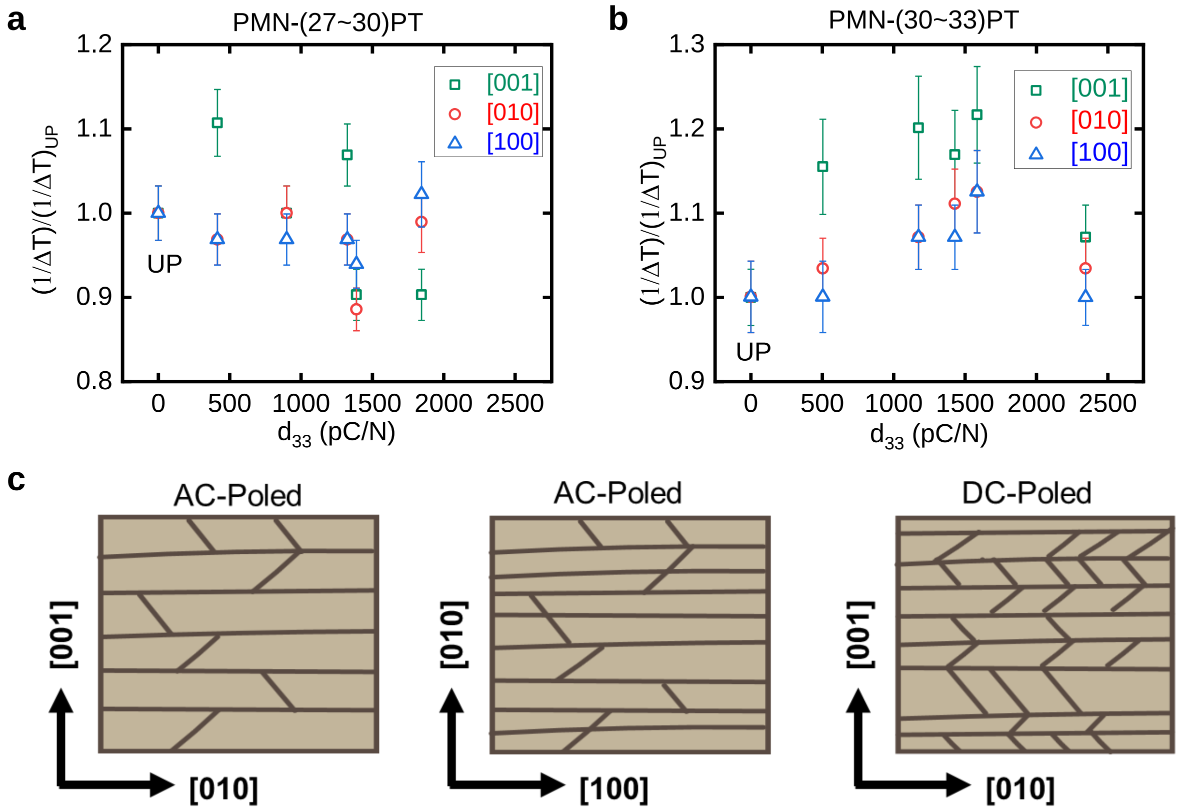

Figure 2.2 Anisotropic normalized temperature difference [(1/ΔT)/ (1/ΔT)$_{UP}$)] measured using IR camera for UP, DCP and ACP PMN-PT SCs. (a) PMN-(27~30)PT and (b) PMN-(30~33)PT crystals poled along the [001] direction. The size of single crystals is 2.5 mm × 2.5 mm × 2.5 mm. Each d$_{33}$ value is obtained by poling three samples under similar poling conditions to ensure repeatability. The poling conditions are shown in the Section Table 2 and. The data is presented in the form of mean ± standard deviation. (c) The schematic of DW orientation under ACP and DCP along the [001] direction. ACP results in laminar domains formed by 109° DWs when viewed along the (100) plane. The majority of 71° DWs are eliminated during ACP leading to a fewer DW density in ACP compared to DCP. The average domain size in the ACP is thus larger than in the DCP. When viewed along the (001) plane for the ACP sample, the overlapping 109° DWs makes the domain size smaller.

For instance, [001] AC poled sample exhibits laminar-like domains created by the 109° DWs, which are evaluated using PLM (Figure 2.3) and in other studies. [44,174] The same sample shows reduced overall domain size when observed along [100] or [010] directions caused by overlapping 71° and 109° DWs. As shown in 2.2 (c), the domain size is maximized along the [001] direction, resulting in the highest thermal conductivity contrast in comparison to other directions.

The maximum thermal conductivity enhancement in ACP samples (~21%) is higher compared to DCP samples (~18%), as also shown in SI Figure S8. The intermediate poling states (DCP-1 and ACP-1) display the highest enhancement for both poling conditions. The higher contrast in ACP highlights its effectiveness in eliminating the 71° DWs. Additionally, the thermal conductivity contrast between DCP-1 and DCP-2 is significantly lower than ACP samples, which implies that the enhanced inhomogeneity in ACP-2 is related to the switching of electric field direction.

2.4 Domain wall density measured by PLM

To investigate the effect of DW density on piezoelectric enhancement and to further reinforce the thermal conductivity measurement results, we did PLM measurements on PMN-(30~33)PT crystals. Figure 2.3 shows the PLM response of the UP and the ACP samples. Referring to Figure 2.1(c) , the intermediate poled state (d_{33}~1480 pC/N) is called ACP-1, and the optimized poled state (d_{33}~ 2530 pC/N) is ACP-2.

<u>Aligning the principal optical axis of single crystals with either that of polarizer or analyzer results in complete extinction</u> [175] Figure 2.3(a) shows extinction at P/A (angle between polarizer and analyzer) = 45° (along {110} directions), which indicates the dominant presence of rhombohedral phase (R-phase). [175] The UP single crystal is expected to be R-phase dominant considering the composition of crystal within the MPB at room temperature. Figure 2.3(b) shows that the majority of the regions in ACP-1 are R-phase with small indications of other phases, similar to other studies.

[33] [176] Figure 2.3(c) indicates that ACP-2 is also predominantly R-phase, which implies that the poling conditions do not lead to a significant phase change.

Figure 2.3(d) shows a typical domain orientation under ACP of PMN-PT singe crystals, consisting primarily of 109° DWs with a few 71° DWs. The former DWs are birefringent, meaning that light passing through the sample will be retarded depending on the differences in the refractive indices between the fast and slow axis. The retardation of white light results in an interference pattern, as shown in Figures 2.3(a-c) at P/A:0°, which is observed using PLM. Higher density of birefringent DWs will result in higher order interference colors. ACP-1 shows a uniform interference throughout the sample surface, indicating a homogenous domain wall distribution. In contrast, ACP-2 exhibits a mix of higher- and lower-order interference colors. This suggests that some domains grew larger while others shrank, resulting in an inhomogeneous DW distribution in ACP-2, similar to results reported in this reference.[177]

Such inhomogeneity in optimized poling state occurs at a bulk scale (~ mm), which is challenging to observe with localized DW characterization methods. This potentially explains the conflicting results in the studies on domain observation in ACP PMN-PT single crystals. We believe that the continuous polarization reversal during ACP causes inhomogeneous electric field distribution within the material. The ACP-1 underwent 1~2 cycles of polarization switching, while ACP-2 underwent 40 cycles under the same electric field. Additionally, as discussed in SI Section S8, ACP-2 is more inhomogeneous than DCP-2,indicating inhomogeneity in polarization reversal. Similar inhomogeneity in electric field distribution has been observed in studies involving other ferroelectrics.[178–180]

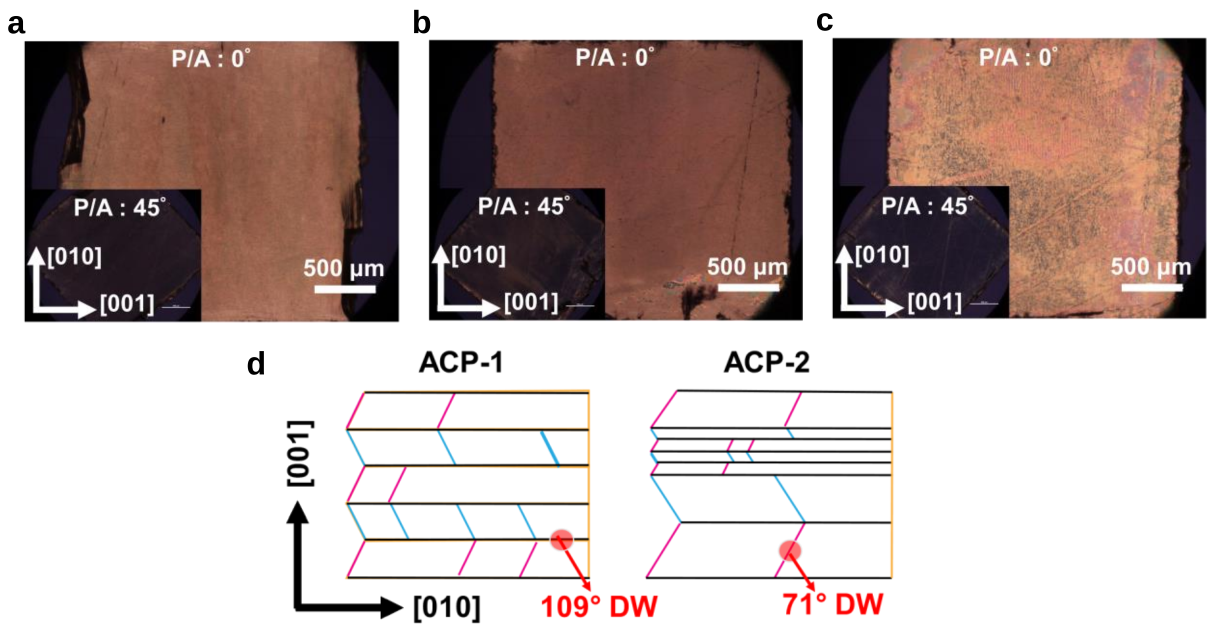

Figure 2.3 The PLM domain morphology of high-PT PMN-PT SCs at P/A = 0 (inset shows P/A = 45°) for (a) Unpoled (UP), (b) Intermediate AC-poled (ACP-1) along the [001] direction, and (c) Optimized AC-poled (ACP-2) along the [001] direction. All the crystals were polished down to a thickness of 0.2 mm for the PLM measurement. (d) The illustration of laminar domains (sandwich between 109° DWs) for the ACP-1 and ACP-2 single crystals poled along the [001] direction. The DW density of 71° DW decreases upon ACP. Based on the PLM observation, the ACP-1 shows homogenous domain size distribution in comparison to ACP-2.

The inherently disordered PMN-PT structure coupled with the large volume of single crystals employed in this study further facilitates the inhomogeneity in polarization reversal. [181,182] Determining the exact cause of inhomogeneity would require a dedicated study involving in-situ structural characterizations, which could be an interesting area for future research.

Next, we calculated the DW density distribution for the UP, ACP-1, and ACP-2 samples. (d) shows that ACP along the [001] direction leads to dominant 109° DWs forming laminar domains. As these 109° DWs are non-overlapping when observed along the (100) plane, the thickness of these laminar domains is a fair estimate for the variation in the domain size with the AC poling. The procedure for calculating the domain size and DW density is described in SI Section S5. Figure shows examples of the domains size distribution for the samples measured using PLM under crossed polars (P/A: 90°).

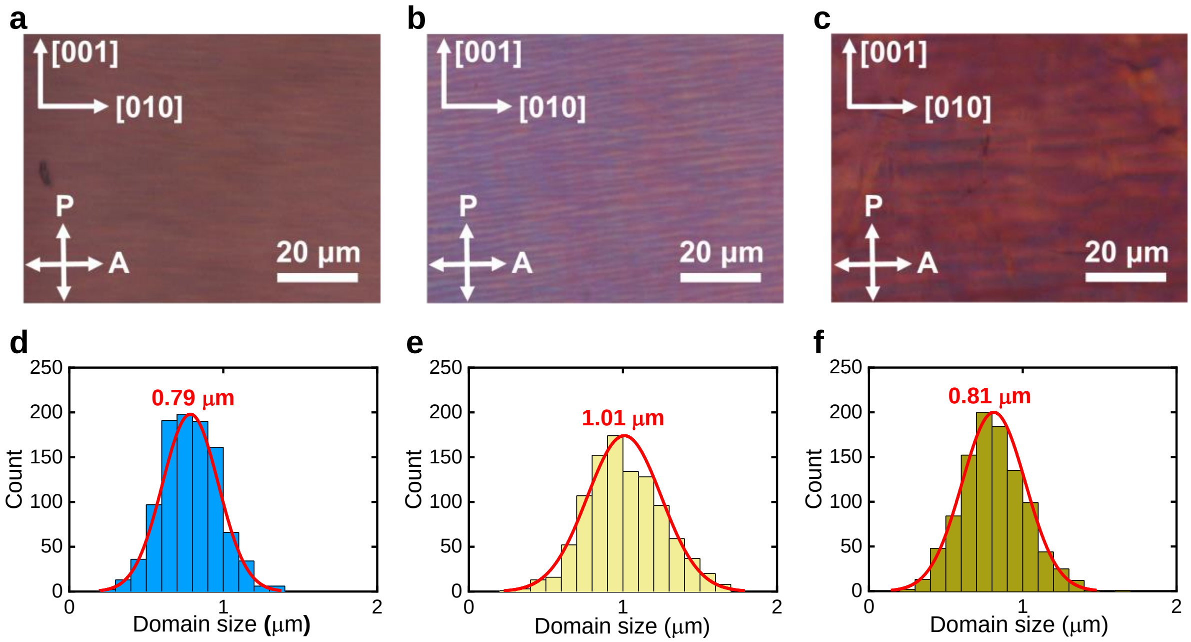

Figure 2.4 Characterization of domain size for high-PT PMN-PT single crystals. PLM image examples on the (100) plane for (a) UP, (b) intermediate ACP along the [001] direction (ACP-1), and (c) optimized ACP along the [001] direction (ACP-2). Distribution of laminar domain thickness for (d) UP, (e) ACP-1, and (f) ACP-2. The distribution is the analysis result from PLM images using three samples from nine different locations.

The calculated domain wall density for UP, ACP-1, and ACP-2 samples are $(2.48 \pm 0.10) \times 10^3$ μm^{-1}, $(1.73 \pm 0.08) \times 10^3$ μm^{-1} and $(2.70 \pm 0.25) \times 10^3$ μm^{-1}, respectively. The DW density agrees with the thermal modulation trend in (c). The UP and ACP-2 sample show similar thermal conductivity and hence similar DW density. Similarly, ACP-1 shows enhanced thermal conductivity owing to a reduced ferroelectric DW density. Also, the standard deviation in DW density for ACP-2 is much larger than the ACP-1 samples, which again reflects the increased inhomogeneity in domain size distribution. It is important to note that the DW density calculated from PLM for the UP sample only indicates the birefringent DW density, and the actual DW density can be slightly higher than the one calculated here. This also explains the slightly lower UP DW density compared to ACP-2 even though their thermal conductivity is similar.

2.5 Domain wall density measured by PLM

The inhomogeneity observed in ACP-2 emphasizes the need for bulk DW density characterization. Localized measurements may lead to smaller or higher DW density values that can lead to incorrect conclusions. To further validate our PLM measurements in the last section, we turn to bulk apparent birefringence measurement of the UP and ACP PMN-(30~33)PT samples using the QPLM experimental setup. More information regarding the QPLM is provided in SI Section S9. We compared the apparent birefringence of the UP, ACP-1, and ACP-2 samples. Theoretically, birefringence is the measurement of optical retardation in a crystal. The change in birefringence is influenced by the DW density and orientation [44,174].

Figure 2.5 shows the retardation maps and corresponding histograms for the UP, ACP-1, and ACP-2 samples. The average retardation (φ) is calculated over a 600 μm × 600 μm area for five different locations in the samples, which is sufficient to scan the bulk of the SC of size 2500 × 2500 μm. Based on φ, the apparent birefringence was calculated using Equation **Error! Reference source not found.** in section 4.4. The average apparent birefringence (Δn) is calculated to be 0.00069 for UP, 0.00057 for ACP-1, and 0.00062 for ACP-2 samples, respectively. In the case of the UP sample, the orientation of DW is random, as also illustrated in Figure 2.3 **(b)** and **(e)**, where the retardation map shows no specific orientation preference.

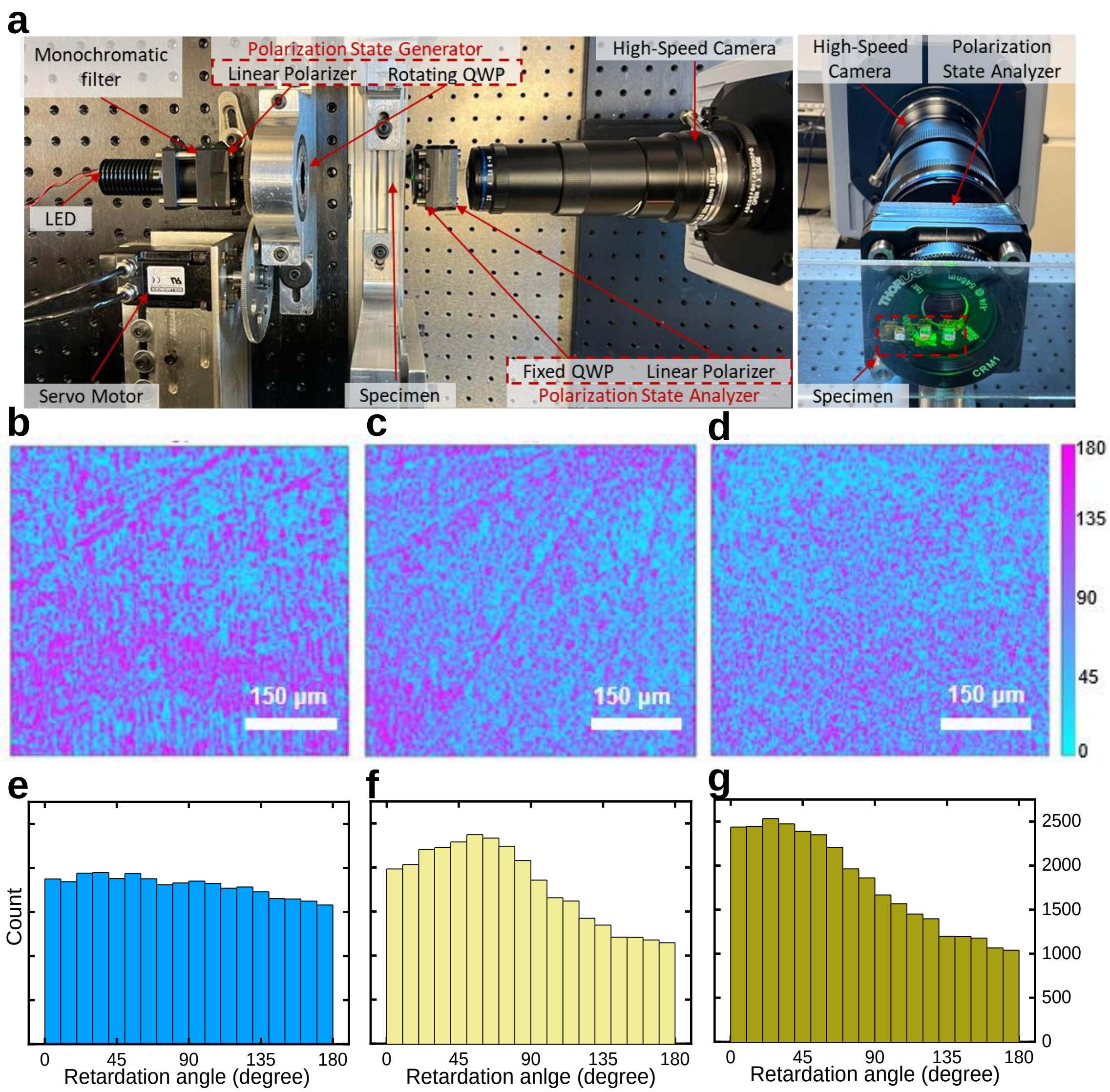

Figure 2.5 (a) Experimental setup of the QPLM measurement. Retardation maps (in degrees) obtained for (b) UP, (c) ACP-1, and (d) ACP-2 PMN-(30~33)PT SCs. The corresponding histograms for the retardation maps are also shown for (e) UP, (f) ACP-1, and (g) ACP-2 samples. The retardation maps and histograms were obtained for five locations on the samples and the average alignment degree (φ) value is used to calculate the apparent birefringence for each sample. The thickness of the UP, ACP-1 and ACP-2 sample is measured to be around 0.19 mm, 0.22 mm, and 0.18 mm, respectively.

The net retardation is thus expected to be the highest as compared to the ACP samples. For ACP, the presence of birefringent 109° DW primarily dictates the retardation observed in the samples. Naturally, a higher density of 109° DW will result in higher birefringence. This is exactly what we observed in our QPLM measurements, which indicates that the DW density in the case of ACP-2 is higher than ACP-1. This observation further reinforces the DW density contrast as observed by thermal conductivity modulation and PLM measurements.

We note that the birefringence reported in the QPLM is not the actual birefringence of the material. We measured the apparent birefringence of the samples, which is sensitive to small changes in birefringence between two samples. As the domain wall density changes by around 58% between ACP-1 and ACP-2, leading to an enhancement in thermal conductivity of 21%, the change in birefringence is also expected to be 58% or even lower. Therefore, QPLM was selected specifically because it is sensitive enough to detect such small changes in birefringence.

2.6 Ex-situ cyclic poling-unpoling test

Heat loss determination is vital for steady state measurements to ensure repeatability. In the current setup, the total heat input is divided into four pathways: diffusion in the PMN-PT single crystals, conduction loss into the insulation, convection loss to the ambience, and radiation loss. The total heat loss is calculated by subtracting the heat input from the heat diffused into the PMN-PT samples. The heat input is computed based on resistive heating. The diffused heat is evaluated by taking the thermal conductivity of the PMN-PT sample as measured by PTR and the temperature difference measured by the IR camera.

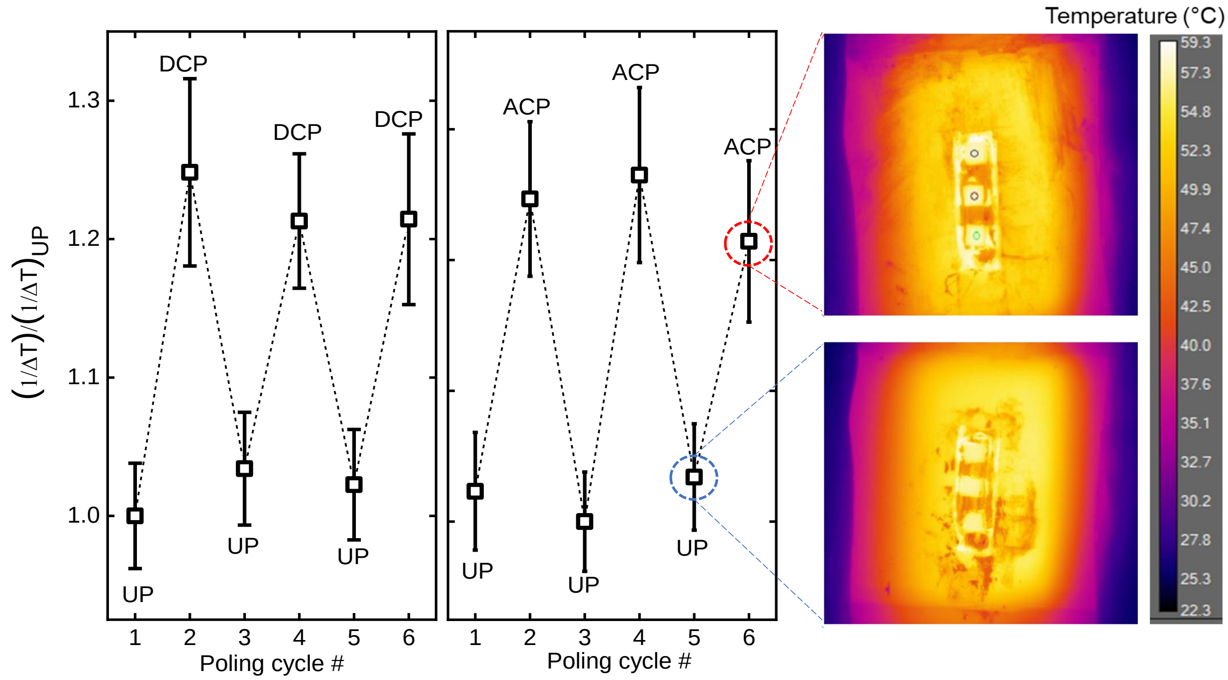

Figure 2.6 Ex-situ cyclic unpoling and poling (ACP and DCP) of PMN-(30~33)PT SCs. Left panel: Cyclic unpoling and DCP test. Middle panel: Cyclic unpoling and ACP test. Right panel: IR camera images of the three UP and ACP samples. The plots represent the average temperature difference of the three samples. During each test, the power input to the heater is slightly adjusted to ensure a similar temperature rise. The unpoling and poling test was performed three times to ensure repeatability and confirm similar heat loss throughout the measurements.

As we compared ΔT among different states (e.g., UP, ACP-1, ACP-2) in this study, it is vital to ensure that the heat loss is the same in all the measurements. The difference between the total heat loss for the UP (~3.87 mW) and ACP-1 (~3.79 mW) is around 2.1%, which is much lower than the observed rise in ΔT (~21%). Additionally, we conducted an ex-situ repeatability test on PMN-(30-33)PT single crystals to validate this claim. We measured the same crystals to eliminate any potential influence of varying compositions. Before the IR camera test, the crystals were taken off the heater and thermally depoled for about two hours. Once completely depoled, the UP samples were re-attached to the heater using silver paste and tested under the IR camera. The samples were then poled and tested in the same way. The poling conditions and measured piezoelectric coefficient are shown in Section. We conducted this test three times to ensure repeatability. demonstrates consistent thermal contrast for both ACP and DCP PMN-(30-33)PT SCs. The UP samples show consistent reduction in thermal conductivity, which indicates that the domains are completely reoriented The maximum thermal contrast in one of the UP-ACP-UP cycles reaches 27%, and the average is 22% over the three cycles. In the UP-DCP-UP test, the maximum modulation is 25%, with an average of 20%.This test confirms that heat loss is similar throughout our measurements and highlights the reliability of the relaxor-based ferroelectric thermal switch.

2.7 Conclusion

We have demonstrated the thermal conductivity modulation in bulk scale (millimeter thick) using ferroelectric PMN-PT SCs. We observed a maximum thermal conductivity enhancement of ≈25% for the PMN-(30-33) PT and ≈12% for the PMN-(27-30) PT SCs using AC poling. The anisotropic steady state temperature difference measurements suggest that the poling direction exhibits the maximum thermal conductivity modulation (maximum DW density contrast). The DW density measurement using PLM and apparent birefringence measurement using QPLM validate the observed thermal conductivity contrast. The PLM also reveals the increased inhomogeneity in domain size distribution in the [001] AC-poled PMN-(30-33) PT SCs under optimized poling conditions. Comparing the thermal conductivity measurement results with piezoelectric property (d_{33}) enhancement reveals that DW density reaches a minimum at intermediate poling states (characterized by an intermittentd_{33} value :$0<d_{33}<d_{33,max}$).Our observations also indicate that the increasing DW density leads to a higher domain size inhomogeneity, particularly for ACP single

crystals. At optimized poling (maximum d_{33}), the inhomogeneity dominates, which results in increased overall DW density compared to intermediate poling states. This study highlights the relevance of thermal conductivity characterization as an alternative tool to understand the variation of domain walls in future ferroelectric studies. From the thermal conductivity modulation perspective, such relaxor-based ferroelectric thermal switches can offer remarkable control over thermal transport in a solid-state device, not limited to only the bipolar ON and OFF states as in conventional switches, with the aid of AC poling. Considering a unit of single crystal produces an around 20% reduction in heat transfer coupled with the ease of applying electric field, an array of single crystals would lead to a considerable reduction in overall heat transfer, ideal for solid-state thermal management applications.

CHAPTER 3

Phonon mean free path distribution in single-crystalline barium titanate

The last chapter demonstrated thermal conductivity modulation in bulk scale PMN-PT single crystals. It is only natural to expect similar behavior in perovskite thin films as well. The question remains however, how small the domains need to be to observe large thermal conductivity contrast. Such information can be accessed by evaluating the phonon mean free path (MFP) distribution. This presents the understanding of phonon MFP distribution in BTO, a prototypical perovskite used in several nanoscale applications. Surprisingly, even after decades of research on thermal properties, the accurate MFP prediction is not present for a lot of oxide perovskite materials like BTO. Information of MFP distribution aids in nano structuring in thermoelectric materials and avoids incorrect assumptions about thermal conductivity scaling. Further, MFP distribution can also be used to explore extreme thermal transport regimes such as super-diffusive and quasi-ballistic phonon transport.

3.1 Introduction

Nanosized perovskite ferroelectrics are widely employed in several electromechanical, photonics, and thermoelectric applications. Scaling of ferroelectric materials entails a severe reduction in the lattice (phonon) thermal conductivity, particularly at sub-100 nm length scales. Such thermal conductivity reduction can be accurately predicted using the information of phonon mean free path (MFP) distribution. The current understanding of phonon MFP distribution in perovskite ferroelectrics is still inconclusive despite the critical thermal management implications. Here, we have grown high-quality single-crystalline barium titanate (BTO) thin films, a representative perovskite ferroelectric material, at several thicknesses. Using experimental thermal conductivity measurements and first-principles based modeling (including four-phonon scattering), we determine the phonon MFP distribution in BTO. The simulation results agree with the measured thickness-dependent thermal conductivity. Our results show that the phonons with sub-100 nm MFP dominate the thermal transport in BTO, and phonons with MFP exceeding 10 nm contribute about 35% to the total thermal conductivity, in significant contrast to previously published experimental results. Our experimentally validated phonon MFP distribution is consistent with the theoretical predictions of other complex crystals with strong anharmonicity. This work paves the way for thermal management in nanostructured and ferroelectric-domain-engineered systems for oxide perovskite-based functional materials.

3.2 Determination of thermal conductivity for BTO

The thermal conductivity of BTO at room temperature is determined using the time-domain thermoreflectance method (TDTR).[183,184] Figure 3.1(a) shows the schematics of this method, with more details in the Methods section. A thin layer of Al is deposited on top serving as both the heater and the reflectivity-temperature transducer. The ultrafast laser beam is divided into pump beam and probe beam, where the pump beam heats the sample surface, and the probe beam measures the corresponding surface temperature rise via the surface reflectivity change. The time delay between the two beams allows us to track the transient temperature change upon heating, the rate of which depends on the thermal properties of the unknown layer (e.g., BTO layer). Since TDTR is an optical method where surface reflectance is essential, the surface of the grown sample needs to be atomically smooth with a typical requirement of R.M.S. roughness < 15 nm. Figure 3.1(b) shows the atomic force microscopy (AFM) scan of the surface on a representative sample and the surface roughness is below 1 nm. Such a smooth surface results from the high-quality MBE growth of BTO on top of the STO substrate.

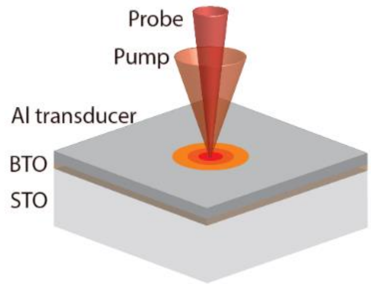

(a)

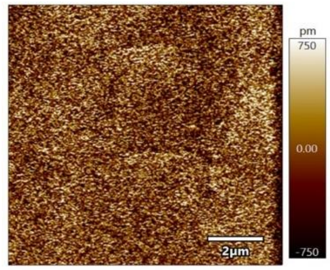

(b)

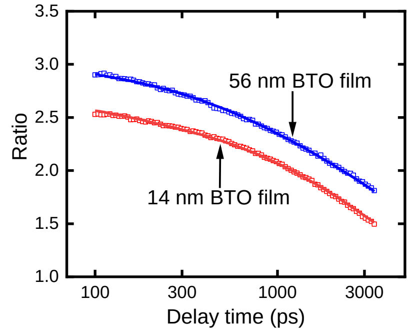

(c)

Figure 3.1 a) Schematic of thermal conductivity measurement of BTO thin films using TDTR. b) Surface morphology of the 14 nm BTO film scanned by AFM. The R.M.S. roughness of the film is ≈0.3 nm indicating a smooth BTO growth over the STO substrate. c) TDTR normalized signal (ratio) for the 14 nm and 56 nm BTO thin films obtained using experiments (symbols), which is fitted with the heat diffusion model (solid lines). With increasing film thickness, the thermal resistance increases, which results in a larger ratio.

Figure 3.1(c) shows two sets of typical TDTR experimental data where the normalized signals (also termed as "ratio") are plotted as a function of the delay time between the two beams. The cross-plane (i.e., through-thickness) thermal conductivities (k) of the single crystalline BTO films were obtained by fitting the experimental data from TDTR with the heat diffusion model. In theory, TDTR fitting involves the influence of several geometric, laser, and thermophysical parameters: the thickness of each layer, thermal conductivity and heat capacity of each layer, and interfacial thermal conductances between Al-BTO ($G_{Al\text{-}BTO}$) and BTO-STO ($G_{BTO\text{-}STO}$), and the laser spot size.

The thickness of the Al transducer is determined using picosecond acoustics.[185] The thickness of BTO is controlled and measured during growth. The thermal conductivity and heat capacity of Al are taken from literature, as in our previous work. [186] The heat capacity of BTO is taken from literature. [94] We measured the thermal conductivity of bare STO substrate ($k_{STO} = 10.6 \pm 0.4$ W m^{-1} K^{-1}), which agrees with the data reported previously. [89] The heat capacity of STO is adopted from literature. [187] Given the laser spot size in our experiment (5×, 1/e^2 Gaussian beam radius ≈ 10.5 μm) is relatively large, the influence of this parameter on the signal is negligible. All these determined inputs leave us with three relevant undetermined thermophysical parameters in the fitting, the k_{BTO}, $G_{Al\text{-}BTO}$, and $G_{BTO\text{-}STO}$.

To measure the k_{BTO} with a higher accuracy, we conducted a sensitivity analysis and then measured the samples with their selected modulation frequencies of pump beam. When varying the modulation frequency of pump beam, the thermal waves will penetrate different depths into the sample, thus changing the relative sensitivities of these undetermined parameters. We calculated the sensitivity (S) of the three parameters at three representative modulation frequencies using Equation (1),

$$S_\alpha = \frac{\partial}{\partial \alpha}\left(\frac{\ln R_\alpha}{\ln \alpha}\right) \quad , \tag{1}$$

where α is the undetermined thermophysical parameter and R is the TDTR signal (ratio). Figure 3.2 shows the sensitivity analysis results. For the thinnest sample (14 nm-thick), at the low modulation frequencies, the signal is more sensitive to k_{BTO}. However, the sensitivities of the interfaces (i.e., $G_{BTO\text{-}STO}$ and $G_{Al\text{-}BTO}$) are also comparable to that of k_{BTO}. Extracting thermal conductivity of the BTO film, without any influence of interfaces, is thus challenging even with a multifrequency-fitting approach (used in our previous work[87,184]). At low modulation frequencies, other parameters including the specific heat of BTO, STO, and Al transducer, thermal conductivity of STO, and $G_{BTO\text{-}STO}$ also become more sensitive. Thus, the total uncertainty (more details in the next paragraphs) in determining k_{BTO} increases as well. In that regard, we chose a modulation frequency of 3.85 MHz for thinner samples (BTO film thickness < 40 nm) to balance the trade-off between the uncertainty due to k_{BTO} sensitivity and uncertainties in other parameters. As the BTO film thickness increases, a relatively higher modulation frequency is preferred because of a smaller thermal penetration depth that leads to predominantly a higher sensitivity of the signal to k_{BTO}. Thus, we selected a modulation frequency of 7.2 MHz for thicker samples (BTO film thickness > 40 nm).

In our case, as BTO is atomically grown on the STO substrate and the surface smoothness is ensured using RHEED, the interface can be assumed to be atomically smooth. Thus, we use the diffusive mismatch model (DMM) to calculate the interfacial thermal conductance between the BTO and STO interface at room temperature.[188] We have demonstrated in our previous work that the DMM predicted interfacial thermal conductance is more accurate using first-principles predicted full phonon dispersion relations compared with other approaches (e.g., using the Debye approximations).

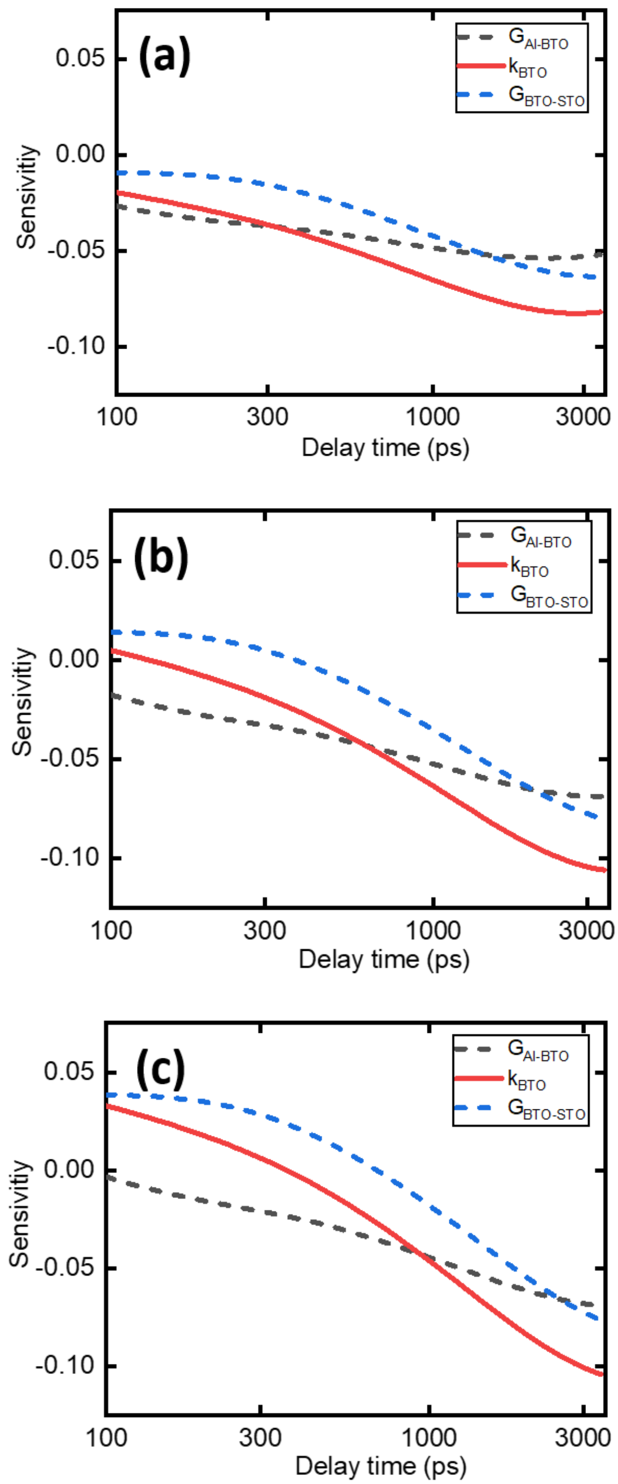

Figure 3.2 Sensitivity analysis for optimizing the measurement conditions. Sensitivity plots for 14 nm-thick BTO thin film at a) 1 MHz, b) 3.85 MHz, and c) 7.2 MHz modulation frequencies.

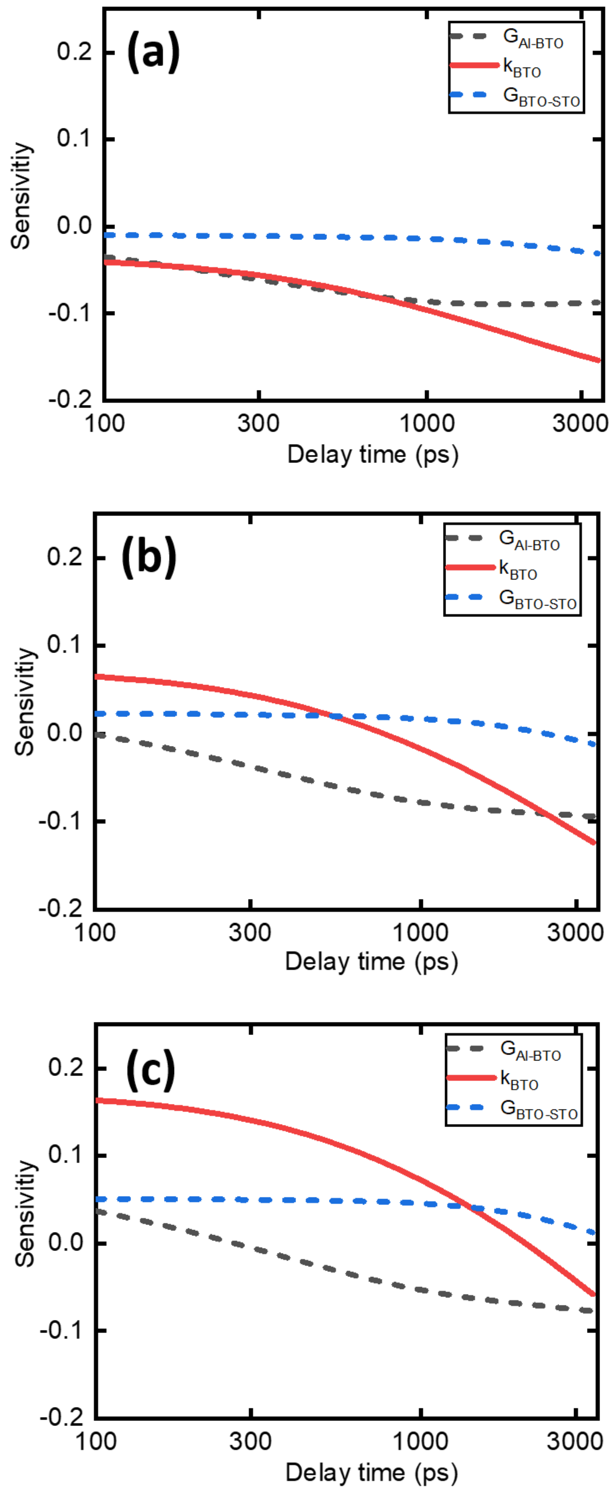

Figure 3.3 Sensitivity analysis for optimizing the measurement conditions. Sensitivity plots for 56 nm-thick BTO thin film at a) 1 MHz, b) 3.85 MHz, and c) 7.2 MHz modulation frequencies.

The second-order force constants and dispersion relations for BTO and STO were extracted from the first-principles method (with details in the Methods). The calculated interfacial thermal conductance at room temperature for the BTO-STO interface is 250 MW m^{-2} K^{-1}. Using the DMM calculated $G_{BTO\text{-}STO}$ and given that both $G_{Al\text{-}BTO}$ and k_{BTO} are sensitive depending on the BTO thickness, we define a parameter σ, as in our previous work, to quantify the goodness of fit.[189] σ is the summation of the standard deviation between the model and experimental data, at the modulation frequency (3.85 and 7.2 MHz in our case).

Figure 3.4 shows the contour of 2σ (95 % confidence interval) as a function of $G_{Al\text{-}BTO}$ and k_{BTO} for the BTO thin films. As shown in the sensitivity plots, the k_{BTO} is the most sensitive fitting parameter for thinner films at 3.85 MHz modulation, which leads to low uncertainty in k_{BTO}. This uncertainty is a function of the signal to noise ratio and the quality of fit between the thermal model and experimental data. The total uncertainty in $k_{BTO,}$ shown in Figure 3.5, also includes the systematic errors due to uncertainties in transducer film thickness, thermal properties of transducer film and substrate, spot size, and the BTO-STO interfacial conductance. Even though we used the first-principles-enabled DMM to predict $G_{BTO\text{-}STO}$, we have considered a 20% input uncertainty for this parameter when computing the total uncertainty.

For the interfacial thermal conductance between Al and BTO, as the BTO film thickness increases, sensitivity plots show an increased dependence on $G_{Al\text{-}BTO}$, which translates to a lower uncertainty in the parameter. The range of our measured $G_{Al\text{-}BTO}$ lies within ~ 50–250 MW m^{-2} K^{-1} for films with a thickness above 20 nm, which is reasonable for the interfacial thermal conductance for an evaporated metal–dielectric contact.[190,191] The high $G_{Al\text{-}BTO}$ for the 14 nm BTO can be related to the growth of BTO, Al transducer deposition, and the low sensitivity of this parameter. Because the thermal evaporation of Aluminum on top of the BTO surface depends strongly on the evaporation condition and the quality of the sample surface, the thickness-dependent interfacial thermal conductance between Al and BTO does not lead to any meaningful conclusion at such a small film thickness.

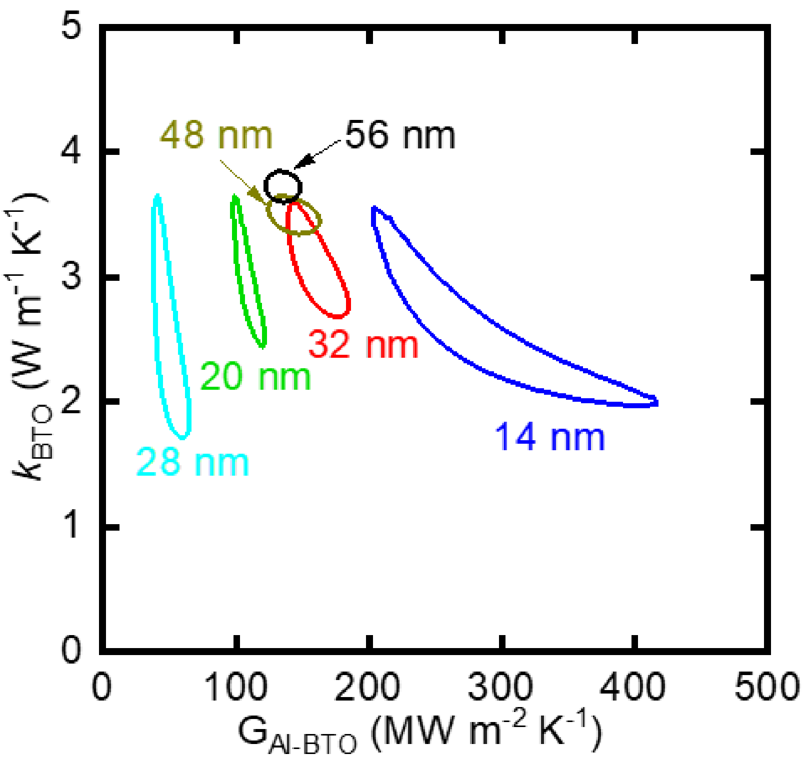

Figure 3.4 Contour plot of 2σ as a function of k_{BTO} and $G_{Al\text{-}BTO}$. For thinner films, the measured signal is less sensitive to the top interface, which translates to a larger uncertainty in $G_{Al\text{-}BTO}$.

Figure 3.5 shows the fitted TDTR thermal conductivity of BTO thin films. We also measured the thermal conductivity of a bulk BTO single crystal (double sided polished procured from MTI Corporation) ($k_{BTO,bulk}$ ~ 4.05 ± 0.35 W^{-1} m^{-1} K) using TDTR. Substantial reduction in thermal conductivity is observed (~ 30 %) for the thinnest sample compared to bulk single crystal. Further, we observed a much steeper rise in thermal conductivity for the sub-100 nm thin films, indicating a shorter MFP in comparison to BTO thin films reported in literature.

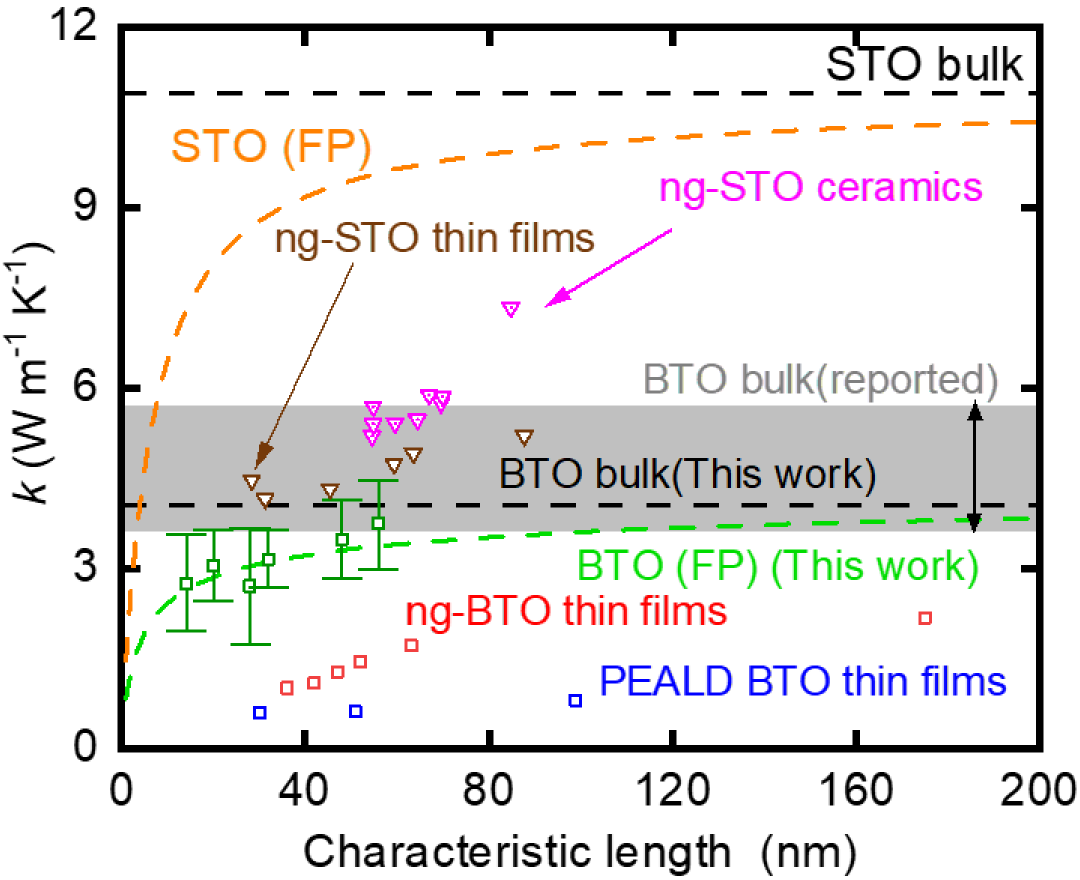

Figure 3.5 Thermal conductivity of BTO as a function of characteristic length. The characteristic length is equal to film thickness for this work (green squares) and PEALD BTO thin films (blue squares)[96], and grain size for ng-BTO thin films (red squares)[95], ng-STO thin films (brown triangles)[89] and ng-STO ceramics (pink triangles)[100]. The bulk value of BTO measured using a single crystal (black dashed line) is also shown. The reported values of BTO are also presented for reference (gray region).[54,91,94] First-principles (FP) predicted thermal conductivity as a function of characteristic length for STO (orange dashed line)[101] and BTO (green dashed line). The predicted bulk value for STO is the top black dashed line. The error bars in the fitted BTO results are a summation of the 2σ uncertainty in k_{BTO} and standard TDTR error.

3.3 Modeling phonon transport in BTO

To understand the phonon transport and resolve the phonon MFP distribution in BTO, we performed first-principles based modeling, including using density functional theory to optimize the unit cell, performing *ab initio* molecular dynamics simulations to obtain snapshots of atomic configurations, and Boltzmann transport equation to calculate phonon transport properties (including phonon scattering rates) and thermal conductivity.

Figure 3.6(a) shows the calculated phonon dispersion curve for BTO. No negative frequencies appear in the dispersion curve , which indicates a proper relaxation of the cell. Figure 3.6(b) shows the phonon lifetime as a function of phonon frequency in BTO. The phonon lifetime is shorter when taking four-phonon scattering processes into account. This observation is consistent with the studies in other materials, including Si[192], PbTe[193], BAs[194], etc., where the inclusion of four-phonon scattering processes will decrease the overall phonon lifetime.

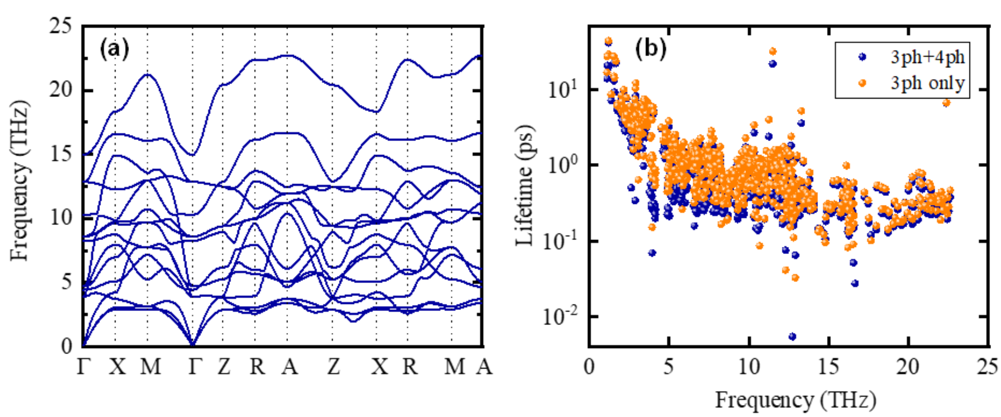

Figure 3.6 Phonon transport properties calculation results of BTO. a) Phonon dispersion relations. b) Phonon lifetime plotted in the log scale as a function of phonon frequency. The blue dots are phonon lifetimes considering both the three- and four-phonon scattering processes in the calculation. The orange dots only consider the three-phonon scattering processes.

3.4 Phonon MFP distribution in BTO and comparison with other complex crystals

When comparing the modeling and measurement results in the cross-plane thermal conductivity of BTO, we used a suppression function in the cross-plane direction to convert from phonon-MFP-dependent thermal conductivity to film-thickness-dependent thermal conductivity. The details are described in Methods 4.4 and the result is plotted in Figure 3.7. The predicted thickness-dependent thermal conductivity in BTO at room temperature matches well with our measurement results, which validates the phonon MFP distribution in BTO.

Previous TDTR measurements on the nanograined-BTO (ng-BTO) thin film shows more than two-fold reduction in thermal conductivity compared to bulk single crystal, even for the epitaxial 175 nm thin film. [95] An even higher reduction in thermal conductivity is observed for the plasma-enhanced atomic layer deposition (PEALD) grown BTO thin films. [96,97] Both measurements are not consistent with our first-principles thermal conductivity predictions. Similar discrepancy between the experimental measurements and first-principles predictions is also observed in STO, also presented in Figure 3.5.

We believe the reason for observing such large discrepancies are two-fold, firstly, the growth of epitaxial film of perovskite oxides on a lattice mismatched substrate (e.g., Si) incurs structural imperfections and presence of large amorphous regions in the film. [195–197] The actual phonon MFP thus becomes much smaller than the film thickness. This is observed in recent work during the growth of BTO on a Si substrate where the low thermal conductivity is attributed to mixed amorphous and crystalline phases.[96,97] Secondly, the experimental discrepancy can also be accounted by considering the uncertainties in accurately determining the thermal conductivity of BTO film using TDTR measurement. The measurement is not only sensitive to the thermal conductivity of BTO, but also to the interfacial thermal conductances. Lumping interfacial thermal conductance values together results in an effective thermal conductivity, that does not reflect the inherent k_{BTO}. Again, assuming inappropriate value for $k_{BTO\text{-}STO}$ can result in lower-than-expected k_{BTO} values.

Figure 3.7 shows a summary of the theoretically predicted normalized cumulative thermal conductivity (k_L/k_{bulk}) as a function of phonon MFP in complex crystals, where either the crystal has a complex chemical composition or atomic structure, and their strong anharmonicity has been demonstrated in the literature. Considering the differences in chemical composition and atomic structure in these complex crystals, we do not expect all the phonon MFP distribution curves will overlap.

However, we surprisingly find that these curves share a similar shape and a few common features:

(1) Phonons with MFPs longer than 1-10 nm still contribute significantly (20%-60%) to the total thermal conductivity, which is contrary to the phonon MFP estimated from the simple kinetic theory based on phonon gas model.

(2) Phonons with MFPs longer than 100 nm do not contribute substantially to the thermal conductivity, with <10% contribution in most complex crystals (only two exceptions in Bi_2Te_3 (≈25%) and $BaHfO_3$ (≈18%)).

(3) Phonons that contribute to the thermal conductivity have an MFP spanning in about two orders of magnitude. The slope on the plot is the highest around phonon MFP=10 nm, which means the change in thermal conductivity is large when including or removing phonons with MFP around this range (5-20 nm). If these complex crystals are made into thin films, their thermal conductivity cannot be assumed the same in this range of film thickness when phonon-boundary scattering becomes important.

These common features found in complex crystals with strong anharmonicity are in contrast with simple crystals with weak anharmonicity. For simple crystals with only one or two atoms in the cell and a simple cell structure, when the anharmonicity is weak, the phonon MFPs can be much higher (>> 100 nm) and these phonons contribute significantly to the thermal conductivity. For example, in Si and sapphire (Al_2O_3), phonons with MFP larger than 100 nm contribute more than 50% to thermal conductivity and phonons with MFP smaller than 10 nm contribute negligibly. Phonons that contribute to the thermal conductivity have an MFP spanning in more than two orders of magnitude (e.g., 10 nm to 10^5 nm in Si).

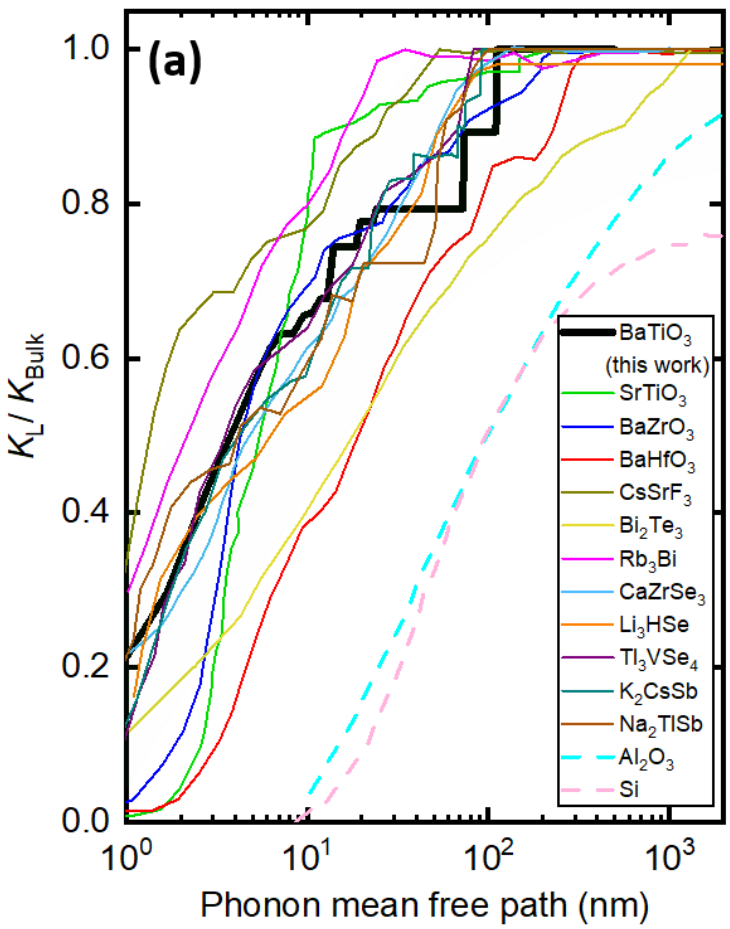

Figure 3.7 Comparison among the phonon MFP distribution curves in complex crystals with strong anharmonicity predicted at 300 K using first-principles based calculations.

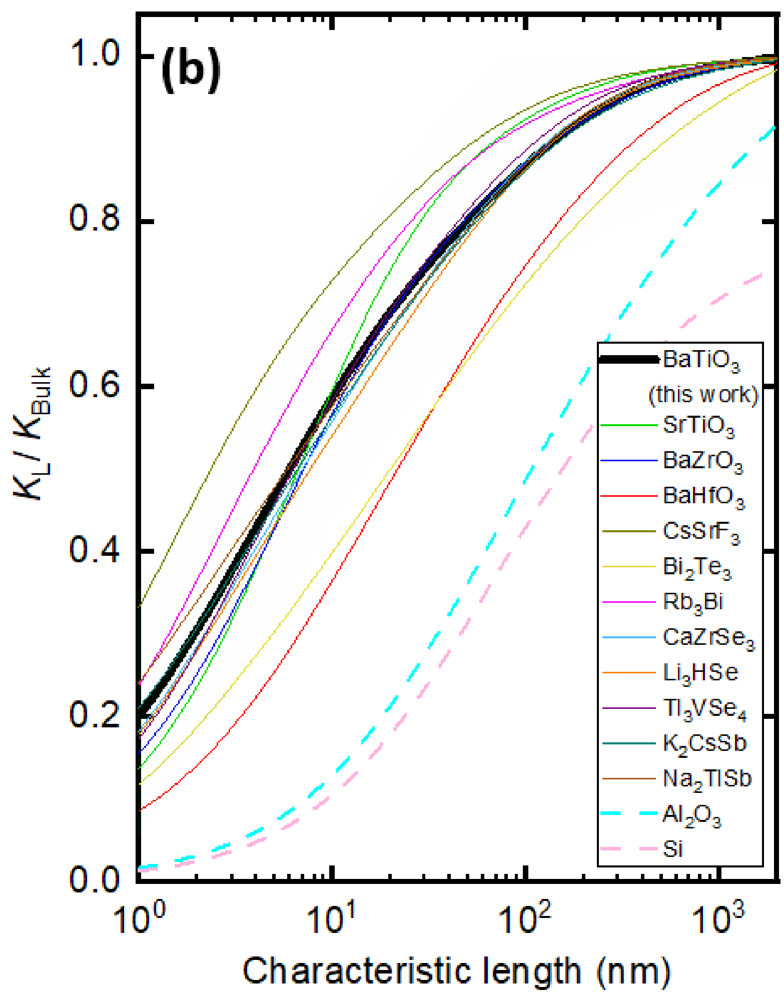

Figure 3.8 Comparison among thermal conductivity variation as a function of characteristic length in complex crystals. The MFP is transformed to the characteristic length using the suppression function as described in Section 4.4. The thermal conductivity can be tailored by controlling the characteristic length scale in the material, which can be the grain size, thin film thickness, or the limiting size of nanostructure. The data for complex crystals is taken from the following references: $SrTiO_3$, $BaZrO_3$[198], $BaHfO_3$[199], $CsSrF_3$[199], Bi_2Te_3[87], Rb_3Bi[200], $CaZrSe_3$[201], Li_3HSe[202], Tl_3VSe_4[203], and K_2CsSb[204]. Two examples of simple crystals with relatively weak anharmonicity are also included here: Al_2O_3 (Sapphire)[205] and Si[206]. The green highlighted area indicates the 80% prediction interval for the phonon MFP distribution of BTO.

This finding agrees with a recent work where Knoop et al.[207] calculated the thermal conductivity and anharmonicity of crystalline solids using the fully anharmonic *ab initio* Green-Kubo first principles method. They found that the intrinsic strong anharmonic crystals will lead to a low thermal conductivity.

The MFP-dependent thermal conductivity is converted to characteristic-length-dependent thermal conductivity using the suppression function described in Section 4.4. The characteristic length can be the average size of grains in polycrystalline materials, film thickness in thin films, and limiting or feature size of nanostructures. Figure 3.8 shows the suppressed thermal conductivity as a function of characteristic length, which serves as a guide for researchers to estimate the variation in thermal conductivity, a key piece of information in several applications. For instance, in thermoelectric materials, controlling the characteristic length to ~10 nm can lead to a 4-5 fold increase in thermoelectric figure of merit, due to the substantial reduction in thermal conductivity as shown in Figure 15. [61,63,65] Further, the length-dependent thermal conductivity is also useful in developing thermal switches that exhibit dynamic modulation of thermal transport using ferroelectric domain wall engineering. [1] The average size of ferroelectric domains can be selected based on the information provided in Figure 3.8.

3.5 Conclusion

We measured the cross-plane thermal conductivity of MBE-grown single-crystalline BTO thin films with a thickness of 14 – 56 nm at room temperature. The experimentally observed phonon mean free path distribution is corroborated by first-principles based predictions. We find that, on one hand, phonons with mean free paths larger than 100 nm contribute negligibly to thermal conductivity, contrary to the recent experimental observations. On the other hand, phonons with mean free paths larger than 10 nm contributes significantly (≈35%) to the total thermal conductivity, contrary to the kinetic theory based on the phonon gas model. The first-principles based calculations reveal that the four-phonon scattering process is non-negligible for BTO, even at room temperature, which is likely due to the strong anharmonicity in the oxide perovskite structure. Considering the similarity in the phonon mean free path distribution with other strongly anharmonic crystals, this result will provide insights and a design guide on the thermal transport in ferroelectric materials and complex crystals. Our work paves the way for thermal management in nanostructured and ferroelectric-domain-engineered systems for a wide range of oxide perovskite based functional materials (e.g., ferroelectric materials, thermoelectric materials).

CHAPTER 4

Tuning thermal transport and mechanical properties of mixed achiral and chiral 2D hybrid perovskites

The perovskite materials considered so far are purely inorganic. This chapter introduces a unique class of materials known as Hybrid organic inorganic perovskite (HOIP). These materials have already surpassed the photovoltaic efficiency of currently commercialized solar cell materials. Further, they are excellent candidates for thermoelectric, optical and electronic applications. Implementation of these materials on a device level requires a thorough understanding of their thermal conductivity. This study identifies the parameters that affect the thermal conductivity in 2D HOIP thin films. We prepared and measured different films that led to different thermal conductivity modulation. The organic-organic interface plays a dominant role in determining thermal conductivity in these materials.

4.1 Introduction

2D Hybrid organic inorganic perovskites (HOIP) are potential candidates for several industrial applications. Implementation of these materials at a device level demands a comprehensive understanding of their thermal conductivity to mitigate thermal management challenges and ensure long term device stability. Here, we prepared 12 different 2D HOIP thin films by changing the organic cations comprising pure achiral, mixed achiral, mixed chiral and pure chiral. The thermal conductivity of the pure achiral 2D HOIP is mostly contingent on the length of organic layer and the thermal conductance between the organic layers. In mixed achiral 2D HOIP, the thermal conductivity is largely determined by the length of organic layer and the CH--π interaction between organic cations. Using a combination of pure and mixed achiral 2D HOIPs, an unprecedented interlayer dependence of thermal conductivity is clearly observed. Introducing chirality in the 2D HOIP thin films engenders unique structural changes which stabilizes the thermal conductivity and breaks the interlayer dependence. The thermal conductivity of all the mixed chiral 2D HOIP is same regardless of the achiral organic cation suggesting the dominance of organic-organic thermal conductance in determining thermal transport. The thermal conductivity of pure chiral 2D HOIP is higher than the mixed chiral highlighting their candidacy in photovoltaic devices.

4.2 Structural characterization of 2D HOIP thin films

The 2D HOIP structure comprises alternating layers of inorganic octahedra separated by the weakly bonded organic cations with the inorganic-organic and organic-organic interactions influencing the material's physical properties. In general, thermal transport is influenced by four major thermal resistances, resistance due to inorganic layer, thermal conductance across the inorganic and organic layer, resistance of the organic layer and the organic-organic thermal conductance. In my case, I choose the inorganic layer the same in all 2D HOIPs, so the inorganic and inorganic-organic thermal resistances are also similar, thereby eliminating two parameters in the model. One objective of this study is to explore the impact of organic resistance and organic-organic conductance on thermal conductivity. In particular, thermal transport in 2D HOIPs is highly sensitive to organic-organic interactions, which are influenced by the selection of organic cations. Figure 4.2(a) shows the structure of an achiral alkyl-alkyl 2D HOIP and Figure 4.2(b) shows the structure of a half-chiral alkyl-aryl 2D HOIP. This is similar to the case of polymers. In alkyl-alkyl 2D HOIPs, the thermal conductance across alkyl-alkyl chains dictates the thermal transport between the two inorganic layers.

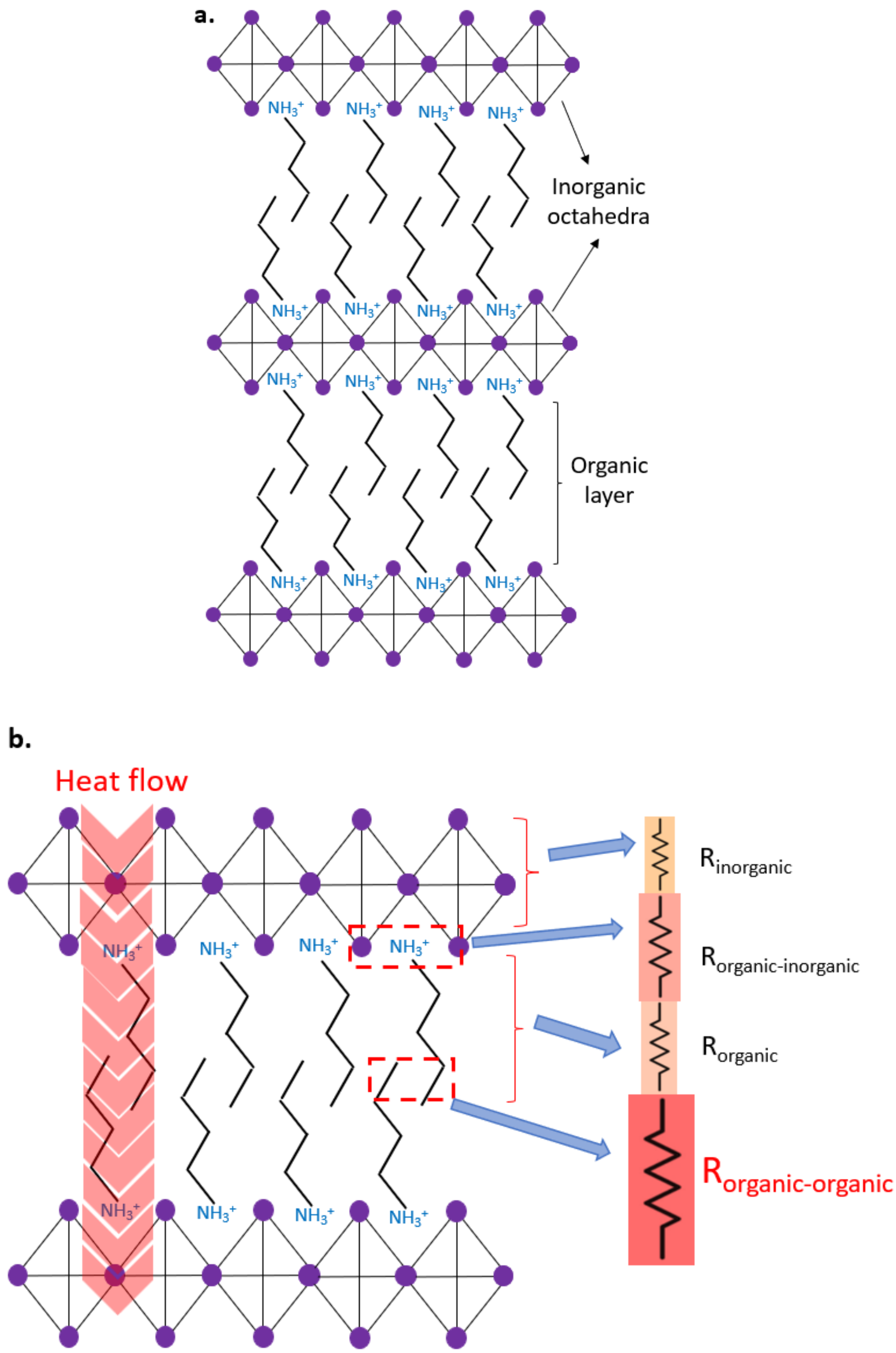

Figure 4.1 (a) Schematic of structure of 2D HOIP comprising of inorganic octahedral layer separated by weakly bonded organic cations. (b) Thermal resistance network diagram of the 2D HOIP structure. Four major thermal resistances impede the heat transfer in the material.

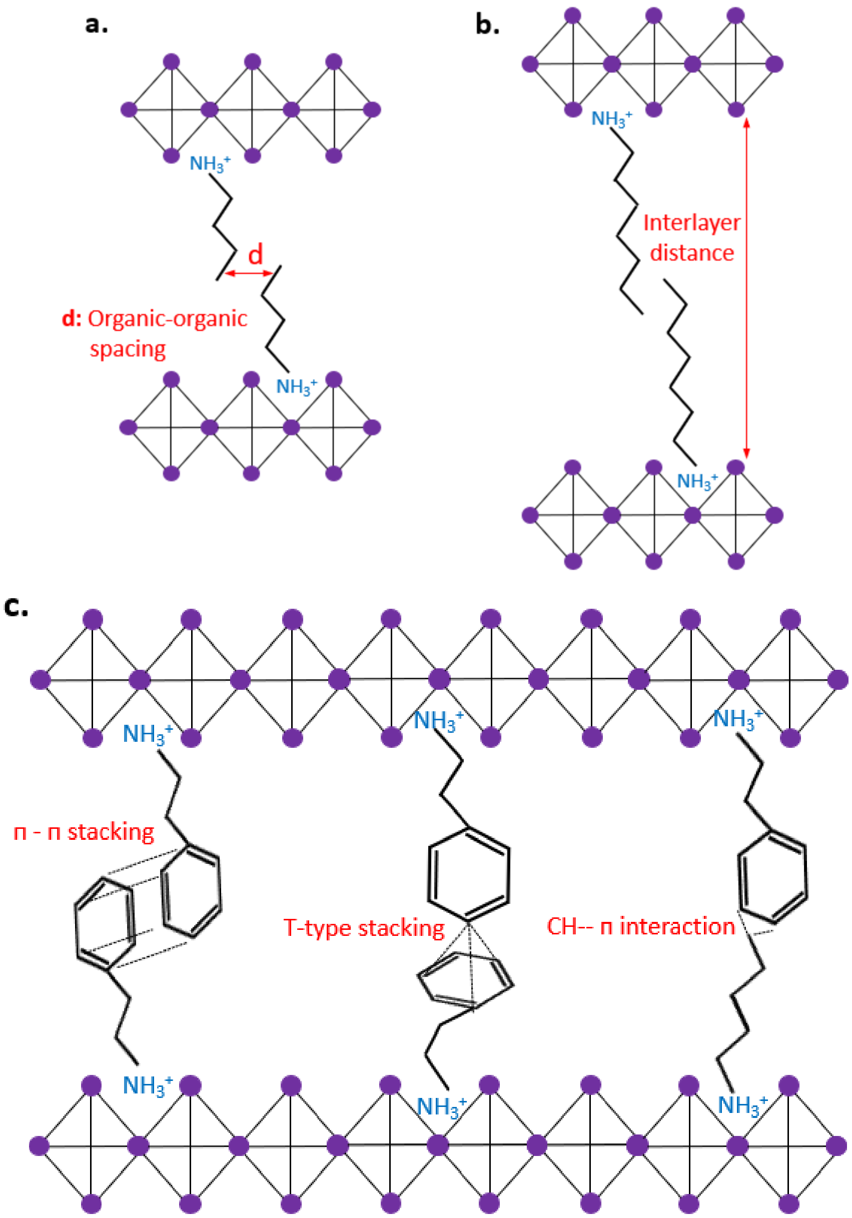

Figure 4.2 Identification of factors predominantly affecting the thermal conductivity in 2D HOIPs. The thermal resistance in the organic layer and the organic-organic thermal conductance are key in determining thermal conductivity of 2D HOIPs. (a) The spacing between the organic cations affects the thermal conductance of the organic-organic interface (b) The interlayer distance changes the group velocity of phonons and (c) different stacking in benzene rings leads to different thermal conductivity in the 2D HOIPs

The distance between organic cations and the amount of interdigitation primarily dictates the alkyl-alkyl interaction. Similarly, thermal transport is mostly dictated by the alkyl-aryl interaction in the case of mixed alkyl-aryl type 2D HOIPs. The orientation of benzene ring relative to the alkyl chain and distance between the organic cations primarily influence the alkyl-aryl thermal conductance. In the case of aryl-aryl type 2D HOIPs (for instance, $[PEA]_2PbI_4$), the orientation of two benzene rings relative to one another and the distance between them impacts the thermal conductance between them. The structure of the 2D HOIPs thus partially explain the thermal conductivity of different 2D HOIP thin films.

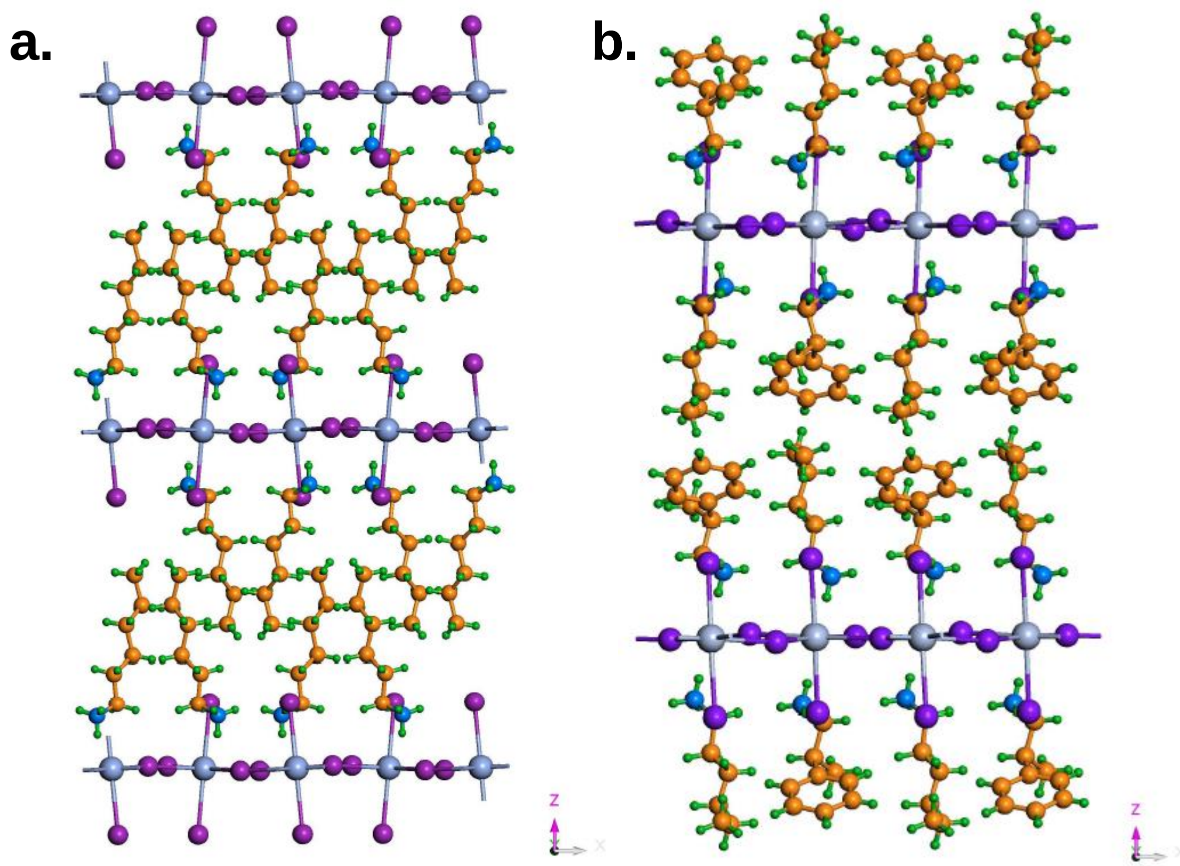

Figure 4.3 Structure of 2D HOIP thin films (a) Achiral $[C_6A]_2PbI_4$ and (b) Half-chiral $[C_6A][SMePEA]PbI_4$

Table 1 Information on 2D HOIP samples measured in this study

#	Chirality	Composition	Film thickness (nm)	Interlayer distance (Å)
1	Achiral	$[BA]_2PbI_4$	147 ± 11.9	13.3
2	Achiral	$[C_3A][PEA]PbI_4$	138 ± 6.0	13.9
3	Achiral	$[BA][PEA]PbI_4$	165 ± 3.8	14.9
4	Achiral	$[C_6A]_2PbI_4$	148 ± 6.0	16.35
5	Achiral	$[PEA]_2PbI_4$	153 ± 1.5	16.5
6	Achiral	$[AZO]_2PbI_4$	288 ± 11.4	23.5
7	Half chiral	$[S\text{-}C_3A]PbI_4$	133 ± 2.0	15.1
8	Half chiral	$[S\text{-}BA]PbI_4$	145 ± 4.0	16.8
9	Half chiral	$[S\text{-}PEA]PbI_4$	161 ± 5.6	16.95
10	Half chiral	$[S\text{-}C_6A]PbI_4$	146 ± 1.0	17.2
11	Half chiral	$[S\text{-}C_8A]PbI_4$	151 ± 3.0	17.6
12	Full chiral	$[SMBA]_2PbI_4$	148 ± 2.0	14.4
13	Full chiral	$[SMePEA]_2PbI_4$	158 ± 2.0	17.4

4.3 Thermal conductivity of 2D HOIP thin films

We measured the thermal conductivity of several thin films using TDTR.[87,184,186] Thermal conductivity is obtained by fitting the experimentally obtained temperature rise data with a multi-layered heat conduction model, with the thermal conductivity of 2D HOIP film as the only fitting parameter. Theoretically, the fitting is influenced by several parameters. As we described in Methods, the only unknown fitting parameter here is the heat capacity (c) of the 2D HOIP films.

We define a sensitivity index, as in our previous work to quantify the sensitivity of the fitting parameters.[87,184] Figure 4.4(a) shows the sensitivity of the thermal conductivity and heat capacity of the 2D HOIP films at 1.04 MHz modulation frequency. For the given thickness range of films studied in this work (~ 130 nm – 170 nm), the influence of heat capacity is negligible in contrast to thermal conductivity. It implies that the uncertainty due to heat capacity doesn't have a significant impact on the fitted thermal conductivity. Figure 4.4(b) shows a typical fitting of the TDTR parameter (ratio) for the 2D HOIP thin films. Excellent agreement between the experimental data and model is observed for the films used in this study.

Figure 4.5 shows the fitted thermal conductivity value for the achiral (Figure 4.5(a)), half-chiral and full-chiral (Figure 4.5(b)) 2D HOIP thin films. The thermal conductivity values are averaged over multiple different measurements. The standard deviation across several measurements contributes to random error. The systematic uncertainty is calculated by considering the error propagation based on the sensitivity of other fitting parameters such as thickness of metals (Al and Cu), thickness of 2D HOIP film, thermal conductivity of metals (Al and Cu) and substrate (Si), Interfacial thermal conductance's, heat capacity of metals, substrate and film, and spot size. The total uncertainty is calculated by adding random and systematic uncertainties. The thermal conductivity is plotted as a function of interlayer distance. The interlayer distance is calculated from the structures of the films (from the CIF file). Figure 4.5(a) shows the thermal conductivity of achiral 2D HOIP films. As all the films are different, the comparison between the observed thermal conductivity values is done on a case-by-case basis. Firstly, comparing the achiral alkyl-alkyl type 2D HOIPs, we see that the thermal conductivity of $[BA]_2$ is nearly twice that of $[C_6A]_2$.

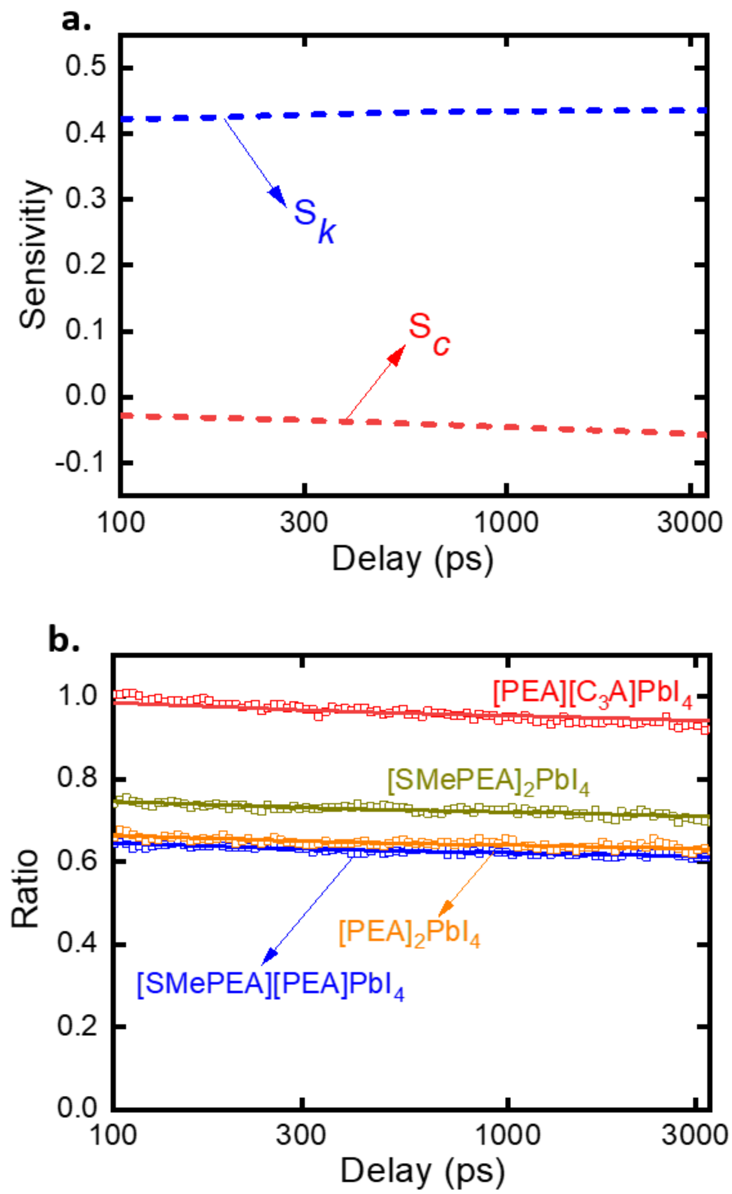

Figure 4.4 (a) Sensitivity of thermal conductivity (S_k) and heat capacity (S_c) for a 2D HOIP thin film at 1.04 MHz modulation frequency. The thermal conductivity and thickness of thin film is assumed to be 0.1 W $m^{-1}K^{-1}$ and 150 nm, respectively. The heat capacity for the film is assumed to be 1.4 J kg^{-1} cc^{-1}, which is a typical value for heat capacity of 2D HOIP thin films in literature (b) The TDTR parameter ratio fitting for the 2D HOIP thin films in this study. The solid lines show the heat conduction model, and the symbols indicate the experimental data. The fit for all the films is good within the experimental delay.

In general, thermal conductivity in HOIPs is influenced by the phonon group velocity and scattering, particularly at organic-organic interface. Previous investigation on 2D HOIP single crystals claimed to have no dependence on the interlayer distance for alkyl-alkyl organic cations, contrary to our observations. The results for elastic modulus (~ group velocity) show around 57% increase from C4 to C6. This is due to the replacement of softer organic layers with increasing alkyl chain length. Further, we'd like to argue that the results reported by [BA]2 are much lower than our measurements and in other studies. This discrepancy can be potentially due to structural rearrangement in their study due to high temperature rise (~30 K) and differences in preparation procedure. Also, Rasael et al. reported thermal conductivity of single crystals and we measured thin films, so the orientation can also play role in thermal conductivity behavior. The strong interlayer distance dependence for alkyl chains can be further attributed to scattering mechanisms. Increasing chain length also promotes film orientation parallel to the substrate, thus leading to lowering of thermal conductivity. Further, lower alkyl chain length have stronger inter-organic colombic interaction which helps stabilizing the structure, thereby leading to higher thermal conductivity compared to higher chain lengths.

Figure 4.5(a) further shows that the thermal conductivity of [PEA]2 is similar to [C6A]2. Both the organic ligands exhibit similar interlayer distance. Pure aromatic organic ligands possess sp2 (π - π) interaction in addition to the weak van der waal interaction in pure alkyl ligands. This is further supported by the fact that pure aromatic 2D HOIP films are stiffer than pure alkyl ones, leading to a higher phonon group velocity. Thus, it is expected that [PEA]2 shows higher thermal conductivity, which is not the case here. The observed low thermal conductivity in [PEA]2 highlights the strong dynamic disorder of the (π-π) stacked benzene rings.

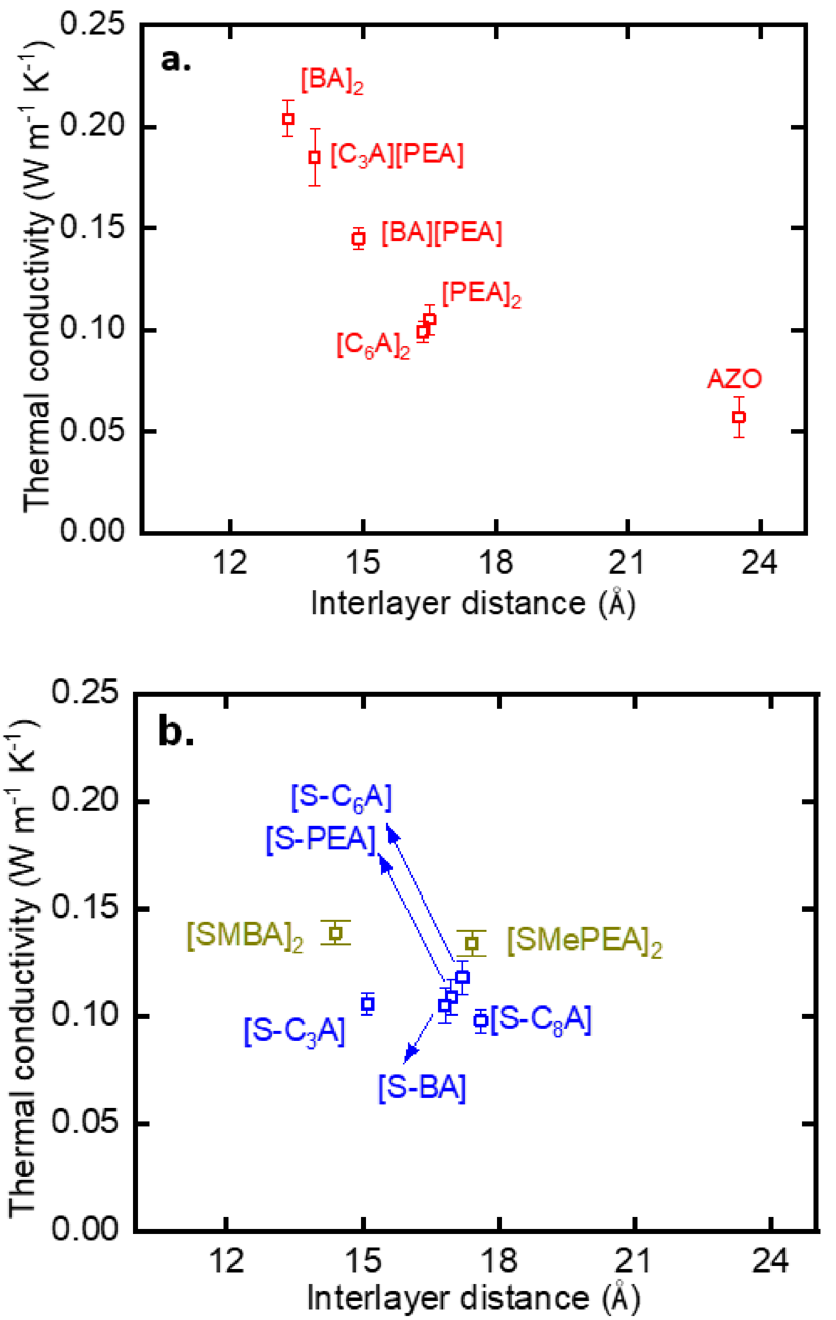

Figure 4.5. Thermal conductivity as a function of interlayer distance for (a) Achiral 2D HOIP thin films and (b) Chiral 2D HOIP thin films. The blue color represents half-chiral films and indigo color represents full chiral films. The data is presented in the form of mean ± standard deviation. The total standard deviation is the sum of random and systematic uncertainty in the measurements.

Further, replacing [PEA] with alkyl ligands increases thermal conductivity, which is expected considering that the disorder (π- π) stacking is replaced with relatively stable sp3 (CH-- π) interaction in mixed 2D HOIP films.

Figure 4.5(b) shows the fitted thermal conductivity of half-chiral and full-chiral 2D HOIP thin films. All the half-chiral 2D HOIPs have the same chiral ligand (SMePEA). Interestingly, the thermal conductivity for all the mixed chiral HOIPs is similar, regardless of the achiral organic ligand. This behavior can be explained by looking at the unique structure of mixed chiral HOIPs. Figure 2(c) shows the structure of S-C3A and S-C6A. A closer look at the interface between the aryl and alkyl groups shows that increasing the carbon chain length of alkyl ligand results in an increased C-C separation between the two layers. In general, the increase in separation between the organic layer should result in reduction in thermal conductivity. However, this is not the case for the mixed chiral thin films. On the other hand, we also observe that the S-C6A shows reduced H-H separation, thus increasing propensity for hydrogen bonding leading to enhancement in thermal conductivity. Thus, in half-chiral 2D HOIPs, the reduction in thermal conductivity due to larger C-C separation is offset by the enhancement because of stronger H-H interactions. Further, the thermal conductivity of half-chiral 2D HOIPs is slightly higher than lowest thermal conductivity observed in achiral 2D HOIPs (PEA_2) which highlights the better thermal transport across alkyl-aryl interfaces.

4.4 Elastic modulus of 2D HOIP thin films

In general, the elastic modulus in 2D HOIPs can be modulated by varying the length of organic layer, the interaction between the two organic layers and the inorganic framework.

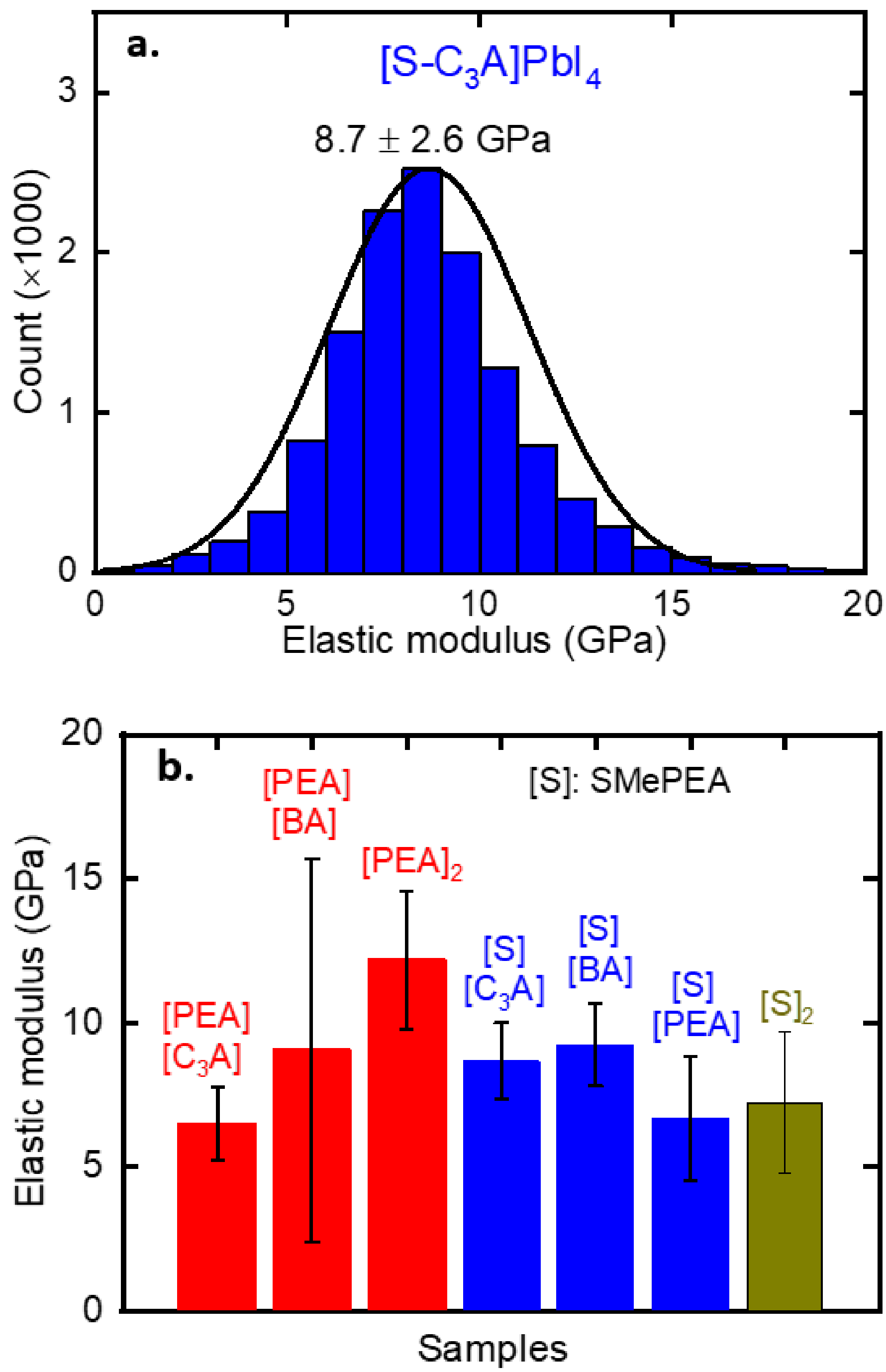

Figure 4.6 The elastic modulus of 2D HOIP thin films (a) Typical fitting of elastic modulus measured using nanoindentation for [SMePEA][C_3A]PbI_4 (b) Elastic modulus of 2D HOIP thin films

As the inorganic layer is the same in all the 2D HOIP films used in the study, the influence of the inorganic layer on elastic modulus will also be same. Figure 4.6 shows the measurement of elastic modulus of seven 2D HOIP thin films. Nanoindentation measurement of achiral 2D HOIPs show highest elastic modulus for PEA_2 thin film. This is in agreement with previous measurements and is attributed to the rigidity of the benzene rings. Replacing the PEA with softer alkyl chains leads to a reduction in average value, but still within the experimental uncertainty. In the case of half chiral films, the elastic modulus is similar between 7~9 GPa for all the films within the experimental uncertainty. This highlights that the interaction between the chiral and achiral organic cations are similar regardless of the choice of organic cations. Finally, the elastic modulus of the full chiral 2D HOIP film is also like half-chiral, lower than PEA_2. Comparing the structure of the two suggests that the orientation of benzene ring influences the elastic modulus. The thermal conductivity measurement shows higher values for full-chiral compared to PEA_2. This implies strong scattering of phonons due to (π-π) stacking in PEA_2.

4.5 Conclusion

We prepared 12 different 2D HOIP thin films with different organic cations comprising pure achiral, mixed achiral, mixed chiral and pure chiral. Combining structural data, GIWAXs and thermal conductivity characterization, this work offers insights into the thermal property-structure relation for several 2D HOIP thin films. Thermal conductivity of achiral 2D HOIP (both pure and mixed) can be modulated by changing the organic layer and the thermal conductance across the two organic layers. Introducing chirality into the 2D HOIP structure engenders unique structural changes which stabilizes the thermal conductivity regardless of the choice of achiral organic layer. This highlights the dominance of thermal conductance across the two organic layers in determining thermal transport in chiral 2D HOIPs. This work offers insight on modulating thermal conductivity in 2D HOIPs, key in implementing these materials at a device level.

CHAPTER 5

Molecularly engineered ultralow thermally conductivity in hybrid organic-inorganic perovskite

The last chapter highlighted the importance of organic-organic interface in determining the heat transport through 2D HOIP. Here, by engineering the organic-organic interface and orientation of the thin film, we demonstrate ultralow thermal conductivity in Azobenzene ethylammonium lead iodide (AZO). Thermal conductivity of nine AZO thin films, prepared under three different conditions and three different thicknesses are measured using TDTR. GIWAXS measurement reveal changes in isotropy and orientation under different conditions. The crystallinity of all the films is similar as also shown by GIWAXS. Measurement of elastic modulus suggest a similar modulus for the films in the range of 7 – 11 GPa, higher than existing ultralow thermal conductivity thin films. This suggests a high group velocity despite the ultralow-k. Molecular dynamic simulations reveal a significant role of dynamic disorder in determining ultralow-k. The record low thermal conductivity, low anisotropy ratio, high mechanical stiffness and degree of modulation shows the multifunctionality of the AZO films.

5.1 GIWAXS measurement of 2D HOIP thin film

Grazing index wide angle scattering (GIWAXS) is used to discern the orientation and crystallite size in the 2D HOIP thin films. An X-ray beam is directed at an angle close to the total external reflection from the film. The detector measured the scattered intensity which gives information on the orientation and crystallite size.

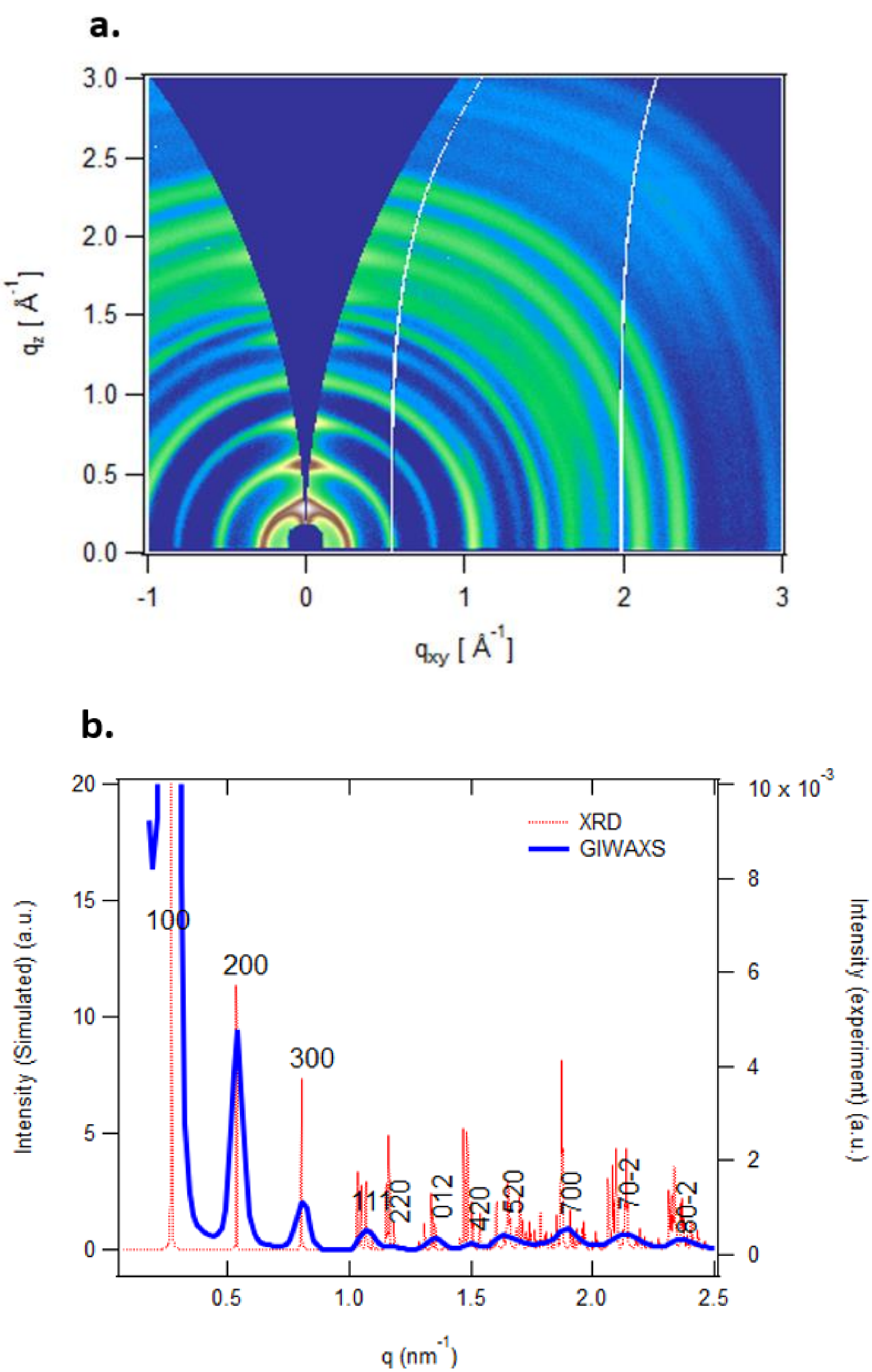

Figure 5.1 (a) Typical GIWAXS pattern of AZO thin film (b) Comparison of simulated XRD with peak intensity from GIWAXS (line cut)

The order parameter indicates the orientation of the 2D HOIP thin films. An order parameter close to 0 indicates isotropic film (high thermal conductivity), compared to an order parameter of 1 which indicates a parallel film orientation (low thermal conductivity).

Coherence length indicates the crystallite size. The MFP for such films is expected to be less than 10 nm (less than BTO in chapter 3). As the crystallite size for all the films is around 20 nm with a divergence of 5 nm, this is not going to effect thermal conductivity a lot.

5.2 Thermal conductivity measurement of AZO 2D HOIP films

Thermal conductivity of all the films is measured using TDTR. An additional Cu layer is deposited prior to Al deposition to protect the AZO film. Thermal conductivity of 9 different films with different thickness (100 nm, 150 nm and 250 nm nominal thickness) and different baking temperatures (60 C, 80 C and 100 C) have been measured.

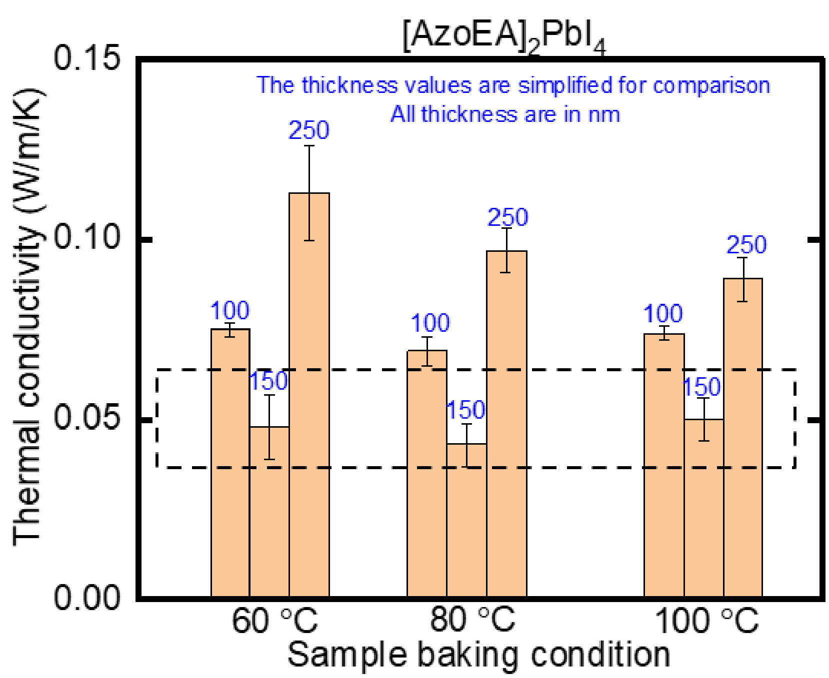

Figure 5.2 Thermal conductivity of the AZO 2D HOIP thin films with different thickness and baking conditions. The 150 nm thick films show the lowest thermal conductivity potentially due to high isotropy and low group velocity

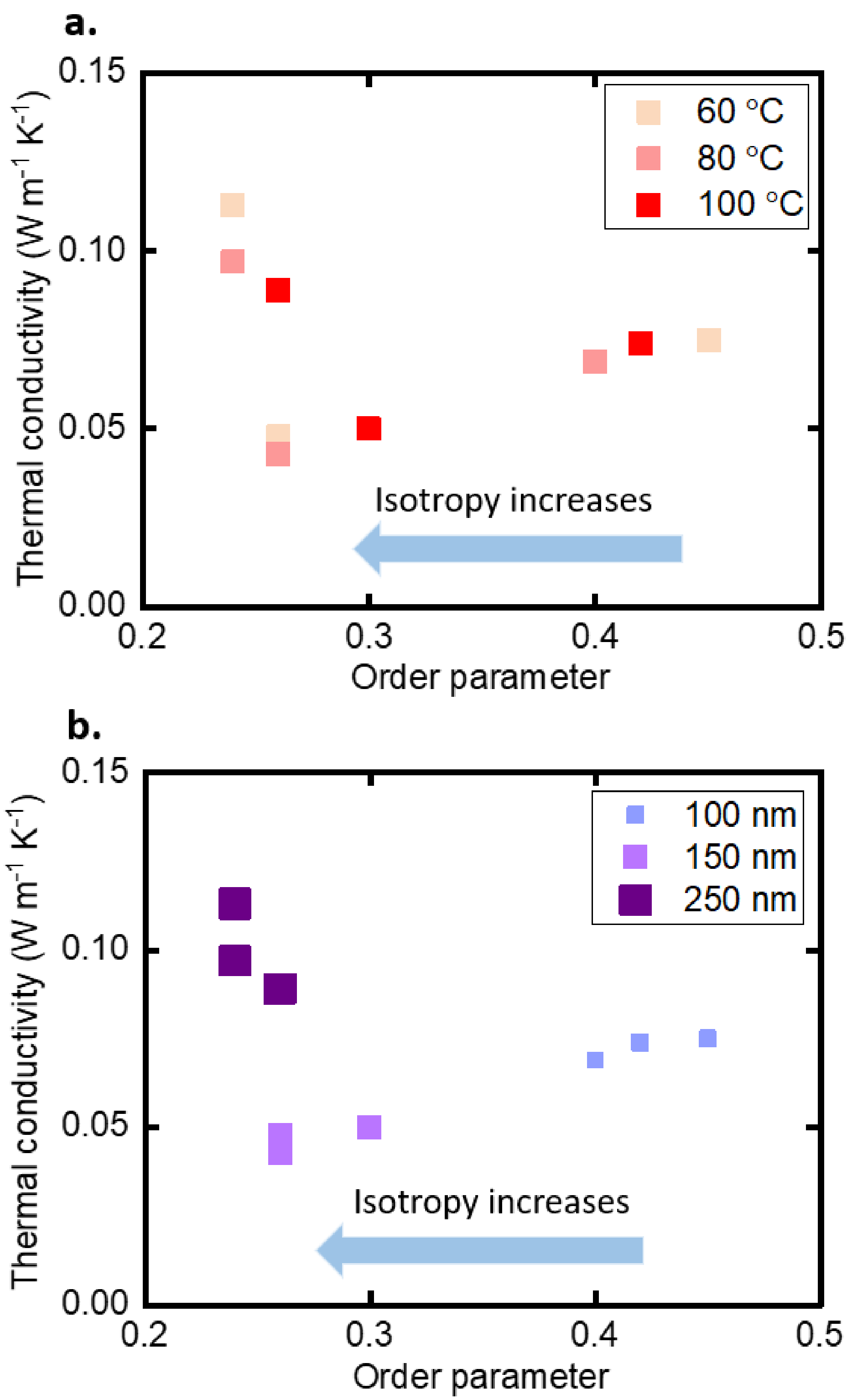

Figure 5.3 Correlation plots of thermal conductivity and order parameter (a) classification based on annealing temperature and (b) classification based on film thickness

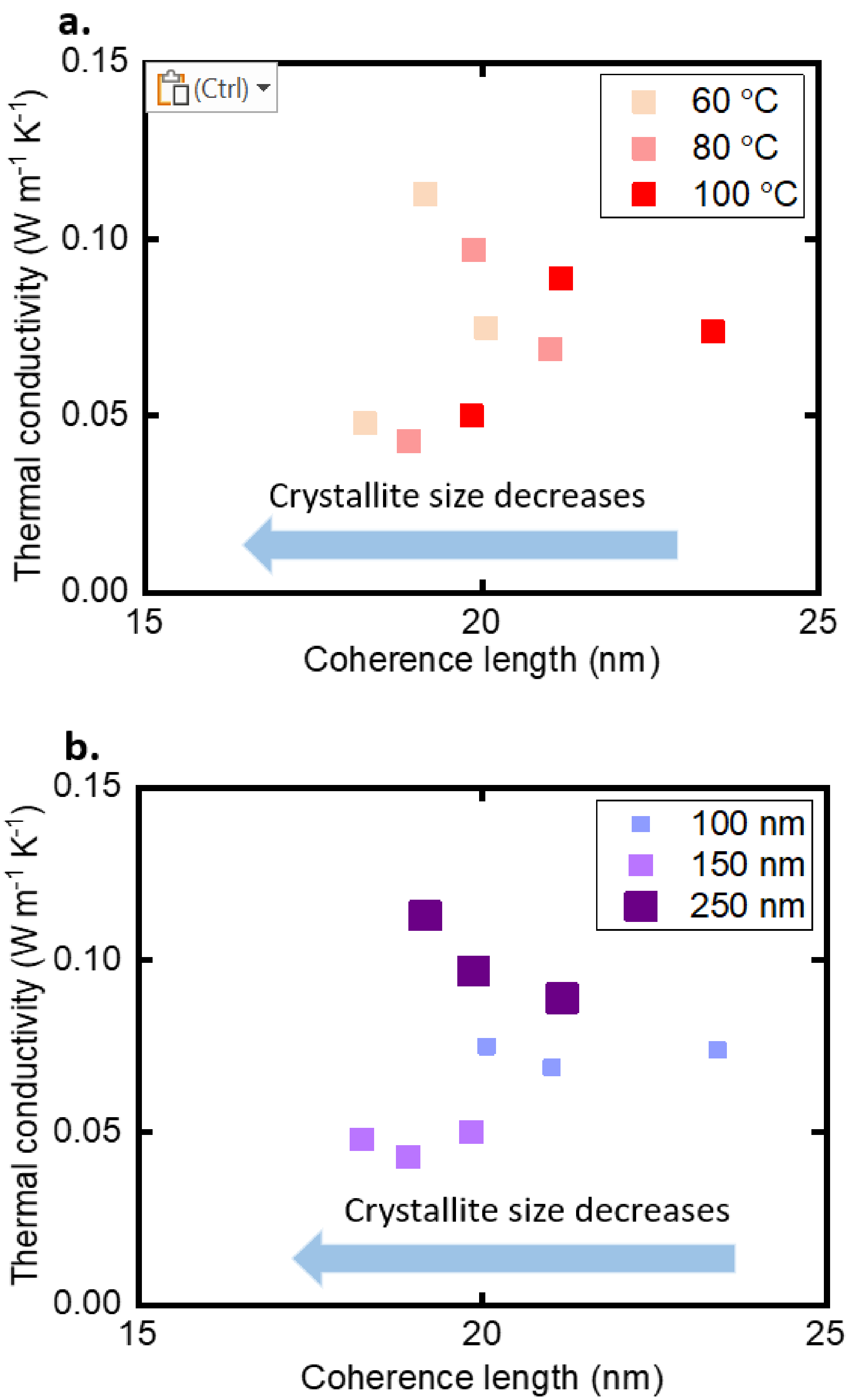

Figure 5.4 Correlation plots of thermal conductivity and coherence length (a) classification based on annealing temperature and (b) classification based on film thickness

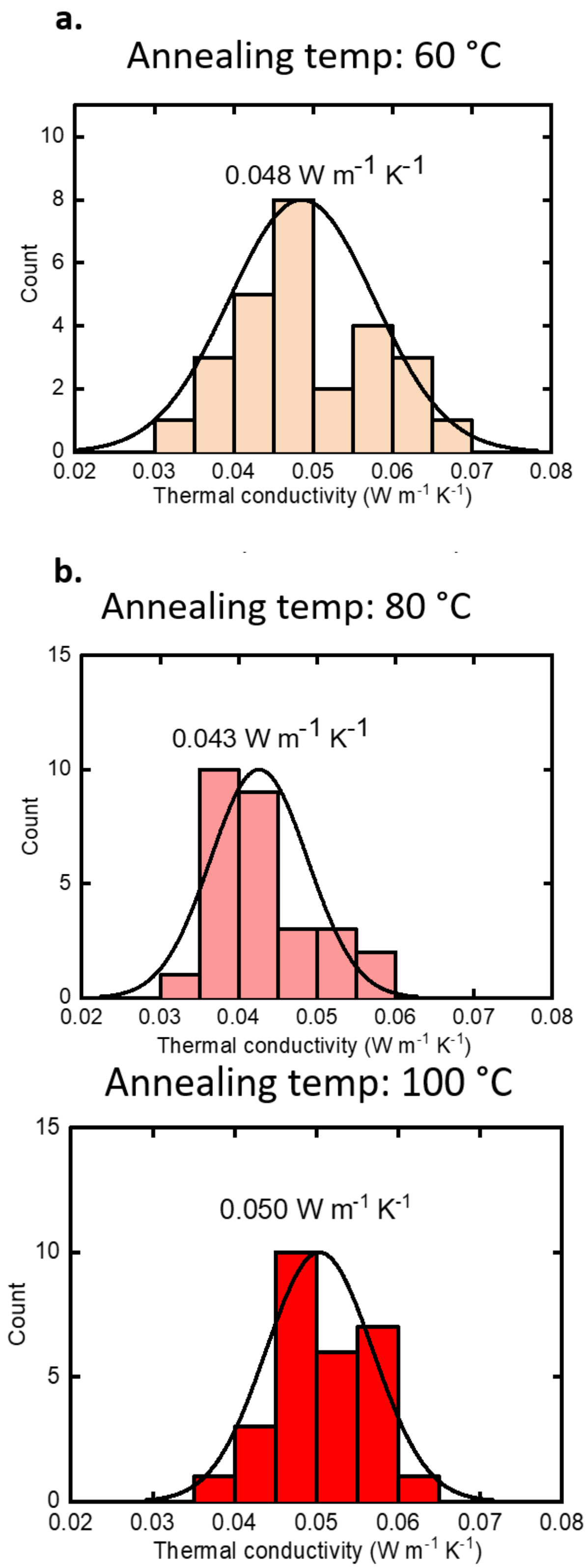

Figure 5.5 Thermal conductivity measurement of 2D HOIP thin films of nominal thickness = 150 nm annealed at (a) 60 C (b) 80 C and (c) 100 C

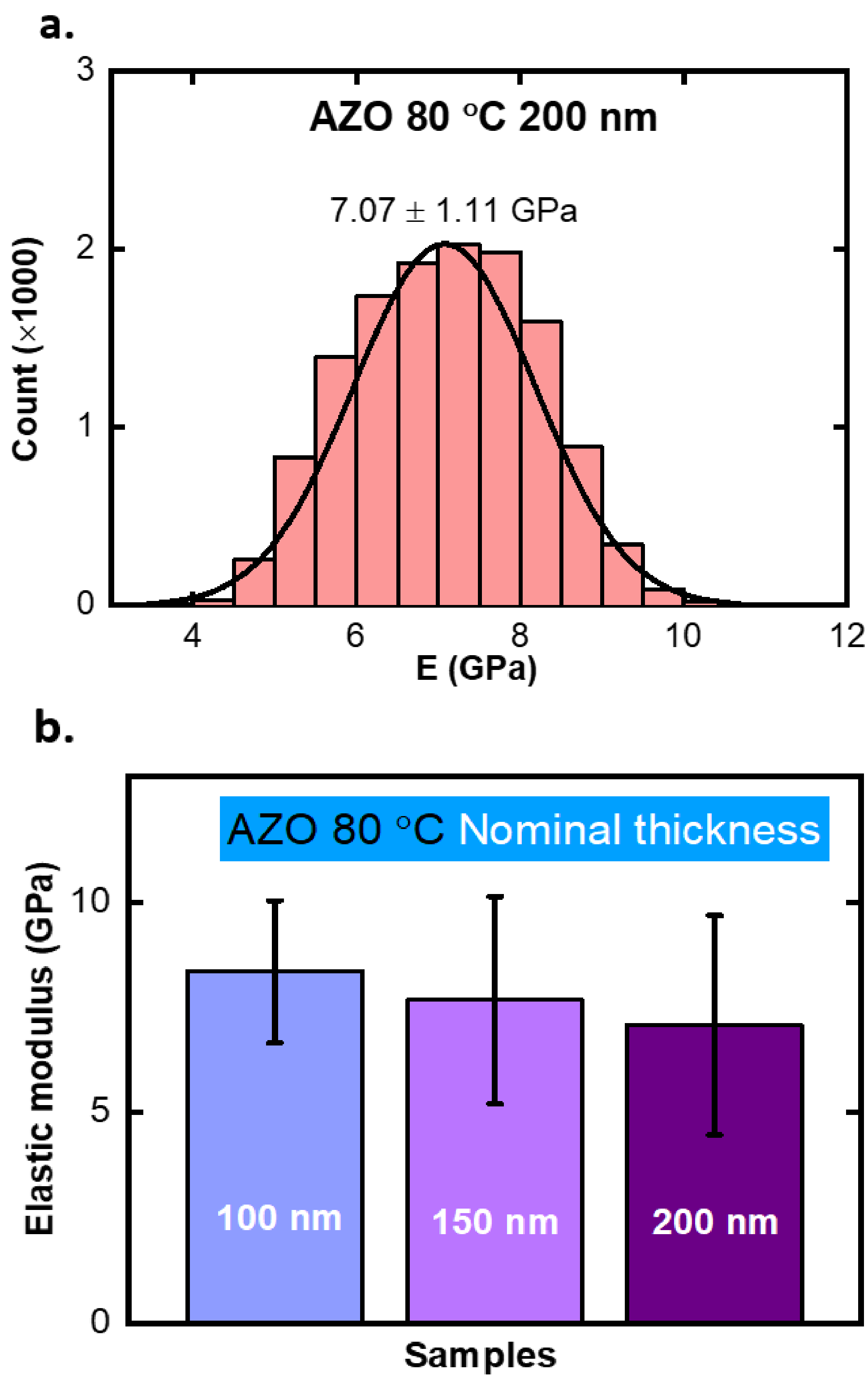

Figure 5.6 (a) Typical elastic modulus fitting for AZO film using nanoindentation (b) Elastic modulus of AZO films annealed at 80 C.

Correlation analysis of AZO indicates a weak temperature dependence. Further, the correlation analysis indicates thicker films are more isotropic, partially explaining the lower thermal conductivity of 150 nm films. The higher thermal conductivity of 250 nm films is most likely due to higher group velocity (~ Elastic modulus). Those measurements are still underway during the preparation of this manuscript and have not been included here.

5.3 Elastic modulus of 2D AZO thin films

The elastic modulus of AZO thin films of 100, 150 nm and 250 nm thickness and baked at 80C is measured. The elastic modulus is similar for all the films within the experimental uncertainty. This indicates that the group velocity is not responsible for such a low thermal conductivity in the material. This also supports the role of "phonon filtering" in obtaining such ultralow-k in this material.

5.4 Conclusion

The AZO 2D HOIP has the **lowest** thermal conductivity ever recorded for a 2D HOIP material. Furthermore, the thermal conductivity is comparable to the record of lowest thermal conductivity (0.038 ~ 0.05 W/m/K) for a fully dense solid. The high elastic stiffness of this material, coupled with ultralow thermal conductivity makes it highly appealing thermal insulation material. Further, this material is also excellent choice for thermoelectrics given the low k and facile preparation (typically spin casting).

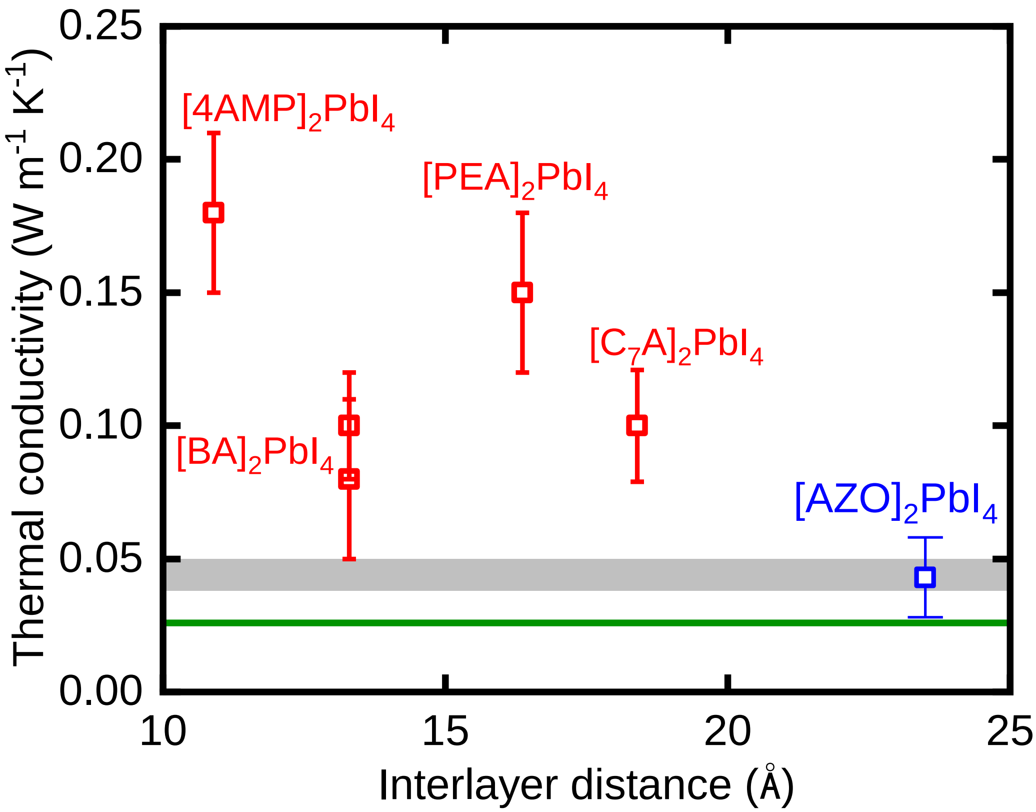

Figure 5.7 Comparison of thermal conductivity measurements of 2D HOIP thin films. The grey area represents the lowest thermal conductivity of fully dense solids. The green line indicates the thermal conductivity of air.

CHAPTER 6

Conclusion and Future work

This thesis highlights and develops methods to engineer thermal transport in ferroelectric single crystals, thin films and hybrid organic-inorganic thin films.[208, 209] The selection of these materials is driven by their ubiquity in industrial and recent research in several fields of engineering and physics. This study also highlights the potential use of these materials to mitigate thermal management challenges.

In chapter 2, thermal conductivity modulation has been demonstrated in PMN-PT single crystals, which are already commercialized and widely used in ultrasound and piezoelectric applications. This study presents an additional functionality as thermal modulation, which further broadens the applicability of the material in different fields. From a scientific perspective, this study also uncovered some of the fundamental questions on domain wall engineering of ferroelectrics which is key for understanding their structure-property relationship. I believe that the methodology developed in this study can also be extended to other materials such as PIN-PMN-PT, which are nowadays preferred owing to low curie temperature.

Chapter 3 presents the understanding of phonon mean free path distribution in BTO. Surprisingly, even after decades of research on thermal properties, the accurate MFP prediction is not present for a lot of oxide perovskite materials like BTO. Information of MFP distribution aids in nano structuring in thermoelectric materials and avoids incorrect assumptions about thermal conductivity scaling. Further, MFP distribution can also be used to explore extreme thermal transport regimes such as super-diffusive and quasi-ballistic phonon transport. Thermal conductivity modulation can be achieved in BTO thin films by manipulating domain walls, which can be undertaken in a future study

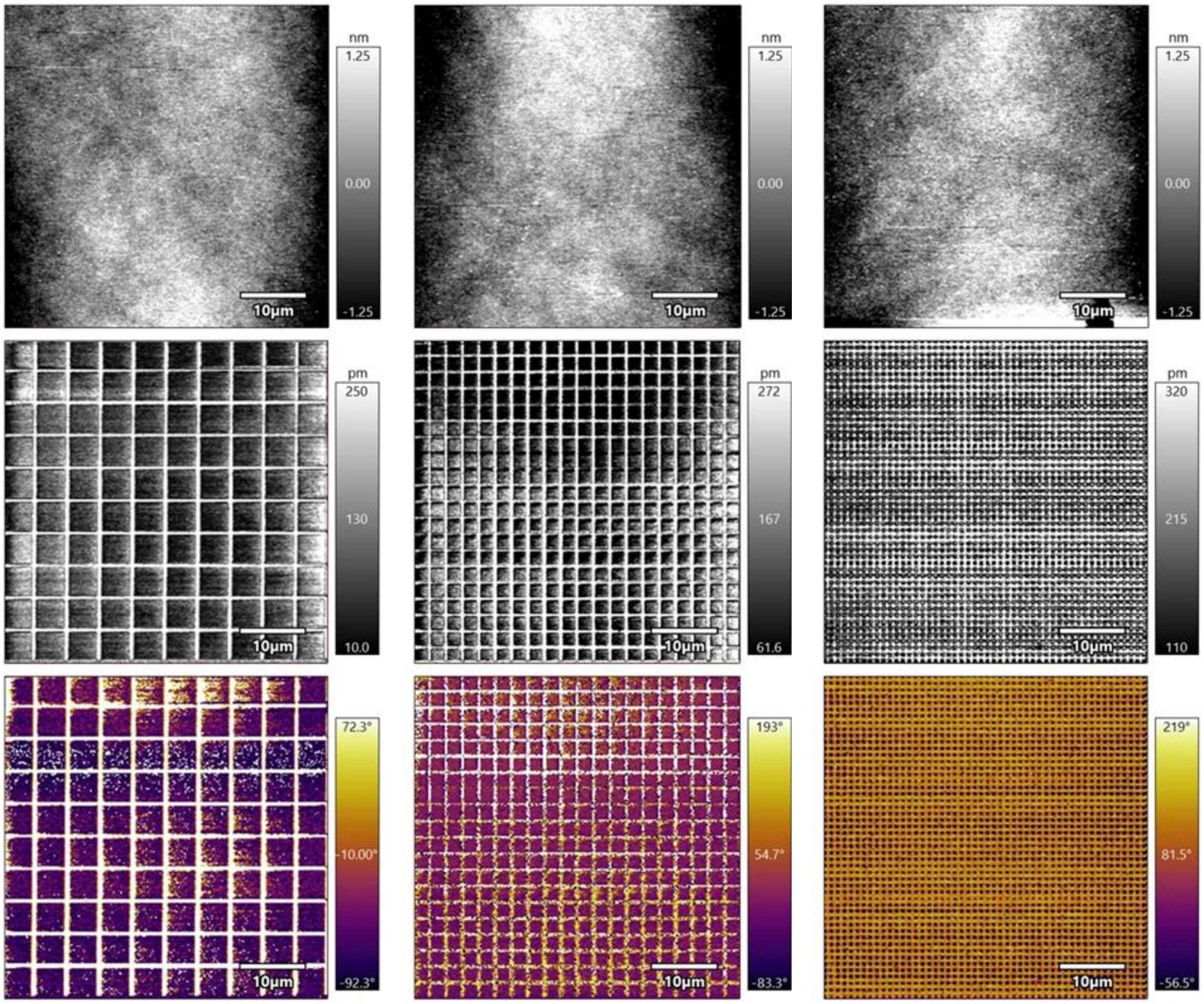

(a) (b) (c)

Figure 6.1 Manipulating domain walls in BTO thin film using piezoresponse force microscopy. The images show the morphology (top), amplitude (middle) and phase (bottom) of the BTO films. The domain walls are created in 16 nm BTO film on top STO substrate with the average domain size of (a) 1 um, (b) 0.5 um and (c) 0.2 um

Chapter 4 introduces a unique class of materials known as Hybrid organic inorganic perovskite (HOIP). These materials have already surpassed the photovoltaic efficiency of currently commercialized solar cell materials. Further, they are excellent candidates for thermoelectric, optical and electronic applications. Implementation of these materials on a device level requires a thorough understanding of their thermal conductivity. This study identifies the parameters that affect the thermal conductivity in 2D HOIP thin films. We prepared and measured different films that led to different thermal conductivity modulation. The organic-organic interface plays a dominant role in determining thermal conductivity in these materials.

Chapter 5 deals with molecular engineering of a specific 2D HOIP thin film which shows ultralow thermal conductivity. Nine different films with different thickness and annealing conditions are prepared and measured. Record low thermal conductivity is confirmed using TDTR and molecular dynamics assisted lattice dynamic simulations. The weak bonding in the organic interface, benzene pi-pi stacking and dynamic disorder leads to such ultralow thermal conductivity. The high mechanical stiffness, ultralow thermal conductivity, potential for thermal conductivity modulation, facile preparation and multifunctionality makes this an ideal material for several applications.

REFERENCES

1. Qian, X., Zhou, J. & Chen, G. Phonon-engineered extreme thermal conductivity materials. *Nat. Mater.* **20**, 1188–1202 (2021).
2. *High Thermal Conductivity Materials*. (Springer-Verlag, 2006).
3. Ball, P. Feeling the heat: the more that microcircuits are shrunk, the hotter they get. Engineers are on the hunt for ways to cool off computing. *Nature* **492**, 174–177 (2012).
4. Waldrop, M. M. The chips are down for Moore's law. *Nat. News* **530**, 144 (2016).
5. Garimella, S. V., Yeh, L.-T. & Persoons, T. Thermal Management Challenges in Telecommunication Systems and Data Centers. *IEEE Trans. Compon. Packag. Manuf. Technol.* **2**, 1307–1316 (2012).
6. Clarke, D. R. Materials selection guidelines for low thermal conductivity thermal barrier coatings. *Surf. Coat. Technol.* **163–164**, 67–74 (2003).
7. Anharmoncity and low thermal conductivity in thermoelectrics - ScienceDirect.
8. Eivari, H. A., Sohbatzadeh, Z., Mele, P. & Assadi, M. H. N. Low thermal conductivity: fundamentals and theoretical aspects in thermoelectric applications. *Mater. Today Energy* **21**, 100744 (2021).
9. Yuan, K. *et al.* Engineering the Thermal Conductivity of Functional Phase-Change Materials for Heat Energy Conversion, Storage, and Utilization. *Adv. Funct. Mater.* **30**, 1904228 (2020).
10. Zhao, M. *et al.* Defect engineering in development of low thermal conductivity materials: A review. *J. Eur. Ceram. Soc.* **37**, 1–13 (2017).

11. Kim, H. S., Wang, T., Liu, W. & Ren, Z. Engineering thermal conductivity for balancing between reliability and performance of bulk thermoelectric generators. *Adv. Funct. Mater.* **26**, 3678–3686 (2016).

12. Guo, Y., Zhou, Y. & Xu, Y. Engineering polymers with metal-like thermal conductivity—Present status and future perspectives. *Polymer* **233**, 124168 (2021).

13. Laaber, D. & Bart, H.-J. Chemical Resistance and Mechanical Stability of Polymer Film Heat Exchangers. *Chem. Ing. Tech.* **87**, 306–311 (2015).

14. Feng, S., Kamat, A. M. & Pei, Y. Design and fabrication of conformal cooling channels in molds: Review and progress updates. *Int. J. Heat Mass Transf.* **171**, 121082 (2021).

15. Amaral, S., Verstraete, T., Van den Braembussche, R. & Arts, T. Design and Optimization of the Internal Cooling Channels of a High Pressure Turbine Blade—Part I: Methodology. *J. Turbomach.* **132**, (2010).

16. Zhang, Z., Wang, X. & Yan, Y. A review of the state-of-the-art in electronic cooling. *E-Prime - Adv. Electr. Eng. Electron. Energy* **1**, 100009 (2021).

17. Sohel Murshed, S. M. & Nieto de Castro, C. A. A critical review of traditional and emerging techniques and fluids for electronics cooling. *Renew. Sustain. Energy Rev.* **78**, 821–833 (2017).

18. Zhang, X. *et al.* Personal thermal management by thermally conductive composites: A review. *Compos. Commun.* **23**, 100595 (2021).

19. Maqbool, M. *et al.* Engineering of polymer-based materials for thermal management solutions. *Compos. Commun.* **29**, 101048 (2022).

20. Smalyukh, I. I. Thermal Management by Engineering the Alignment of Nanocellulose. *Adv. Mater.* **33**, 2001228 (2021).

21. Ruan, K. *et al.* Significant Reduction of Interfacial Thermal Resistance and Phonon Scattering in Graphene/Polyimide Thermally Conductive Composite Films for Thermal Management. *Research* **2021**, 2021/8438614 (2021).
22. Sledzinska, M. *et al.* 2D Phononic Crystals: Progress and Prospects in Hypersound and Thermal Transport Engineering. *Adv. Funct. Mater.* **30**, 1904434 (2020).
23. Nomura, M. *et al.* Review of thermal transport in phononic crystals. *Mater. Today Phys.* **22**, 100613 (2022).
24. Sharma, P., Moise, T. S., Colombo, L. & Seidel, J. Roadmap for Ferroelectric Domain Wall Nanoelectronics. *Adv. Funct. Mater.* **32**, 1–16 (2022).
25. Parkin, S. S. P., Hayashi, M. & Thomas, L. Magnetic domain-wall racetrack memory. *Science* **320**, 190–194 (2008).
26. Catalan, G., Seidel, J., Ramesh, R. & Scott, J. F. Domain wall nanoelectronics. *Rev. Mod. Phys.* **84**, 119–156 (2012).
27. Kim, H. P. *et al.* A Review on Alternating Current Poling for Perovskite Relaxor-$PbTiO_3$ Single Crystals. *IEEE Trans. Ultrason. Ferroelectr. Freq. Control* 1–12 (2022) doi:10.1109/TUFFC.2022.3181236.
28. Zhang, S. & Li, F. High performance ferroelectric relaxor-PbTiO 3 single crystals: Status and perspective. *J. Appl. Phys.* **111**, 031301 (2012).
29. Sun, E. & Cao, W. Relaxor-based ferroelectric single crystals: Growth, domain engineering, characterization and applications. *Prog. Mater. Sci.* **65**, 124–210 (2014).
30. Zhang, S. *et al.* Advantages and Challenges of Relaxor-PbTiO3 Ferroelectric Crystals for Electroacoustic Transducers- A Review. *Prog Mater Sci* **68**, 1–66 (2015).

31. Zhang, S. *et al.* Recent developments in piezoelectric crystals. *J. Korean Ceram. Soc.* **55**, 419–439 (2018).

32. Yamashita, Y. *et al.* A Review of Lead Perovskite Piezoelectric Single Crystals and Their Medical Transducers Application. *IEEE Trans. Ultrason. Ferroelectr. Freq. Control* **69**, 3048–3056 (2022).

33. Sun, Y., Karaki, T., Fujii, T. & Yamashita, Y. Alternate current poling and direct current poling for Pb(Mg1/3Nb2/3)O3-PbTiO3 single crystals. *Jpn. J. Appl. Phys.* **58**, SLLC06 (2019).

34. Chang, W. *et al.* Dielectric and piezoelectric properties of 0 . 7 using alternating current. **3831**, (2018).

35. Qiu, C., Liu, J., Li, F. & Xu, Z. Thickness dependence of dielectric and piezoelectric properties for alternating current electric-field-poled relaxor-PbTiO 3 crystals. *J. Appl. Phys.* **125**, 0–7 (2019).

36. Zhang, Z. *et al.* The performance enhancement and temperature dependence of piezoelectric properties for Pb(Mg 1/3 Nb 2/3)O 3 -0.30PbTiO 3 single crystal by alternating current polarization. *J. Appl. Phys.* **125**, 0–7 (2019).

37. Liu, J. *et al.* Impact of alternating current electric field poling on piezoelectric and dielectric properties of Pb(In1/2Nb1/2)O3-Pb(Mg1/3Nb2/3)O3-PbTiO3ferroelectric crystals. *J. Appl. Phys.* **128**, 094104 (2020).

38. Wan, H., Luo, C., Chung, C. C., Yamashita, Y. & Jiang, X. Enhanced dielectric and piezoelectric properties of manganese-doped Pb(In1/2Nb1/2)O3-Pb(Mg1/3Nb2/3)O3-PbTiO3single crystals by alternating current poling. *Appl. Phys. Lett.* **118**, 0–6 (2021).

39. Xu, J. *et al.* Piezoelectric performance enhancement of Pb(Mg1/3Nb2/3)O3-0.25PbTiO3 crystals by alternating current polarization for ultrasonic transducer. *Appl. Phys. Lett.* **112**, 0–5 (2018).

40. Wada, S., Yako, K., Yokoo, K., Kakemoto, H. & Tsurumi, T. Domain Wall Engineering in Barium Titanate Single Crystals for Enhanced Piezoelectric Properties Domain Wall Engineering in Barium Titanate Single Crystals for Enhanced Piezoelectric Properties. **0193**, (2011).

41. Ahluwalia, R., Lookman, T., Saxena, A. & Cao, W. Domain-size dependence of piezoelectric properties of ferroelectrics. *Phys. Rev. B - Condens. Matter Mater. Phys.* **72**, 1–13 (2005).

42. Porta, M. *et al.* The piezoelectric response of nanotwinned. (2009) doi:10.1088/0957-4484/20/10/105709.

43. Wang, B., Li, F. & Chen, L. Q. Inverse Domain-Size Dependence of Piezoelectricity in Ferroelectric Crystals. *Adv. Mater.* **33**, 1–9 (2021).

44. Qiu, C. *et al.* Transparent ferroelectric crystals with ultrahigh piezoelectricity. *Nature* **577**, 350–354 (2020).

45. Wan, H. *et al.* Alternating current poling on sliver-mode rhombohedral Pb(Mg1/3Nb2/3)O3-PbTiO3 single crystals. *Acta Mater.* **208**, 116759 (2021).

46. Ushakov, A. D. *et al.* Domain structure evolution during alternating current poling and its influence on the piezoelectric properties in [001]-cut rhombohedral PIN-PMN-PT single crystals. *Appl. Phys. Lett.* **118**, 1–6 (2021).

47. Qiu, C. *et al.* In-situ domain structure characterization of Pb(Mg1/3Nb2/3)O3-PbTiO3 crystals under alternating current electric field poling. *Acta Mater.* **210**, 116853 (2021).

48. Xu, G., Gehring, P. M., Stock, C. & Conlon, K. The anomalous skin effect in single crystal relaxor ferroelectric PZN- x PT and PMN- x PT. *Phase Transit.* **79**, 135–152 (2006).

49. Xu, C. *et al.* Domain Structure Evolutions during the Poling Process for [011]-Oriented PMN-xPT Crystals Across the MPB Region. *J. Am. Ceram. Soc.* **99**, 2096–2102 (2016).

50. Hou, D. *et al.* Field-induced polarization rotation and phase transitions in 0.70Pb(M g1/3 N b2/3) O3-0.30PbTi O3 piezoceramics observed by in situ high-energy x-ray scattering. *Phys. Rev. B* **97**, 1–9 (2018).

51. Liu, H. *et al.* Role of Reversible Phase Transformation for Strong Piezoelectric Performance at the Morphotropic Phase Boundary. *Phys. Rev. Lett.* **120**, 55501 (2018).

52. Fan, L. *et al.* Unique Piezoelectric Properties of the Monoclinic Phase in Pb (Zr,Ti) O3 Ceramics: Large Lattice Strain and Negligible Domain Switching. *Phys. Rev. Lett.* **116**, 1–5 (2016).

53. Li, C. *et al.* Atomic-scale origin of ultrahigh piezoelectricity in samarium-doped PMN-PT ceramics. *Phys. Rev. B* **101**, 1–7 (2020).

54. Mante, A. J. H. & Volger, J. Phonon transport in barium titanate. *Physica* **52**, 577–604 (1971).

55. Weilert, M. A., Msall, M. E., Anderson, A. C. & Wolfe, J. P. Phonon scattering from ferroelectric domain walls: Phonon imaging in KDP. *Phys. Rev. Lett.* **71**, 735–738 (1993).

56. Weilert, M. A., Msall, M. E., Wolfe, J. P. & Anderson, A. C. Mode dependent scattering of phonons by domain walls in ferroelectric KDP. *Z. Für Phys. B* **91**, 179–188 (1993).

57. Langenberg, E. *et al.* Ferroelectric Domain Walls in PbTiO3 Are Effective Regulators of Heat Flow at Room Temperature. *Nano Lett.* **19**, 7901–7907 (2019).

58. Ihlefeld, J. F. *et al.* Room-temperature voltage tunable phonon thermal conductivity via reconfigurable interfaces in ferroelectric thin films. *Nano Lett.* **15**, 1791–1795 (2015).

59. Foley, B. M. *et al.* Voltage-Controlled Bistable Thermal Conductivity in Suspended Ferroelectric Thin-Film Membranes. *ACS Appl. Mater. Interfaces* **10**, 25493–25501 (2018).

60. Wang, J. J., Wang, Y., Ihlefeld, J. F., Hopkins, P. E. & Chen, L. Q. Tunable thermal conductivity via domain structure engineering in ferroelectric thin films: A phase-field simulation. *Acta Mater.* **111**, 220–231 (2016).

61. Seijas-Bellido, J. A. *et al.* A phononic switch based on ferroelectric domain walls. *Phys. Rev. B* **96**, 1–6 (2017).

62. Bugallo, D. *et al.* Deconvolution of Phonon Scattering by Ferroelectric Domain Walls and Point Defects in a PbTiO3Thin Film Deposited in a Composition-Spread Geometry. *ACS Appl. Mater. Interfaces* **13**, 45679–45685 (2021).

63. Qian, X., Zhou, J. & Chen, G. Phonon-engineered extreme thermal conductivity materials. *Nat. Mater.* **20**, 1188–1202 (2021).

64. Yang, F. & Dames, C. Mean free path spectra as a tool to understand thermal conductivity in bulk and nanostructures. *Phys. Rev. B - Condens. Matter Mater. Phys.* **87**, 1–12 (2013).

65. Wu, D. *et al.* Understanding Nanostructuring Processes in Thermoelectrics and Their Effects on Lattice Thermal Conductivity. *Adv. Mater.* **28**, 2737–2743 (2016).

66. Bell, L. E. Cooling, heating, generating power, and recovering waste heat with thermoelectric systems. *Science* **321**, 1457–1461 (2008).

67. Heremans, J. P., Dresselhaus, M. S., Bell, L. E. & Morelli, D. T. When thermoelectrics reached the nanoscale. *Nat. Nanotechnol.* **8**, 471–473 (2013).

68. Li, P. *et al.* Thermo-Optically Designed Scalable Photonic Films with High Thermal Conductivity for Subambient and Above-Ambient Radiative Cooling. *Adv. Funct. Mater.* **32**, 1–10 (2022).

69. Regner, K. T. *et al.* Broadband phonon mean free path contributions to thermal conductivity measured using frequency domain thermoreflectance. *Nat. Commun.* **4**, 1–7 (2013).

70. Fan, Z., Kuan, S. & Wang, J. Perovskites for photovoltaics: a combined review of organic-inorganic halide perovskites and ferroelectric oxide perovskites. *J. Mater. Chem. A* **3**, 18809–18828 (2015).

71. Nuraje, N. & Su, K. Perovskite ferroelectric nanomaterials. *Nanoscale* **5**, 8752–8780 (2013).

72. Li, W. & Ji, L. J. Perovskite ferroelectrics go metal free. *Science* **361**, 132 (2018).

73. Wu, H. W. *et al.* Direct Observation of Large Atomic Polar Displacements in Epitaxial Barium Titanate Thin Films. *Adv. Mater. Interfaces* **7**, 1–8 (2020).

74. Acosta, M. *et al.* BaTiO3-based piezoelectrics : Fundamentals , current status , and perspectives. *Appl. Phys. Rev.* **041305**, 041305 (2017).

75. Tao, J., Cao, S. A., Feng, R. & Deng, Y. High dielectric thin films based on barium titanate and cellulose nanofibrils. *RSC Adv.* **10**, 5758–5765 (2020).

76. Razi, P. M., Angappane, S. & Gangineni, R. B. Bipolar resistive switching studies in amorphous barium titanate thin films in Ag/am-BTO/ITO capacitor structures. *Mater. Sci. Eng. B Solid-State Mater. Adv. Technol.* **263**, 114852 (2021).

77. Zhu, X. *et al.* Significantly enhanced energy storage density of epitaxial Ba0.53Sr0.47TiO3 thin films by optimizing bottom electrode material. *Ceram. Int.* **46**, 13900–13906 (2020).

78. Karvounis, A., Timpu, F., Vogler-Neuling, V. V., Savo, R. & Grange, R. Barium Titanate Nanostructures and Thin Films for Photonics. *Adv. Opt. Mater.* **8**, 1–23 (2020).

79. Waser, R., Dittmann, R., Staikov, C. & Szot, K. Redox-based resistive switching memories nanoionic mechanisms, prospects, and challenges. *Adv. Mater.* **21**, 2632–2663 (2009).

80. Ahadi, K. *et al.* Enhancing superconductivity in SrTiO3 films with strain. *Sci. Adv.* **5**, 1–6 (2019).

81. Scholtz, Ľ. *et al.* Investigation of barium titanate thin films as simple antireflection coatings for solar cells. *Appl. Surf. Sci.* **461**, 249–254 (2018).

82. Sangle, A. L. *et al.* Very High Surface Area Mesoporous Thin Films of SrTiO3 Grown by Pulsed Laser Deposition and Application to Efficient Photoelectrochemical Water Splitting. *Nano Lett.* **16**, 7338–7345 (2016).

83. Gao, J., Xue, D., Liu, W., Zhou, C. & Ren, X. Recent progress on BaTiO3-based piezoelectric ceramics for actuator applications. *Actuators* **6**, (2017).

84. Ziati, M. & Ez-Zahraouy, H. Theoretical investigation of electronic, optical and thermoelectric properties of tellurium doped barium titanate (BTO) through modified Becke – Johnson exchange potential. *Optik* **231**, 166440 (2021).

85. Kheyrdan, A., Abdizadeh, H., Shakeri, A. & Golobostanfard, M. R. Structural, electrical, and optical properties of sol-gel-derived zirconium-doped barium titanate thin films on transparent conductive substrates. *J. Sol-Gel Sci. Technol.* **86**, 141–150 (2018).

86. Abdollahi, M., Firouzabadi, Y., Dehghani, F. & Mohammadi, S. THAMON: Thermal-aware High-performance Application Mapping onto Opto-electrical network-on-chip. *J. Syst. Archit.* **121**, (2021).

87. Wang, S. *et al.* Revisiting the Reduction of Thermal Conductivity in Nano- to Micro-Grained Bismuth Telluride: The Importance of Grain-Boundary Thermal Resistance. *Eng. Sci.* **17**, 45–55 (2022).

88. Xie, G., Ding, D. & Zhang, G. Phonon coherence and its effect on thermal conductivity of nanostructures. *Adv. Phys. X* **3**, 720–755 (2018).

89. Foley, B. M. *et al.* Thermal conductivity of nano-grained SrTiO3 thin films. *Appl. Phys. Lett.* **101**, (2012).

90. Sánchez, F., Ocal, C. & Fontcuberta, J. Tailored surfaces of perovskite oxide substrates for conducted growth of thin films. *Chem. Soc. Rev.* **43**, 2272–2285 (2014).

91. Tachibana, M., Kolodiazhnyi, T. & Takayama-muromachi, E. Thermal conductivity of perovskite ferroelectrics. **092902**, 91–94 (2016).

92. He, Y. Heat capacity, thermal conductivity, and thermal expansion of barium titanate-based ceramics. *Thermochim. Acta* **419**, 135–141 (2004).

93. Jezowski, A., Mucha, J., Pazik, R. & Strek, W. Influence of crystallite size on the thermal conductivity in BaTiO 3 nanoceramics. *Appl. Phys. Lett.* **90**, 1–4 (2007).

94. Davitadze, S. T. *et al.* Specific heat and thermal conductivity of BaTiO3 polycrystalline thin films. *Appl. Phys. Lett.* **80**, 1631–1633 (2002).

95. Donovan, B. F., Foley, B. M., Ihlefeld, J. F., Maria, J. P. & Hopkins, P. E. Spectral phonon scattering effects on the thermal conductivity of nano-grained barium titanate. *Appl. Phys. Lett.* **105**, (2014).

96. Kim, Y., Park, J., Shin, J., An, J. & Cho, J. Thickness-dependent thermal conductivity of ultrathin (< 100 nm) barium titanate films. *Ceram. Int.* **45**, 681–685 (2019).

97. Cho, J., Park, J., Prinz, F. B. & An, J. Thermal conductivity of ultrathin $BaTiO_3$ films grown by plasma-assisted atomic layer deposition. *Scr. Mater.* **154**, 225–229 (2018).

98. Wu, X. *et al.* Glass-Like Through-Plane Thermal Conductivity Induced by Oxygen Vacancies in Nanoscale Epitaxial $La_{0.5}Sr_{0.5}CoO_{3-\delta}$. *Adv. Funct. Mater.* **27**, 1–11 (2017).

99. Buscaglia, M. T. *et al.* Effect of nanostructure on the thermal conductivity of La-doped $SrTiO_3$ ceramics. *J. Eur. Ceram. Soc.* **34**, 307–316 (2014).

100. Wang, Y. *et al.* Interfacial thermal resistance and thermal conductivity in nanograined $SrTiO_3$. *Appl. Phys. Express* **3**, 4–7 (2010).

101. Feng, L., Shiga, T. & Shiomi, J. Phonon transport in perovskite $SrTiO_3$ from first principles. *Appl. Phys. Express* **8**, (2015).

102. Szuromi, P. & Grocholski, B. Natural and engineered perovskites. *Science* **358**, 732–733 (2017).

103. Tilley, R. J. D. *Perovskites: Structure-Property Relationships*. (John Wiley & Sons, 2016).

104. Berry, J. *et al.* Hybrid Organic-Inorganic Perovskites (HOIPs): Opportunities and Challenges. *Adv. Mater.* **27**, 5102–5112 (2015).

105. Li, W. *et al.* Chemically diverse and multifunctional hybrid organic-inorganic perovskites. *Nat. Rev. Mater.* **2**, (2017).

106. Herculano-Houzel, S. Peskovite solar cells. *Science* **342**, 316–317 (2013).

107. Parola, S., Julián-López, B., Carlos, L. D. & Sanchez, C. Optical Properties of Hybrid Organic-Inorganic Materials and their Applications. *Adv. Funct. Mater.* **26**, 6506–6544 (2016).

108. Stranks, S. D. & Snaith, H. J. Metal-halide perovskites for photovoltaic and light-emitting devices. *Nat. Nanotechnol.* **10**, 391–402 (2015).

109. Sourisseau, S. *et al.* Reduced band gap hybrid perovskites resulting from combined hydrogen and halogen bonding at the organic-inorganic interface. *Chem. Mater.* **19**, 600–607 (2007).

110. Haque, M. A., Kee, S., Villalva, D. R., Ong, W. L. & Baran, D. Halide Perovskites: Thermal Transport and Prospects for Thermoelectricity. *Adv. Sci.* **7**, (2020).

111. Ma, Z. Q., Shao, Y., Wong, P. K., Shi, X. & Pan, H. Structural and Electronic Properties of Two-Dimensional Organic-inorganic Halide Perovskites and their Stability against Moisture. *J. Phys. Chem. C* **122**, 5844–5853 (2018).

112. Smith, I. C., Smith, M. D., Jaffe, A., Lin, Y. & Karunadasa, H. I. Between the Sheets: Postsynthetic Transformations in Hybrid Perovskites. *Chem. Mater.* **29**, 1868–1884 (2017).

113. Mao, L., Stoumpos, C. C. & Kanatzidis, M. G. Two-Dimensional Hybrid Halide Perovskites: Principles and Promises. *J. Am. Chem. Soc.* **141**, 1171–1190 (2019).

114. Chen, Y. *et al.* 2D Ruddlesden–Popper Perovskites for Optoelectronics. *Adv. Mater.* **30**, 1–15 (2018).

115. Grancini, G. & Nazeeruddin, M. K. Dimensional tailoring of hybrid perovskites for photovoltaics. *Nat. Rev. Mater.* **4**, 4–22 (2019).

116. Stoumpos, C. C. *et al.* Ruddlesden-Popper Hybrid Lead Iodide Perovskite 2D Homologous Semiconductors. *Chem. Mater.* **28**, 2852–2867 (2016).

117. Kieslich, G., Sun, S. & Cheetham, A. K. Solid-state principles applied to organic–inorganic perovskites: New tricks for an old dog. *Chem. Sci.* **5**, 4712–4715 (2014).

118. Quan, L. N. *et al.* Ligand-Stabilized Reduced-Dimensionality Perovskites. *J. Am. Chem. Soc.* **138**, 2649–2655 (2016).

119. Du, K. Z. *et al.* Two-Dimensional Lead(II) Halide-Based Hybrid Perovskites Templated by Acene Alkylamines: Crystal Structures, Optical Properties, and Piezoelectricity. *Inorg. Chem.* **56**, 9291–9302 (2017).

120. Azadmanjiri, J., Wang, J., Berndt, C. C. & Yu, A. 2D layered organic-inorganic heterostructures for clean energy applications. *J. Mater. Chem. A* **6**, 3824–3849 (2018).

121. Yan, L., Hu, J., Zhou, N., Moran, A. M. & You, W. Enhancing Photovoltaic Performance of Aromatic Ammonium-based Two-Dimensional Organic-Inorganic Hybrid Perovskites via Tuning CH···π Interaction. *Sol. RRL* **4**, 1–9 (2020).

122. Qiu, J. *et al.* 2D Intermediate Suppression for Efficient Ruddlesden-Popper (RP) Phase Lead-Free Perovskite Solar Cells. *ACS Energy Lett.* **4**, 1513–1520 (2019).

123. Zhou, N. *et al.* The Spacer Cations Interplay for Efficient and Stable Layered 2D Perovskite Solar Cells. *Adv. Energy Mater.* **10**, 1–13 (2020).

124. Lian, X. *et al.* The Second Spacer Cation Assisted Growth of a 2D Perovskite Film with Oriented Large Grain for Highly Efficient and Stable Solar Cells. *Angew. Chem. - Int. Ed.* **58**, 9409–9413 (2019).

125. Pietropaolo, A. *et al.* Rationalizing the design and implementation of chiral hybrid perovskites. *Chem* **8**, 1231–1253 (2022).

126. Ma, J., Wang, H. & Li, D. Recent Progress of Chiral Perovskites: Materials, Synthesis, and Properties. *Adv. Mater.* **33**, 1–22 (2021).

127. Hou, Y. *et al.* Two-dimensional hybrid organic-inorganic perovskites as emergent ferroelectric materials. *J. Appl. Phys.* **128**, (2020).

128. Li, W. *et al.* Light-activated interlayer contraction in two-dimensional perovskites for high-efficiency solar cells. *Nat. Nanotechnol.* **17**, 45–52 (2022).

129. Huang, Y. *et al.* Stable Layered 2D Perovskite Solar Cells with an Efficiency of over 19% via Multifunctional Interfacial Engineering. *J. Am. Chem. Soc.* **143**, 3911–3917 (2021).
130. Tu, Q. *et al.* Out-of-Plane Mechanical Properties of 2D Hybrid Organic-Inorganic Perovskites by Nanoindentation. *ACS Appl. Mater. Interfaces* **10**, 22167–22173 (2018).
131. Christodoulides, A. D. *et al.* Signatures of Coherent Phonon Transport in Ultralow Thermal Conductivity Two-Dimensional Ruddlesden-Popper Phase Perovskites. *ACS Nano* **15**, 4165–4172 (2021).
132. Wang, M. & Lin, S. Anisotropic and Ultralow Phonon Thermal Transport in Organic–Inorganic Hybrid Perovskites: Atomistic Insights into Solar Cell Thermal Management and Thermoelectric Energy Conversion Efficiency. *Adv. Funct. Mater.* **26**, 5297–5306 (2016).
133. Jung, Y. *et al.* Thermal Transport Properties of Phonons in Halide Perovskites. *Adv. Mater.* **2204872**, 1–28 (2023).
134. Pisoni, A. *et al.* Ultra-Low Thermal Conductivity in Organic-Inorganic Hybrid Perovskite CH3NH3PbI3. *J. Phys. Chem. Lett.* **5**, 2488–2492 (2014).
135. Giri, A. *et al.* Ultralow Thermal Conductivity of Two-Dimensional Metal Halide Perovskites. *Nano Lett.* **20**, 3331–3337 (2020).
136. Rasel, M. A. J. *et al.* Chain-Length Dependence of Thermal Conductivity in 2D Alkylammonium Lead Iodide Single Crystals. *ACS Appl. Mater. Interfaces* **12**, 53705–53711 (2020).
137. Thakur, S., Dai, Z., Karna, P., Padture, N. P. & Giri, A. Tailoring the thermal conductivity of two-dimensional metal halide perovskites. *Mater. Horiz.* **9**, 3087–3094 (2022).
138. Goodson, K. E. Ordering Up the Minimum Thermal Conductivity of Solids. *Science* **315**, 342–343 (2007).

139. Kim, S. E. & Cahill, D. G. Pushing low thermal conductivity to the limit. *Science* **373**, 963–964 (2021).

140. Ding, J. *et al.* Soft anharmonic phonons and ultralow thermal conductivity in $Mg_3(Sb, Bi)_2$ thermoelectrics. *Sci. Adv.* **7**, eabg1449 (2021).

141. Mukhopadhyay, S. *et al.* Two-channel model for ultralow thermal conductivity of crystalline Tl_3VSe_4. *Science* **360**, 1455–1458 (2018).

142. He, J. *et al.* Ultralow Thermal Conductivity in Full Heusler Semiconductors. *Phys. Rev. Lett.* **117**, 046602 (2016).

143. Christensen, M. *et al.* Avoided crossing of rattler modes in thermoelectric materials. *Nat. Mater.* **7**, 811–815 (2008).

144. Sales, B. C., Mandrus, D. & Williams, R. K. Filled Skutterudite Antimonides: A New Class of Thermoelectric Materials. *Science* **272**, 1325–1328 (1996).

145. Zhao, L.-D. *et al.* Ultralow thermal conductivity and high thermoelectric figure of merit in SnSe crystals. *Nature* **508**, 373–377 (2014).

146. Mukhopadhyay, S., Singh, D. J. & Reinecke, T. L. Ultralow Thermal Conductivity in Cs–Sb–Se Compounds: Lattice Instability versus Lone-Pair Electrons. *Chem. Mater.* **32**, 8906–8913 (2020).

147. Feser, J. P., Chan, E. M., Majumdar, A., Segalman, R. A. & Urban, J. J. Ultralow Thermal Conductivity in Polycrystalline CdSe Thin Films with Controlled Grain Size. *Nano Lett.* **13,** 2122–2127 (2013).

148. Kim, K., He, J., Ganeshan, B. & Liu, J. Disorder enhanced thermal conductivity anisotropy in two-dimensional materials and van der Waals heterostructures. *J. Appl. Phys.* **124**, 055104 (2018).

149. Braun, J. L. *et al.* Breaking network connectivity leads to ultralow thermal conductivities in fully dense amorphous solids. *Appl. Phys. Lett.* **109**, 191905 (2016).

150. Weathers, A. *et al.* Glass-like thermal conductivity in nanostructures of a complex anisotropic crystal. *Phys. Rev. B* **96**, 214202 (2017).

151. Xie, X. *et al.* High and low thermal conductivity of amorphous macromolecules. *Phys. Rev. B* **95**, 035406 (2017).

152. Tambo, N. *et al.* Ultimate suppression of thermal transport in amorphous silicon nitride by phononic nanostructure. *Sci. Adv.* **6**, eabc0075 (2020).

153. Hu, M. & Poulikakos, D. Si/Ge Superlattice Nanowires with Ultralow Thermal Conductivity. *Nano Lett.* **12**, 5487–5494 (2012).

154. Hadland, E. *et al.* Synthesis, Characterization, and Ultralow Thermal Conductivity of a Lattice-Mismatched $SnSe_2(MoSe_2)_{1.32}$ Heterostructure. *Chem. Mater.* **31**, 5699–5705 (2019).

155. Vaziri, S. *et al.* Ultrahigh thermal isolation across heterogeneously layered two-dimensional materials. *Sci. Adv.* **5**, eaax1325 (2019).

156. Chiritescu, C. *et al.* Ultralow Thermal Conductivity in Disordered, Layered WSe_2 Crystals. *Science* **315**, 351–353 (2007).

157. Kim, S. E. *et al.* Extremely anisotropic van der Waals thermal conductors. *Nature* **597**, 660–665 (2021).

158. Zhou, W.-X. & Chen, K.-Q. First-Principles Determination of Ultralow Thermal Conductivity of monolayer WSe2. *Sci. Rep.* **5**, 15070 (2015).

159. Gibson, Q. D. *et al.* Low thermal conductivity in a modular inorganic material with bonding anisotropy and mismatch. *Science* **373**, 1017–1022 (2021).

160. Wei, Z., Chen, Y. & Dames, C. Negative correlation between in-plane bonding strength and cross-plane thermal conductivity in a model layered material. *Appl. Phys. Lett.* **102**, 011901 (2013).

161. Cahill, D. G. Analysis of heat flow in layered structures for time-domain thermoreflectance. *Rev. Sci. Instrum.* **75**, 5119–5122 (2004).

162. Zhu, J. *et al.* Ultrafast thermoreflectance techniques for measuring thermal conductivity and interface thermal conductance of thin films. *J. Appl. Phys.* **108**, 094315 (2010).

163. Liu, J. *et al.* Simultaneous measurement of thermal conductivity and heat capacity of bulk and thin film materials using frequency-dependent transient thermoreflectance method. *Rev. Sci. Instrum.* **84**, 034902 (2013).

164. Schmidt, A. J., Cheaito, R. & Chiesa, M. A frequency-domain thermoreflectance method for the characterization of thermal properties. *Rev. Sci. Instrum.* **80**, 094901 (2009).

165. Wang, H. & Sen, M. Analysis of the 3-omega method for thermal conductivity measurement. *Int. J. Heat Mass Transf.* **52**, 2102–2109 (2009).

166. Zhang, S. *et al.* Recent developments on high Curie temperature PINPMNPT ferroelectric crystals. *J. Cryst. Growth* **318**, 846–850 (2011).

167. Dames, C. Measuring the Thermal Conductivity of Thin Films: 3 Omega and Related Electrothermal Methods. *Annu. Rev. Heat Transf.* **16**, 7–49 (2013).

168. Nataf, G. F. *et al.* Domain-wall engineering and topological defects in ferroelectric and ferroelastic materials. *Nat. Rev. Phys.* **2**, 634–648 (2020).

169. Bednyakov, P. S., Sturman, B. I., Sluka, T., Tagantsev, A. K. & Yudin, P. V. Physics and applications of charged domain walls. *Npj Comput. Mater.* **4**, (2018).

170. Sluka, T., Tagantsev, A. K., Bednyakov, P. & Setter, N. Free-electron gas at charged domain walls in insulating BaTiO3. *Nat. Commun.* **4**, (2013).

171. Xu, G., Wen, J., Stock, C. & Gehring, P. M. Phase instability induced by polar nanoregions in a relaxor ferroelectric system. *Nat. Mater.* **7**, 562–566 (2008).

172. Xu, G., Zhong, Z., Hiraka, H. & Shirane, G. Three-dimensional mapping of diffuse scattering in Pb(Zn 1/3Nb2/3)O3-xPbTiO3. *Phys. Rev. B - Condens. Matter Mater. Phys.* **70**, 1–10 (2004).

173. Li, F. *et al.* The origin of ultrahigh piezoelectricity in relaxor-ferroelectric solid solution crystals. *Nat. Commun.* **7**, 1–9 (2016).

174. Deng, C. *et al.* Reporting Excellent Transverse Piezoelectric and Electro-Optic Effects in Transparent Rhombohedral PMN-PT Single Crystal by Engineered Domains. *Adv. Mater.* **33**, 1–12 (2021).

175. Ye, Z. G. & Dong, M. Morphotropic domain structures and phase transitions in relaxor-based piezo-/ferroelectric (1-x)Pb(Mg1/3Nb2/3)O3-xPbTiO3 single crystals. *J. Appl. Phys.* **87**, 2312–2319 (2000).

176. Luo, C. *et al.* Multi-layered domain morphology in relaxor single crystals with nano-patterned composite electrode. *Acta Mater.* **182**, 10–17 (2020).

177. Vlasin, O. *et al.* Optical Imaging of Nonuniform Ferroelectricity and Strain at the Diffraction Limit. *Sci. Rep.* **5**, 1–11 (2015).

178. Matyjasek, K., Wolska, K., Rogowski, R. Z., Kaczmarek, S. M. & Ivleva, L. I. Polarization reversal kinetics in strontium barium niobate relaxor crystals. *Ferroelectrics* **413**, 311–327 (2011).

179. Zhao, J., Funni, S. D., Molina, E. R., Dickey, E. C. & Jones, J. L. Inhomogeneous electric field-induced structural changes in soft lead zirconate titanate ferroelectric ceramics. *Acta Mater.* **226**, 117682 (2022).

180. Genenko, Y. A., Glaum, J., Hoffmann, M. J. & Albe, K. Mechanisms of aging and fatigue in ferroelectrics. *Mater. Sci. Eng. B Solid-State Mater. Adv. Technol.* **192**, 52–82 (2015).

181. Song, M. S., Lee, K. C., Choi, J. C., Lee, K. & Chae, S. C. Local field inhomogeneity and ferroelectric switching dynamics in Hf1-xZrx O2 thin films. *Phys. Rev. Mater.* **5**, 114408 (2021).

182. Wang, X., Xu, Z., Li, Z. & Chen, H. Study on the inhomogeneity of Pb(In1/2Nb1/2)O 3-Pb(Mg1/3Nb2/3)O3-PbTiO 3 single crystal along the growth direction. *Solid State Commun.* **150**, 1425–1428 (2010).

183. Cahill, D. G., Ford, W. K., Goodson, K. E., Ford, W. K. & Maris, H. J. Nanoscale thermal transport. **793**, (2019).

184. Liu, J. *et al.* Simultaneous measurement of thermal conductivity and heat capacity of bulk and thin film materials using frequency-dependent transient thermoreflectance method. *Rev. Sci. Instrum.* **84**, (2013).

185. Thomsen, C. *et al.* Coherent phonon generation and detection by picosecond light pulses. *Phys. Rev. Lett.* **53**, 989–992 (1984).

186. Chatterjee, K., Negi, A., Kim, K., Liu, J. & Ghosh, T. K. In-Plane Thermoelectric Properties of Flexible and Room-Temperature-Doped Carbon Nanotube Films. *ACS Appl. Energy Mater.* **3**, 6929–6936 (2020).

187. Wang, H. C. *et al.* Enhancement of thermoelectric figure of merit by doping Dy in La 0.1Sr0.9TiO3 ceramic. *Mater. Res. Bull.* **45**, 809–812 (2010).

188. Subramanyan, H., Kim, K., Lu, T., Zhou, J. & Liu, J. On the importance of using exact full phonon dispersions for predicting interfacial thermal conductance of layered materials using diffuse mismatch model. *AIP Adv.* **9**, (2019).

189. Liu, J. *et al.* Thermal conductivity and elastic constants of PEDOT:PSS with high electrical conductivity. *Macromolecules* **48**, 585–591 (2015).

190. Singh, P., Seong, M. & Sinha, S. Detailed consideration of the electron-phonon thermal conductance at metal-dielectric interfaces. *Appl. Phys. Lett.* **102**, 1–5 (2013).

191. Jeong, M. *et al.* Enhancement of Thermal Conductance at Metal-Dielectric Interfaces Using Subnanometer Metal Adhesion Layers. *Phys. Rev. Appl.* **5**, 1–7 (2016).

192. Feng, T., Yang, X. & Ruan, X. Phonon anharmonic frequency shift induced by four-phonon scattering calculated from first principles. *J. Appl. Phys.* **124**, (2018).

193. Xia, Y. Revisiting lattice thermal transport in PbTe: The crucial role of quartic anharmonicity. *Appl. Phys. Lett.* **113**, (2018).

194. Feng, T., Lindsay, L. & Ruan, X. Four-phonon scattering significantly reduces intrinsic thermal conductivity of solids. *Phys. Rev. B* **96**, 1–6 (2017).

195. Tyunina, M. *et al.* Epitaxial growth of perovskite oxide films facilitated by oxygen vacancies. *J. Mater. Chem. C* **9**, 1693–1700 (2021).

196. Schlom, D. G. *et al.* Elastic strain engineering of ferroic oxides. *MRS Bull.* **39**, 118–130 (2014).

197. Li, H. *et al.* Two-dimensional growth of high-quality strontium titanate thin films on Si. *J. Appl. Phys.* **93**, 4521–4525 (2003).

198. Zheng, J. *et al.* Anharmonicity-induced phonon hardening and phonon transport enhancement in crystalline perovskite BaZrO3. *Phys. Rev. B* **105**, 1–14 (2022).

199. Zhao, Y. *et al.* Lattice thermal conductivity including phonon frequency shifts and scattering rates induced by quartic anharmonicity in cubic oxide and fluoride perovskites. *Phys. Rev. B* **104**, 1–20 (2021).

200. Wang, W., Wang, X., Zhao, Y., Meng, S. & Dai, Z. The ultra-low lattice thermal conductivity dominated by the quartic anharmonicity in Bi-based binary compounds A3Bi (A = K, Rb). *Epl* **138**, (2022).

201. Osei-Agyemang, E., Adu, C. E. & Balasubramanian, G. Ultralow lattice thermal conductivity of chalcogenide perovskite CaZrSe3 contributes to high thermoelectric figure of merit. *Npj Comput. Mater.* **5**, (2019).

202. Xiao, Y. *et al.* Low lattice thermal conductivity of hydride-based cubic antiperovskites A3HB (a = Li, Na; B = S, se, Te) with higher-order anharmonicity correction. *Int. J. Energy Res.* **46**, 13687–13697 (2022).

203. Xia, Y., Pal, K., He, J., Ozoliņš, V. & Wolverton, C. Particlelike Phonon Propagation Dominates Ultralow Lattice Thermal Conductivity in Crystalline Tl3VSe4. *Phys. Rev. Lett.* **124**, 1–7 (2020).

204. Yue, T. *et al.* Theoretical prediction of mechanics, transport, and thermoelectric properties of full Heusler compounds Na2KSb and X2CsSb (X= K,Rb). *Phys. Rev. B* **105**, 1–13 (2022).

205. Dongre, B., Carrete, J., Mingo, N. & Madsen, G. K. H. Ab initio lattice thermal conductivity of bulk and thin-film α-Al2O3. *MRS Commun.* **8**, 1119–1123 (2018).

206. Liang, L. H. & Li, B. Size-dependent thermal conductivity of nanoscale semiconducting systems. *Phys. Rev. B - Condens. Matter Mater. Phys.* **73**, 1–4 (2006).

207. Knoop, F., Purcell, T. A. R., Scheffler, M. & Carbogno, C. Anharmonicity in Thermal Insulators -- An Analysis from First Principles. 1–5 (2022).

208. Negi, Ankit, Hwang Pill Kim, Zilong Hua, Anastasia Timofeeva, Xuanyi Zhang, Yong Zhu, Kara Peters, Divine Kumah, Xiaoning Jiang, and Jun Liu. Ferroelectric domain wall engineering enabled thermal modulation in PMN-PT single crystals. *Advanced Materials* (2023): 2211286.

209. Negi, Ankit, Alejandro Rodriguez, Xuanyi Zhang, Andrew H. Comstock, Cong Yang, Dali Sun, Xiaoning Jiang, Divine Kumah, Ming Hu, and Jun Liu. Thickness-Dependent Thermal Conductivity and Phonon Mean Free Path Distribution in Single-Crystalline Barium Titanate. *Advanced Science* (2023): 2301273.